Topics in Collider Physics

Wenhan Zhu

A Dissertation
Presented to the Faculty
of Princeton University
in Candidacy for the Degree
of Doctor of Philosophy

Recommended for Acceptance
by the Department of
Physics
Adviser: Valerie Halyo

April 2012

Abstract

The Large Hadron Collider (LHC), the world's largest and highest-energy particle accelerator, is leading particle physics into a new era. This experiment will very likely to discover the mechanism responsible for electroweak symmetry breaking and also possibly new particles at the TeV scale.

This thesis addresses some topics which we may hope to probe at the LHC. Chapter 1 serves an an introduction, reviewing the Standard Model and introducing all the topics covered in this thesis. In Chapter 2, we discusses the evaluation of PDF uncertainty of $W \to \ell\nu$ cross section at the LHC with the Hessian Method. In Chapter 3, we discusses the search channel for boosted Higgs boson produced with a vector boson using Jet Trimming Technique. In Chapter 4, we discusses a new collider based probe of electroweak symmetry breaking, designed to look for models that approximate the Standard Model at the electroweak scale, but which deviate from it at higher energies. In Chapter 5, we discusses the feasibility of seeing a Higgs boson which decays to four bottom quarks through a pair of long-lived (pseudo-)scalars. In Chapter 6, we investigates various sources of the systematic uncertainty in the dijet mass distribution of W+jets at Tevatron . Chapter 7 contains the conclusions.

Acknowledgements

First, I would like to thank my advisers, Valerie Halyo and Lian-Tao Wang, for introducing me to the methods and ideas of particle physics phenomenology.

Much of what I learned in graduate school was taught to be by my collaborators: Nadia Adam, Tao Han, Pratima Jindal, David Krohn, Gavin Salam, Matt Strassler and Scott Yost. I've benefited greatly from our work together. David in particular was very helpful: by sharing his office with me and patiently answering my many questions, he helped me to get my research going.

Over the years I've been lucky to interact with many talented physicists. I am grateful for the conversations I've had with Johan Awall , Steve Gubser, Igor Klebanov, Adam Martin, James Olsen, Matt Reece, Chris Tully, Herman Verlinde, and Jan Winter. Surely there are others who should be on this list - I apologize to those I forgot to name.

I would also want to thank all the students that I have taught at Princeton. They always remind me the fun of physics and inspire me with their curiosity and eager to learn physics.

Finally, I'd like to thank my parents and my wife Yuan Yuan for their support and encouragement.

Relation to Previously Published Work

Chapter 2 comes from ref. [1], chapter 3 comes from ref. [2], chapter 4 comes from ref. [3], and chapter 5 is derived from work in progress with Valerie Halyo, Gavin Salam and Matt Strassler.

Contents

Chapter 1

Introduction

The Standard Model (SM) of particle physics is a theory describing the electromagnetic, weak, and strong nuclear interactions, which mediate the dynamics of the known subatomic particles. The SM was first proposed and analysed over 40 years ago [4, 5, 6, 7, 8, 9]. Because of its success in explaining a wide variety of experimental results, the SM is sometimes regarded as a theory of almost everything. However, we still have yet found the Higgs boson, which is necessary to keep the SM self-consistent. Moreover, the SM possesses certain theoretical traits which modern field theory tells are less than desirable (e.g. fine tuning).

Fortunately, LHC has already begun to take data, which allows us to probe the SM at unprecedented energies, and look with incredible precision for the signatures of new particles. Over the next decade we can expect to discover the SM Higgs boson (or probe whatever else does its job). This thesis presents several results in particle physics phenomenology relevant to this exciting era.

1.1 The Standard Model

1.1.1 Particles

The fundamental particles described by the SM can be split into two subsets. Particles which carry a half integer spin are classified as fermions and can be further subdivided into quarks and leptons. The other subset consists of particles with integer spin and these are classified as bosons. These bosons serve as the mediator particles of the electromagnetic, weak, and strong forces. The bosons could also have charges and thus may interact with each other.

The fundamental fermions and bosons described by SM are shown in Table 1.1. There are 12 fermions, which consists of six quarks (up, down, charm, strange, top and down), three leptons (electron, muon and tau), and three neutrinos (electron neutrino, muon neutrino and tau neutrino). The fundamental bosons are: gluon (g) carries the strong force, the photon (γ) the electromagnetic force, and the W^+, W^+ and Z the weak force. One final boson, the Higgs boson, has been postulated but not observed experimentally.

1.1.2 Quantum Chromodynamics

Quantum Chromodynamics (QCD) is a theory of the strong interaction (color force), a fundamental force describing the interactions of the quarks and gluons making up hadrons (such as the proton, neutron or pion). In the SM, QCD is a gauge theory of a $SU(3)_c$ gauge group, and the Lagrangian is:

$$\mathcal{L}_{\text{QCD}} = \bar{\psi}_i(i\gamma^\mu\partial_\mu - m)\psi_i - gG^a_\mu\bar{\psi}_i\gamma^\mu T^a_{ij}\psi_j - \frac{1}{4}G^a_{\mu\nu}G^{\mu\nu}_a \tag{1.1}$$

where $\bar{\psi}_i$ is the quark field, in the fundamental representation of the SU(3) gauge group, and G^a_μ is the gluon field, in the adjoint representation of the SU(3) gauge

Quarks (spin=$\frac{1}{2}$)		
Particle	Mass (GeV)	Electric Charge (q)
d	0.0041-0.0058	-$\frac{1}{3}$
u	0.0017-0.0033	$\frac{2}{3}$
s	0.08-0.13	-$\frac{1}{3}$
c	1.18-1.34	$\frac{2}{3}$
b	4.13-4.37	-$\frac{1}{3}$
t	170.4-173.6	$\frac{2}{3}$
Leptons (spin=$\frac{1}{2}$)		
Particle	Mass (GeV)	Electric Charge (q)
e	0.000511	-1
ν_e	$<5 \times 10^{-7}$	0
μ	0.106	-1
ν_μ	1.9×10^{-4}	0
τ	1.777	-1
ν_τ	0.0182	0
Bosons (spin=0,1)		
Particle	Mass (GeV)	Electric Charge (q)
g	0	0
γ	0	0
W^+	80.376	1
Z	91.166	0
H	>114	0

Table 1.1: Table of SM particles. Antiparticles are charge conjugates of a particle with the same mass. The Higgs bosons are not yet experimentally discovered.

group. T^a_{ij} are the generators of the SU(3) gauge group. The Gell-Mann matrices provide one such representation for the generators. $G^a_{\mu\nu}$ is the gauge invariant gluonic field strength tensor, given by

$$G^a_{\mu\nu} = \partial_\mu G^a_\nu - \partial_\nu G^a_\mu - g f^{abc} G^b_\mu G^c_\nu \tag{1.2}$$

where f^{abc} are the structure constants of SU(3).

The QCD has two special features:

- Confinement: the force between quarks does not diminish as they are separated. This means it takes infinite amount of energy to take apart two quarks, and

they are forever bounded into hadrons.

- Asymptotic Freedom:the interactions between quarks become weaker at higher energy scales or shorter distance.

Because of the Asymptotic Freedom, the computation of QCD described by perturbation theory is accurate in experiments performed at very high energies. However, when it comes to low energy scale QCD, the theory becomes strongly interacting, and there is no First Principle computation available. For instance, the Parton Distribution Functions (PDF) are extracted from a global analysis of the experiments worldwide.

1.1.3 Electroweak Interactions

In particle physics, the electroweak interaction is the description of two of the four known fundamental interactions of nature: electromagnetism and the weak interaction. Although these two forces appear very different at low energies, the theory models them as two different aspects of the same force. Above the unification energy, on the order of 100 GeV, they would merge into a single electroweak force.

The SM electroweak interaction is an $SU(2)_L \times U(1)_Y$ gauge theory containing three $SU(2)_L$ gauge bosons, W^i_μ, $i = 1, 2, 3$, and one $U(1)_Y$ gauge boson, B_μ. The Lagrangian for the electroweak interactions is divided into four parts:

$$\mathcal{L}_{\text{EW}} = \mathcal{L}_{\text{gauge}} + \mathcal{L}_{\text{fermion}} + \mathcal{L}_{\text{higgs}} + \mathcal{L}_{\text{yukawa}} \tag{1.3}$$

The gauge interactions describe the interaction between the W fields and B field:

$$\mathcal{L}_{\text{gauge}} = -\frac{1}{4} W^i_{\mu\nu} W^{\mu\nu i} - \frac{1}{4} B_{\mu\nu} B^{\mu\nu} \tag{1.4}$$

$$W^i_{\mu\nu} = \partial_\nu W^i_\mu - \partial_\mu W^i_\nu + g\epsilon^{ijk} W^j_\mu W^k_\nu \quad , \tag{1.5}$$

$$B_{\mu\nu} = \partial_\nu B_\mu - \partial_\mu B_\nu \quad . \tag{1.6}$$

The fermion interactions describe the interaction between the fermion and gauge fields:

$$\mathcal{L}_f = \bar{Q}_i \gamma^\mu i D_\mu Q_i + \bar{u}_i \gamma^\mu i D_\mu u_i + \bar{d}_i \gamma^\mu i D_\mu d_i + \bar{L}_i \gamma^\mu i D_\mu L_i + \bar{e}_i \gamma^\mu i D_\mu e_i \tag{1.7}$$

where the Q and L are SU(2) fermion doublet, and u,d and e are SU(2) singlet, and

$$D_\mu = \partial_\mu - i\frac{g}{2}\tau \cdot W_\mu - i\frac{g'}{2} B_\mu Y. \tag{1.8}$$

The interactions describe the interaction between the Higgs field itself and between the Higgs field and the gauge fields:

$$\mathcal{L}_{higgs} = |D_\mu \Phi|^2 - V(\Phi) \tag{1.9}$$

ϕ is a complex scalar SU(2) doublet:

$$\Phi = \begin{pmatrix} \phi^+ \\ \phi^0 \end{pmatrix} \tag{1.10}$$

with a scalar potential given by

$$V(\Phi) = \mu^2 \mid \Phi^\dagger \Phi \mid + \lambda \Big(\mid \Phi^\dagger \Phi \mid \Big)^2 \tag{1.11}$$

the state of minimum energy for $\mu^2 < 0$ is not at $\Phi = 0$ and the scalar field develops a VEV. The direction of the minimum in $SU(2)_L$ space is not determined since the

potential depends only on the combination $\Phi^\dagger\Phi$ and we arbitrarily choose

$$\langle\Phi\rangle = \frac{1}{\sqrt{2}}\begin{pmatrix} 0 \\ v \end{pmatrix} \tag{1.12}$$

With this choice the scalar doublet has $U(1)_Y$ charge (hypercharge) $Y_\Phi = 1$ and the electromagnetic charge is

$$Q = \frac{(\tau_3 + Y)}{2} \ . \tag{1.13}$$

Therefore,

$$Q\langle\Phi\rangle = 0 \tag{1.14}$$

nd electromagnetism is unbroken by the scalar VEV. The VEV hence yields the desired symmetry breaking scheme,

$$SU(2)_L \times U(1)_Y \to U(1)_{EM}. \tag{1.15}$$

Now, we will show how W and Z gauge bosons become massive from Higgs Mechanism:

$$\mathcal{L}_s = (D^\mu\Phi)^\dagger(D_\mu\Phi) - V(\Phi), \tag{1.16}$$

$$\Phi = \frac{1}{\sqrt{2}}\begin{pmatrix} 0 \\ v+h \end{pmatrix} \tag{1.17}$$

which gives the contribution to the gauge boson masses from the scalar kinetic energy term ,

$$\frac{1}{2}(0,v)\left(\frac{1}{2}g\tau\cdot W_\mu + \frac{1}{2}g'B_\mu\right)^2\begin{pmatrix} 0 \\ v \end{pmatrix} \tag{1.18}$$

The physical gauge fields are then two charged fields, $W^\pm$, and two neutral gauge

bosons, Z and γ.

$$W_\mu^\pm = \frac{1}{\sqrt{2}}(W_\mu^1 \mp iW_\mu^2) \tag{1.19}$$

$$Z^\mu = \frac{-g'B_\mu + gW_\mu^3}{\sqrt{g^2 + g'^{\,2}}} \tag{1.20}$$

$$A^\mu = \frac{gB_\mu + g'W_\mu^3}{\sqrt{g^2 + g'^{\,2}}}. \tag{1.21}$$

The gauge bosons obtain masses from the Higgs mechanism:

$$M_W^2 = \frac{1}{4}g^2v^2 \tag{1.22}$$

$$M_Z^2 = \frac{1}{4}(g^2 + g'^{\,2})v^2 \tag{1.23}$$

$$M_A = 0. \tag{1.24}$$

Since the massless photon must couple with electromagnetic strength, e, the coupling constants define the weak mixing angle θ_W,

$$e = g\sin\theta_W \tag{1.25}$$

$$e = g'\cos\theta_W \tag{1.26}$$

Finally, the Yukawa interaction is the interaction between the fermions and the Higgs Fields and it is responsible for the mass generation of the fermions:

$$\mathcal{L}_{\text{yukawa}} = -\lambda_d\bar{Q}_i\Phi d_i - \lambda_u\bar{Q}_i\Phi^c u_i - \lambda_e\bar{L}_i\Phi e_i + h.c. \tag{1.27}$$

This gives the effective coupling

$$-\lambda_d\frac{1}{\sqrt{2}}(\overline{u}_L,\ \overline{d}_L)\begin{pmatrix} 0 \\ v+h \end{pmatrix}d_R + h.c. \tag{1.28}$$

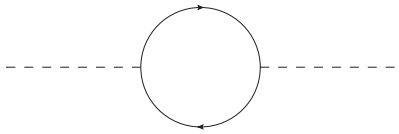

Figure 1.1: A loop correction to the SM Higgs boson mass.

which can be seen to yield a mass term for the down quark if we make the identification

$$\lambda_d = \frac{m_d\sqrt{2}}{v}. \tag{1.29}$$

And hence we could generate mass for up quark and charged leptons. Since the neutrino has no right handed partner, it remains massless.

1.2 Physics Beyond the SM

Although the SM is very successful in describing physics at energies separated by many orders of magnitude, it is not perfect. The main problem is that the SM Higgs boson is supposed to be a fundamental scalar, whose mass is not protected by any symmetry from its loop interaction cut-off by the Plank scale shown in Fig 1.1. The Higgs boson is so much lighter than the Planck mass (or the grand unification energy, or a heavy neutrino mass scale): one would expect that the large quantum contributions to the square of the Higgs boson mass would inevitably make the mass huge, comparable to the scale at which new physics appears, unless there is an incredible fine-tuning cancellation between the quadratic radiative corrections and the bare mass. Therefore, if the SM is really correct, then the parameters of the theory must be tuned against each other with an incredible, seemingly unnatural, precision. This concern is known as the hierarchy problem.

Many solutions of hierarchy problem has been proposed, with different degrees

of success. Supersymmetry [11] supposes there is a symmetry between fermions and bosons, so the chiral symmetry which protects the mass of fermions in turn protects the mass of the Higgs boson. Other theories suggest the Higgs boson mass is stable at the electroweak scale because it is the pseudo-Goldstone boson of an approximate symmetry [12, 13, 14]. Some theories even remove the Higgs boson altogether, breaking SU(2) $\times$ U(1) with the condensate of strongly interacting fields, in analogy to the chiral symmetry breaking of QCD [15, 16]. This is not a comprehensive list ,and already most of the theories here have run into tension with experimental data[1]. The point one should take away is simply that most considerations of naturalness hint that the SM picture of electroweak symmetry breaking is not the full story, and most attempts to construct a more appealing theory require new physics states near the TeV scale.

1.3 Overview of Research Presented in this Thesis

The research presented in this thesis touches upon many of the topics presented in the preceding pages. To reiterate, the main concern of particle physics at the TeV scale is to understand the nature of electroweak symmetry breaking (i.e. finding the Higgs boson or whatever else does its job).

The research presented here begins, in chapter 2, with a study of the PDF Uncertainties in the $W \to \ell\nu$ Cross Sections at the LHC. The W production cross section measurement at the LHC is not only a test of the SM, but also serves as a important tool to measure the luminosity through a comparison of the measured rates to the best theoretical calculations of the cross-section. Therefore, it is important to estimate the systematic error of the cross section calculation of this channel. Due to the limitations in present lattice QCD calculations, the known parton distribution functions

[1]The tension between new models of electroweak symmetry breaking, which usually require states near the TeV-scale, and precision data, which excludes most new states below ~ 10 TeV, is known as the little hierarchy problem [17, 18].

are instead obtained by using experimental data. We use Hessian Error Method to estimate the systematic uncertainty of W production cross section propagated from the uncertainties on the PDF parameters.

In Chapter 3, we propose a new search strategy for the SM Higgs boson. The motivation for this strategy is the observation that the data from both the LEP and Tevatron experiment prefer a light Higgs boson around 120 GeV. With this mass, the Higgs boson will mostly decay to b quarks and previous study shows this channel is very challenging. However, if we require that the Higgs boson is produced with a vector boson and they are both boosted, we could reduce the QCD background significantly. In addition, after we will apply jet trimming, a modern jet technique, to the Higgs jet, we could get a very good resolution of the Higgs boson mass. Combining everything together, we are able to achieve a statistical significance of 4.5 σ for a 115 GeV Higgs boson with $30 fb^{-1}$ at the LHC.

In Chapter 4, we discusses another collider measurement related to electroweak symmetry breaking. The motivation for the research presented in this chapter is the observation that all the constraints from precision data hint that we will discover a particle which looks very much like the SM Higgs boson. Now, the particle we find at the LHC/Tevatron may not be the SM Higgs boson. It could, for instance, be a composite state from dynamics above the TeV scale. However, should we discover such a particle and measure its quantum numbers and couplings, they would probably be very close to those of the SM Higgs boson, and given the messy environment of the LHC it would be difficult for physicists to claim they have seen unambiguous signs of phenomena beyond the SM based on, say, a 20% discrepancy in a particular Higgs decay channel. This is a problem, because without any additional handle we would have to wait for experiments to directly produce new physics states, and these could be out of the reach of our most powerful colliders. Chapter 4 proposes a new measurement designed to detect new phenomena from beyond the SM physics which

could subtly alter the couplings of the Higgs boson to gauge bosons. In particular, we propose measuring the shape of the angular distribution calculated from the decay products of gauge bosons produced in vector boson fusion. Because it measures a shape, rather than a rate, this measurement is not susceptible to the large experimental uncertainties which normally accompany the measurement of Higgs couplings. Unless we see more obvious signs of new physics, this sort of measurement might our best shot at understanding electroweak symmetry breaking using collider data.

In Chapter 5, we introduces another search strategy for the Higgs boson, with four bottom quarks final states through a pair of long-lived (pseudo-)scalars. In this chapter, we will focus on the fact that all the tracks from the signal are produced at highly displaced vertices, therefore, they will have quite substantial impact parameters. After applying several powerful cuts, we are able to reduce the major background substantially, and we are likely to discover this channel with $1 fb^{-1}$ luminosity at LHC with 7 TeV center-of-mass.

In Chapter 6, we discusses the systematic uncertainty for dijet invariant mass distribution associated with the W boson at the CDF. In this chapter, we will investigate the sensitivity of the dijet mass distribution to various parameters, for example, Parton Distribution choice, renormalization and factorization scale choice, jet matching scale choice, and different Monte Carlo Generator choice. We find out that the biggest uncertainty is from the difference between the MLM matching and CKKW matching scheme.

Chapter 2

Evaluation of the PDF Uncertainties in the $W \to \ell\nu$ Cross Sections at the LHC

We study the PDF systematic errors in the measurement of the $W \to \ell\nu$ cross-sections at the LHC. We consider the systematic errors in both the total cross-section and acceptance for anticipated experimental cuts. The method employed here is the Hessian method. In this method, the χ^2 function, which is used to extract the "best fit" between the theory and the experiment, is used to explore the neighbourhood of the global minimum in order to quantify the uncertainties. This chapter derives from ref.[1]

2.1 Motivation

A precise measurement of gauge boson production cross-sections for pp scattering will be crucial at the LHC. W and Z bosons will be produced copiously, and a careful measurement of their production cross-sections will be important in testing the SM more rigorously than ever before, and uncovering signs of new physics which may

appear through radiative corrections. In addition, these cross-sections have been proposed as a "standard candle" for measuring the luminosity through a comparison of the measured rates to the best theoretical calculations of the cross-section. Investigation of this means of measuring luminosity began at the Tevatron and will continue at the LHC [19, 20].

The dominant production mechanism for Z or W bosons is the Drell-Yan process [21], in which a quark and anti-quark annihilate to form a vector boson, which subsequently decays into a lepton pair. The W production process is actually observed through the charged lepton and missing energy of the neutrino produced in its decay. In general, the cross-section may be inferred from the number $N_W^{\rm obs}$ of observed events via the relation

$$N_W^{\rm obs} = \sigma^{\rm tot}\,{\rm B}R(W \to \ell\nu) A_W \int \mathcal{L} dt. \tag{2.1}$$

A_W is the acceptance obtained after applying the experimental selection criteria. For example, if the cuts require $p_{\rm T} > p_{\rm T}^{min}$, $0 < \eta^\ell < \eta_{max}$, and $\not\!\!E_{\rm T} > \not\!\!E_{\rm T}^{min}$, then

$$\begin{aligned} A_W(p_{\rm T}^{min}, \eta_{max}) &= \frac{1}{\sigma^{\rm tot}\,{\rm B}R(W \to \ell\nu)} \int_{p_{\rm T}^{min}}^{\sqrt{s}/2} dp_{\rm T}{}^{\ell} \int_{\not\!\!E_{\rm T}^{min}}^{\sqrt{s}/2} dp_{\rm T}{}^{\nu} \\ &\times \int_{-\eta_{max}}^{\eta_{max}} d\eta_\ell \int_{-\infty}^{\infty} d\eta_\nu \frac{d^4\sigma}{dp_{\rm T}{}^{\ell}\, dp_{\rm T}{}^{\nu} d\eta_\ell d\eta_\nu}\, {\rm B}R(W \to \ell\nu) \end{aligned} \tag{2.2}$$

Alternatively to the W production cross-section measurement, the corrected W yield can be used as a standard candle for a luminosity monitor in LHC if one calculates the cross-section and solves for $\int \mathcal{L} dt$. The theoretical cross-section may be constructed by convoluting a parton-level cross-section $\widehat{\sigma}_{ab}$ for partons a and b with the parton density functions (PDFs) f_a, f_b for these partons,

$$\sigma^{\rm th} BR(W \to \ell\nu) = \sum_{a,b} \int_0^1 dx_1 dx_2 f_a(x_1) f_b(x_2)\, \widehat{\sigma}_{ab}(x_1, x_2) \tag{2.3}$$

integrating over the momentum fractions x_1, x_2, and applying cuts relevant to the experiment.

There are various sources of theoretical uncertainties in this computation, and here we will focus on the errors from the PDFs with the Hessian Method described in [22].

2.2 PDFs parametrization and The Hessian Methods

The parton distribution function (PDF) is defined as the probability density for finding a particle with a certain longitudinal momentum fraction x at momentum transfer Q^2. Because of the inherent non-perturbative effect in a QCD binding state, PDFs cannot be obtained by perturbative QCD. Due to the limitations in present lattice QCD calculations, the known PDFs are instead obtained through the global analysis of experimental data from a wide range of hard-scattering processes, using perturbative QCD to calculate the hard scattering and to determine the dependence of the PDFs on Q by the renormalization-group based evolution equations.

The PDFs are specified in a parametrized form at a fixed low energy scale Q_0, which we choose to be 1 GeV. The PDFs at all higher Q are determined from these by the NLO perturbative QCD evolution equations. The functional forms we use are

$$f(x, Q_0) = A_0\, x^{A_1}\, (1-x)^{A_2}\, (1 + A_3\, x^{A_4}) \tag{2.4}$$

with independent parameters for parton flavour combinations $u_v \equiv u - \bar{u}$, $d_v \equiv d - \bar{d}$, g, and $\bar{u} + \bar{d}$. We assume $s = \bar{s} = 0.2\,(\bar{u} + \bar{d})$ at Q_0. Therefore, there are a total of d=16 independent parameters, referred to generically as $\{a_i\}$.

To extract the PDFs, we will define the χ^2, which measures the quality of the fit

between theory and experiment:

$$\chi^2 = \sum_I \left(\frac{D_{nI} - T_{nI}}{\sigma_{nI}} \right)^2 \tag{2.5}$$

where T_{nI}, D_{nI}, and σ_{nI} are the theory value, data value, and uncertainty for data point I of data set (or "experiment") n. We find the parameter set that minimizes it to obtain a "best estimate" of the true PDFs, denoted by S_0.

To study the uncertainties, we must explore the variation of χ^2 in the neighbourhood of its minimum, rather than focusing only on S_0 as has been done in the past. Moving the parameters away from the minimum increases χ^2 by an amount $\Delta\chi^2$. It is natural to define the relevant neighbourhood of the global minimum as

$$\Delta\chi^2 \leq T^2 \tag{2.6}$$

where T is a *tolerance parameter*. The Hessian formalism developed provides a reliable and efficient method of calculating the variation of all predictions of PDFs in this neighbourhood, as long as T is within the range where a quadratic expansion of χ^2 in terms of the PDF parameters is adequate.

The standard error matrix approach begins with a Taylor series expansion of $\chi^2(S)$ around its minimum S_0, keeping only the leading terms. This produces a quadratic form in the displacements from the minimum:

$$\Delta\chi^2 = \chi^2 - \chi_0^2 = \sum_{i=1}^{d} \sum_{j=1}^{d} H_{ij} \left(a_i - a_i^0\right) \left(a_j - a_j^0\right) \tag{2.7}$$

where $\chi_0^2 = \chi^2(S_0)$ is the value at the minimum, $\{a_j^0\} = \{a_j(S_0)\}$ is its location, and $\{a_j\} = \{a_j(S)\}$. H_{ij} is the Hessian matrix ,the matrix of second derivatives of χ^2 at the minimum.

The Hessian matrix H_{ij} has a complete set of orthonormal eigenvectors v_{ik} defined

by

$$\sum_{j=1}^{d} H_{ij}\, v_{jk} \;=\; \epsilon_k\, v_{ik} \tag{2.8}$$

$$\sum_{i=1}^{d} v_{i\ell}\, v_{ik} \;=\; \delta_{\ell k}\ , \tag{2.9}$$

where $\{\epsilon_k\}$ are the eigenvalues and $\delta_{\ell k}$ is the unit matrix. Displacements from the minimum are conveniently expressed in terms of the eigenvectors by

$$a_i - a_i^0 = \sum_{k=1}^{d} v_{ik}\, s_k\, z_k\ , \tag{2.10}$$

where scale factors s_k are introduced to normalize the new parameters z_k such that

$$\Delta\chi^2 \;=\; \sum_{k=1}^{d} z_k^2\ . \tag{2.11}$$

ith this normalization, the relevant neighborhood (2.6) of the global minimum corresponds to the interior of a hypersphere of radius T:

$$\sum_{k=1}^{d} z_k^2 \;\le\; T^2\ . \tag{2.12}$$

Now we will construct the *Eigenvector Basis* PDFs $\{S_\ell^\pm, \ell = 1, \ldots, d\}$ as:

$$z_k(S_\ell^\pm) = \pm\, t\, \delta_{k\ell}\ . \tag{2.13}$$

More explicitly, S_1^+ is defined by $(z_1, \ldots, z_d) = (t, 0, \ldots, 0)$, *etc.* We make displacements in both directions along each eigenvector to improve accuracy; which direction is called "up" is totally arbitrary. As a practical matter, we choose $t = 5$ for the displacement distance.

Let $X(S)$ be any variable that depends on the PDFs. It can be a physical quantity

such as the W production cross section. The best-fit estimate for X is $X^0 = X(S_0)$. To find the uncertainty, it is only necessary to evaluate X for each of the $2d$ sets $\{S_\ell^\pm\}$.

$$D_k(X) = X(S_k^+) - X(S_k^-) \tag{2.14}$$

$$D(X) = \left(\sum_{k=1}^{d} [D_k(X)]^2 \right)^{1/2} \tag{2.15}$$

$$\tag{2.16}$$

Finally, as defined in[22], the master equation we will use to evaluate the uncertainty is:

$$\boxed{\Delta X = \frac{T}{2t} D(X)} \,. \tag{2.17}$$

2.3 Results

Figure 2.1 and Figure 2.2 show the results of the inclusive W to di-lepton production cross-section using various CTEQ [25] and MRST [23] PDFs. The upward shift of about 7% (between CTEQ6.1 and 6.5 and MRST2004 and 2006) results from the inclusion of heavy quark effects in the latest PDF calculations. The acceptance due to the cuts in Table 2.1 using each of these PDFs is shown in Fig 2.3 and Fig 2.4.[1]

	Transverse Momentum (GeV/c)	Pseudorapidity	Missing Transverse Energy (GeV)
Cut 1	$p_{\mathrm{T}} > 25$	$\lvert\eta\rvert < 1$	$\not\!\!E_{\mathrm{T}} > 20$
Cut 2	$p_{\mathrm{T}} > 25$	$1 < \lvert\eta\rvert < 2.2$	$\not\!\!E_{\mathrm{T}} > 20$
Cut 3	$p_{\mathrm{T}} < 25$	$\lvert\eta\rvert < 1$	$\not\!\!E_{\mathrm{T}} > 30$

Table 2.1: Acceptance regions for the PDF uncertainty study

[1] Theoretical issues which may affect the contribution of the PDFs to the NNLO K-factor are not included here as we are concerned primarily with the error at NLO. See Refs. [24] for details.

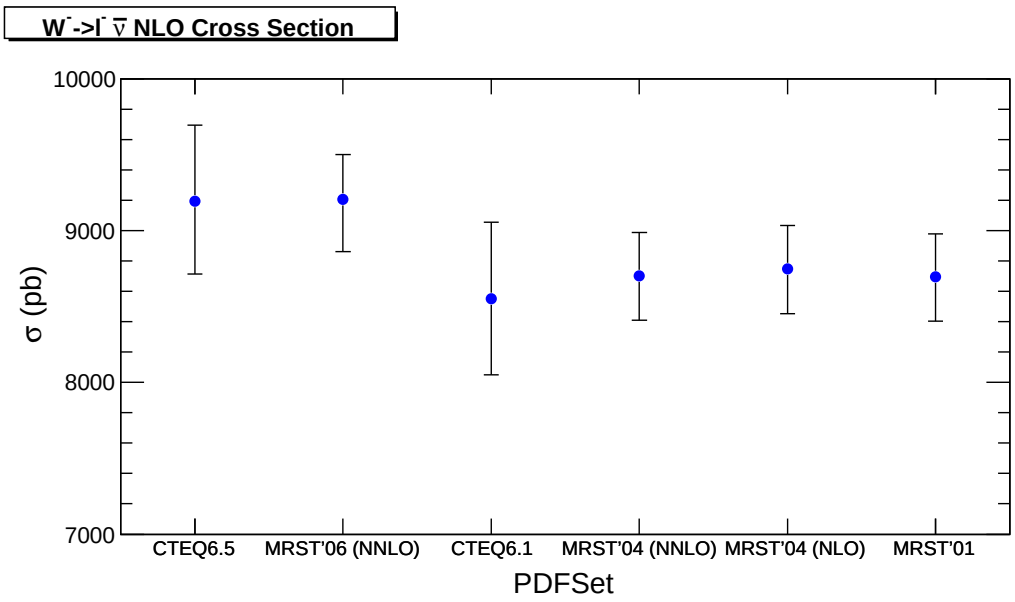

Figure 2.1: Comparison of $W^- \to l^- \overline{\nu}$ total cross-sections for several recent PDF calculations.

The difference in the uncertainties (approximately a factor of two) between the results obtained from the CTEQ and MRST PDF error sets is due to different assumptions made by the groups while creating the eigenvector PDF sets.

Finally we study the sensitivity of the kinematic acceptance calculations to the uncertainties affecting the PDF sets. Fig 2.5 and Fig 2.7 for W^- and Fig 2.6 and Fig 2.8 for W^+ show the systematic error on the production cross-sections as a function of the $|\eta|$ cut and minimum lepton p_{T} for variations on the three types of cuts in Table 2.1. The fractional uncertainties, shown in in the same figures, demonstrate that the relative uncertainty in the cross-section is very flat as a function of the kinematic cuts, until the region of extreme cuts and low statistics in the MC are reached. The corresponding uncertainty on the acceptance as a function of the kinematic cuts is shown in Fig 2.9 and Fig 2.11 for W^- and Fig 2.10 and Fig 2.12 for W^+. These show a similar dependence to the cross-section uncertainties, though the fractional errors are smaller.

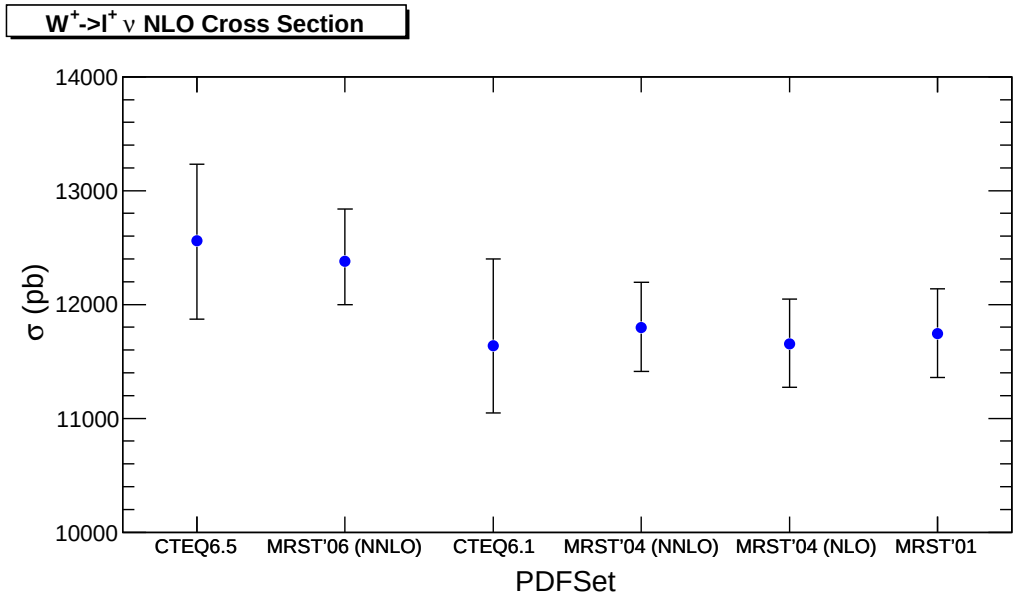

Figure 2.2: Comparison of $W^+ \to l^+\nu$ total cross-sections for several recent PDF calculations.

2.4 Conclusions

The PDF uncertainty is evaluated for $W \to \ell\nu$ at the LHC, shown in Table 2.3. The errors are asymmetric, so we take the largest of the two (up or down) uncertainties as the total fractional error for the PDF calculation. We choose the first cut set, since it is the most representative of likely analysis cuts at the LHC experiments.CTEQ errors, rather than the MRST errors, are used because they give a more conservative estimate. The results are shown in Table 2.2.

PDF Uncertainty (%)

W^-		W^+	
Cross-Section $\Delta\sigma$	Acceptance ΔA	Cross-Section $\Delta\sigma$	Acceptance ΔA
3.31	2.22	4.01	2.28

Table 2.2: PDF Uncertainty on the W production cross-section $\Delta\sigma$, and acceptances ΔA.

	W^-									W^+								
	No cut			Cut Region 1						No cut			Cut Region 1					
PDF Set	σ (pb)	$\Delta\sigma_+$	$\Delta\sigma_-$	σ (pb)	$\Delta\sigma_+$	$\Delta\sigma_-$	A	ΔA_+	ΔA_-	σ (pb)	$\Delta\sigma_+$	$\Delta\sigma_-$	σ (pb)	$\Delta\sigma_+$	$\Delta\sigma_-$	A	ΔA_+	ΔA_-
CTEQ6.5	9195	501	482	1787.3	57.5	59.1	0.185	0.0028	0.0041	12560	672	691	2107.26	84.4	83.5	0.158	0.0033	0.0036
MRST2006	9206	294	344	1824.2	15.0	67.0	0.189	0.0027	0.0054	12379	459	380	2106.42	23.7	45.9	0.160	0.0010	0.0031
CTEQ6.1	8552	504	503	1671.1	64.6	98.9	0.187	0.0014	0.0058	11637	763	589	1944.12	115.6	61.4	0.157	0.0047	0.0028
MRST2004 (NNLO)	8702	284	292	1681.8	48.4	22.7	0.184	0.0045	0.0011	11798	397	386	1983.64	56.9	26.5	0.159	0.0028	0.0024
MRST2004 (NLO)	8747	286	294	1703.3	49.1	23.0	0.186	0.0045	0.0011	11655	392	382	1949.68	56.0	26.1	0.157	0.0028	0.0024
MRST2001	8695	284	292	1676.7	48.3	22.6	0.184	0.0045	0.0011	11743	395	385	1937.29	55.6	25.9	0.156	0.0028	0.0024
	No cut			Cut Region 2						No cut			Cut Region 2					
PDF Set	σ (pb)	$\Delta\sigma_+$	$\Delta\sigma_-$	σ (pb)	$\Delta\sigma_+$	$\Delta\sigma_-$	A	ΔA_+	ΔA_-	σ (pb)	$\Delta\sigma_+$	$\Delta\sigma_-$	σ (pb)	$\Delta\sigma_+$	$\Delta\sigma_-$	A	ΔA_+	ΔA_-
CTEQ6.5	9195	501	482	1907.6	90.2	64.5	0.198	0.0041	0.0002	12560	672	691	2586.6	81.1	95.2	0.193	0.0018	0.0026
MRST2006	9206	294	344	1938.3	38.1	19.4	0.201	0.0035	0.0001	12379	459	380	2568.4	65.4	13.8	0.195	0.0033	0.0016
CTEQ6.1	8552	504	503	1767.4	95.6	64.2	0.197	0.0049	0.0012	11637	763	589	2379.47	120.9	75.9	0.192	0.0023	0.0039
MRST2004 (NNLO)	8702	284	292	1835.2	32.9	31.6	0.202	0.0028	0.0014	11798	397	386	2452.37	49.3	20.8	0.195	0.0019	0.0015
MRST2004 (NLO)	8747	286	294	1846.6	33.1	31.8	0.201	0.0028	0.0014	11655	392	382	2420.16	48.6	20.5	0.195	0.0019	0.0015
MRST2001	8695	284	292	1831.9	32.8	31.5	0.201	0.0028	0.0014	11743	395	385	2418.73	48.6	20.5	0.194	0.0019	0.0015
	No cut			Cut Region 3						No cut			Cut Region 3					
PDF Set	σ (pb)	$\Delta\sigma_+$	$\Delta\sigma_-$	σ (pb)	$\Delta\sigma_+$	$\Delta\sigma_-$	A	ΔA_+	ΔA_-	σ (pb)	$\Delta\sigma_+$	$\Delta\sigma_-$	σ (pb)	$\Delta\sigma_+$	$\Delta\sigma_-$	A	ΔA_+	ΔA_-
CTEQ6.5	9195	501	482	1362.5	41.9	51.8	0.144	0.0025	0.0041	12560	672	691	1572.78	73.0	64.4	0.120	0.0031	0.0030
MRST2006	9206	294	344	1392.4	15.8	56.0	0.147	0.0006	0.0047	12379	459	380	1572.68	25.6	37.8	0.122	0.0007	0.0027
CTEQ6.1	8552	504	503	1265.6	65.5	62.5	0.144	0.0019	0.0034	11637	763	589	1451.63	89.5	43.9	0.120	0.0040	0.0022
MRST2004(NNLO)	8702	284	292	1279.6	44.7	15.1	0.142	0.0040	0.0012	11798	397	386	1476.94	32.5	33.2	0.121	0.0015	0.0031
MRST2004 (NLO)	8747	286	294	1294.7	45.3	15.3	0.144	0.0041	0.0012	11655	392	382	1451.63	31.9	32.6	0.120	0.0015	0.0031
MRST2001	8695	284	292	1273.1	44.5	15.0	0.144	0.0041	0.0012	11743	395	385	1452.54	32.0	32.7	0.119	0.0015	0.0031

Table 2.3: Cross-sections σ for , and acceptances A, with asymmetric Hessian uncertainties as calculated using several recent PDF sets for the three cut regions defined in Table 2.1.

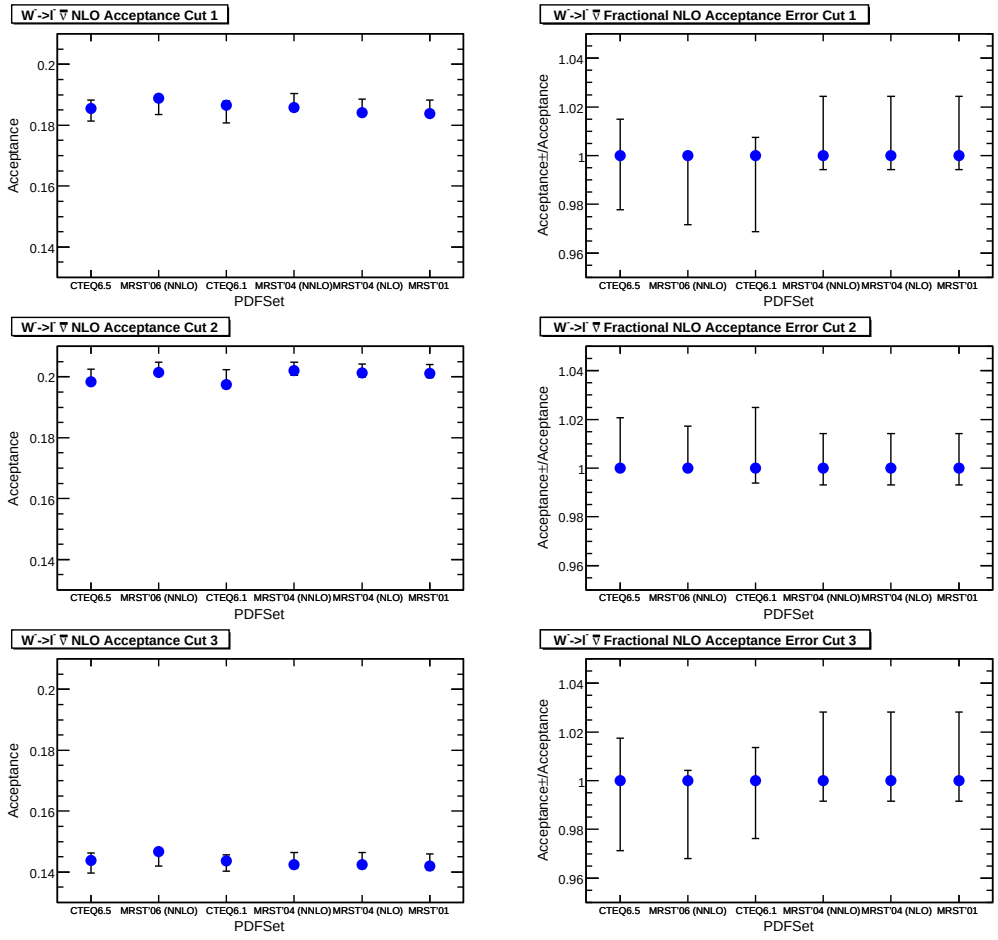

Figure 2.3: Comparison of $W^- \to l^- \overline{\nu}$ ($\ell = e$ or μ) acceptances A, with several recent PDF calculations for acceptance regions (a) Cut 1, (b) Cut 2, and (c) Cut 3, as defined in Table 2.1. The left-hand plots show the total acceptance and the right hand plots show the fractional error on the acceptance.

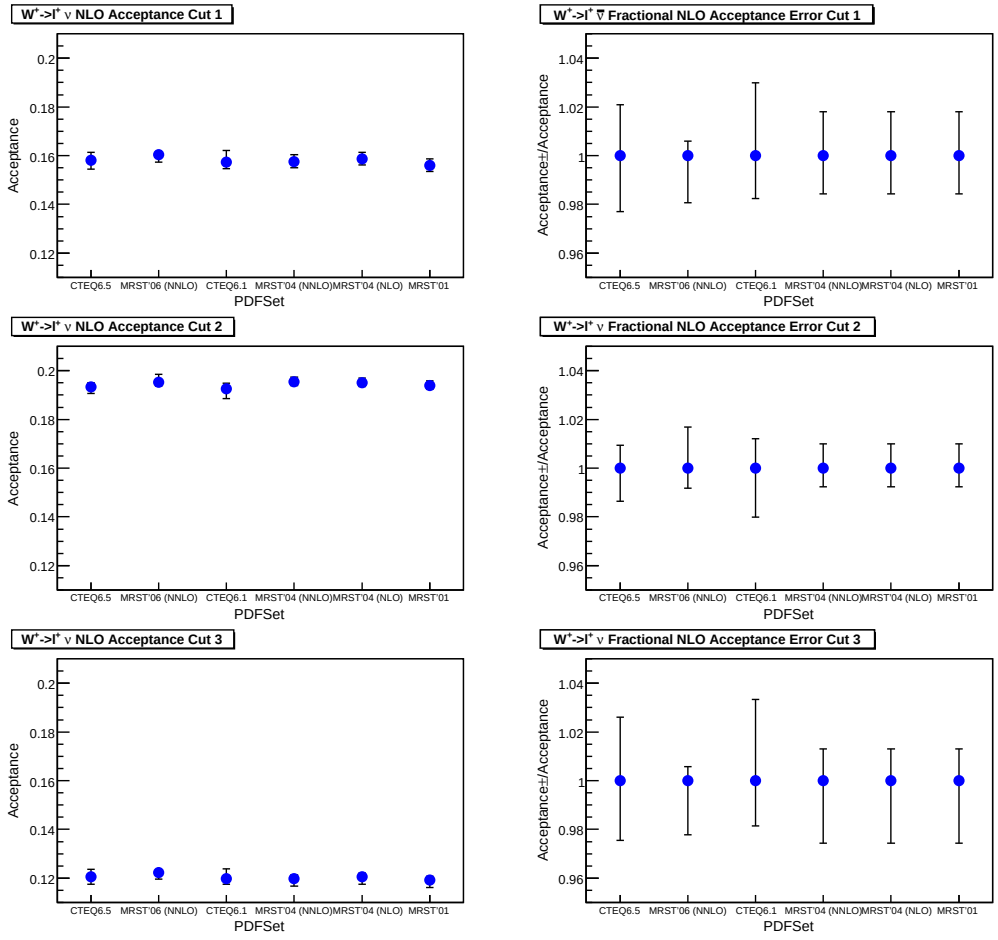

Figure 2.4: Comparison of$W^+ \to l^+\nu$ ($\ell = e$ or μ) acceptances A, with several recent PDF calculations for acceptance regions (a) Cut 1, (b) Cut 2, and (c) Cut 3, as defined in Table 2.1. The left-hand plots show the total acceptance and the right hand plots show the fractional error on the acceptance.

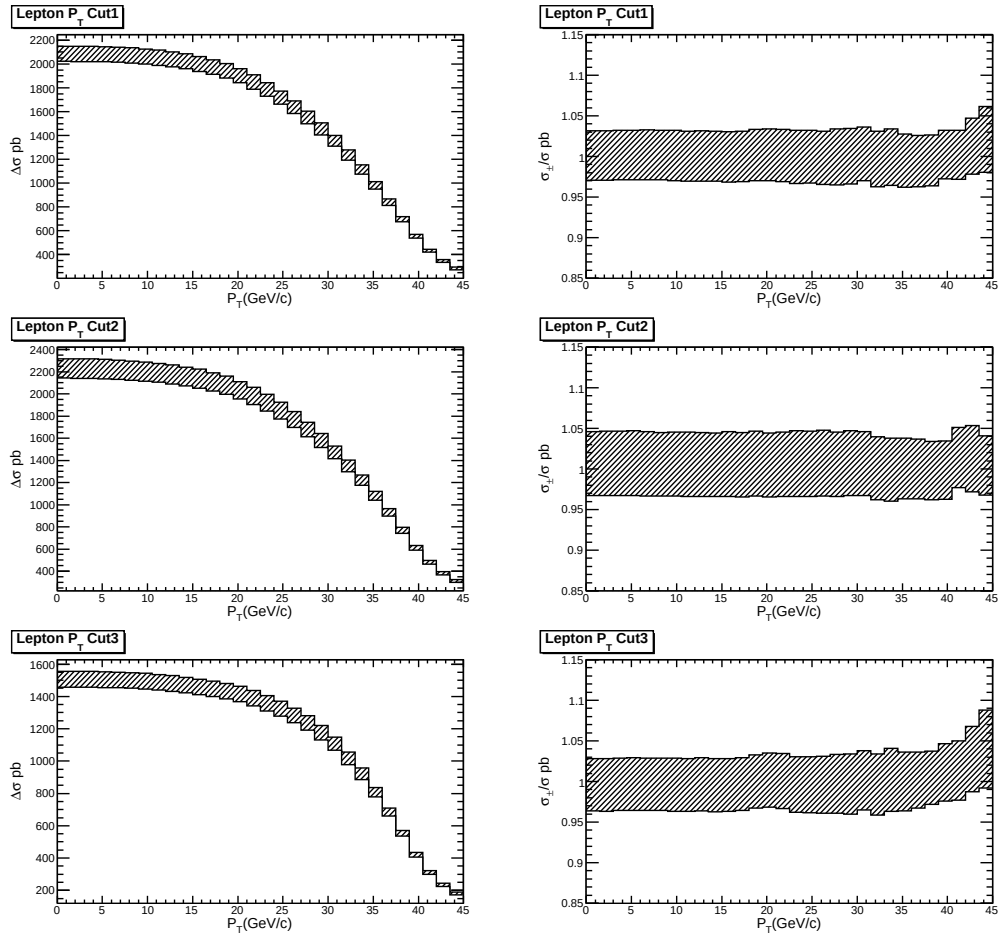

Figure 2.5: The $W^- \to l^- \overline{\nu}$ cross-section σ ($\ell = e$ or μ), as a function of the $p_{\rm T}$ cut for acceptance regions (a) Cut 1, (b) Cut 2, and (c) Cut 3, as defined in Table 2.1. For each acceptance region we fix the invariant mass and $|\eta|$ cuts at their specified values, and vary only the $p_{\rm T}$ cut. The figures on the right show the relative errors in the cross sections.

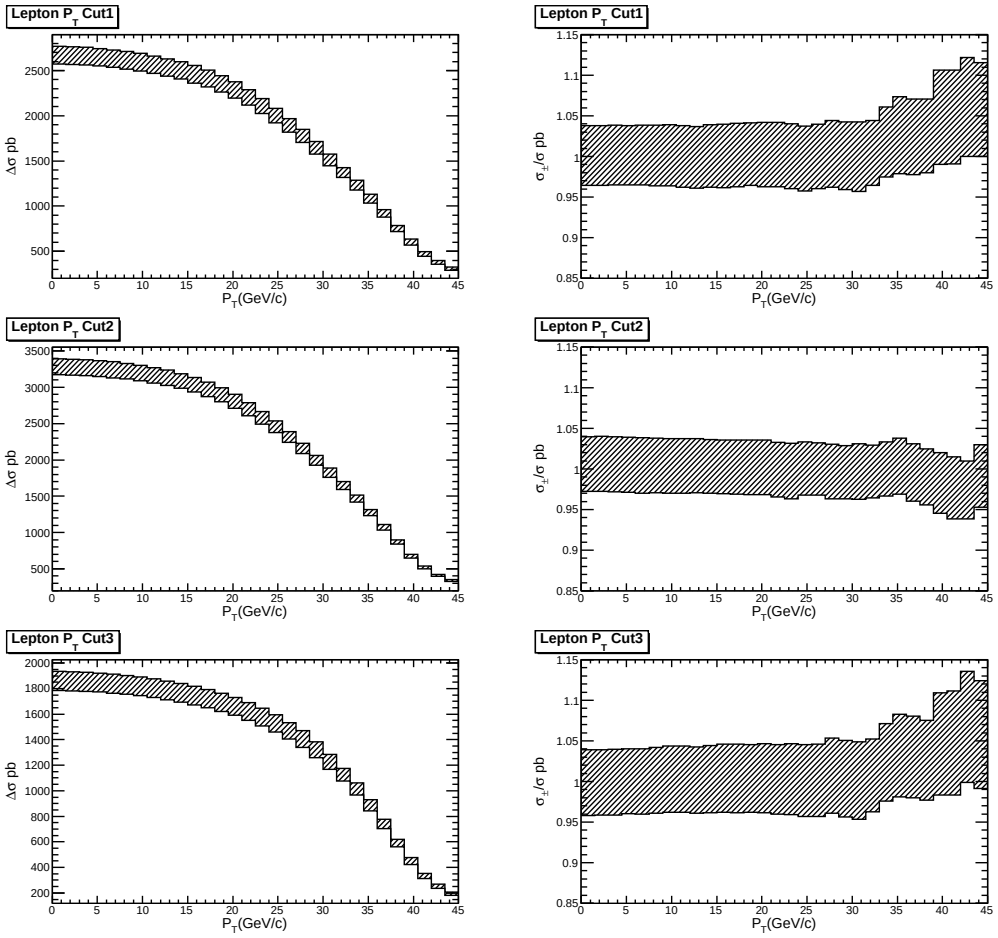

Figure 2.6: The $W^+ \to l^+\nu$ cross-section σ ($\ell = e$ or μ), as a function of the $p_{\rm T}$ cut for acceptance regions (a) Cut 1, (b) Cut 2, and (c) Cut 3, as defined in Table 2.1. For each acceptance region we fix the invariant mass and $|\eta|$ cuts at their specified values, and vary only the $p_{\rm T}$ cut. The figures on the right show the relative errors in the cross sections.

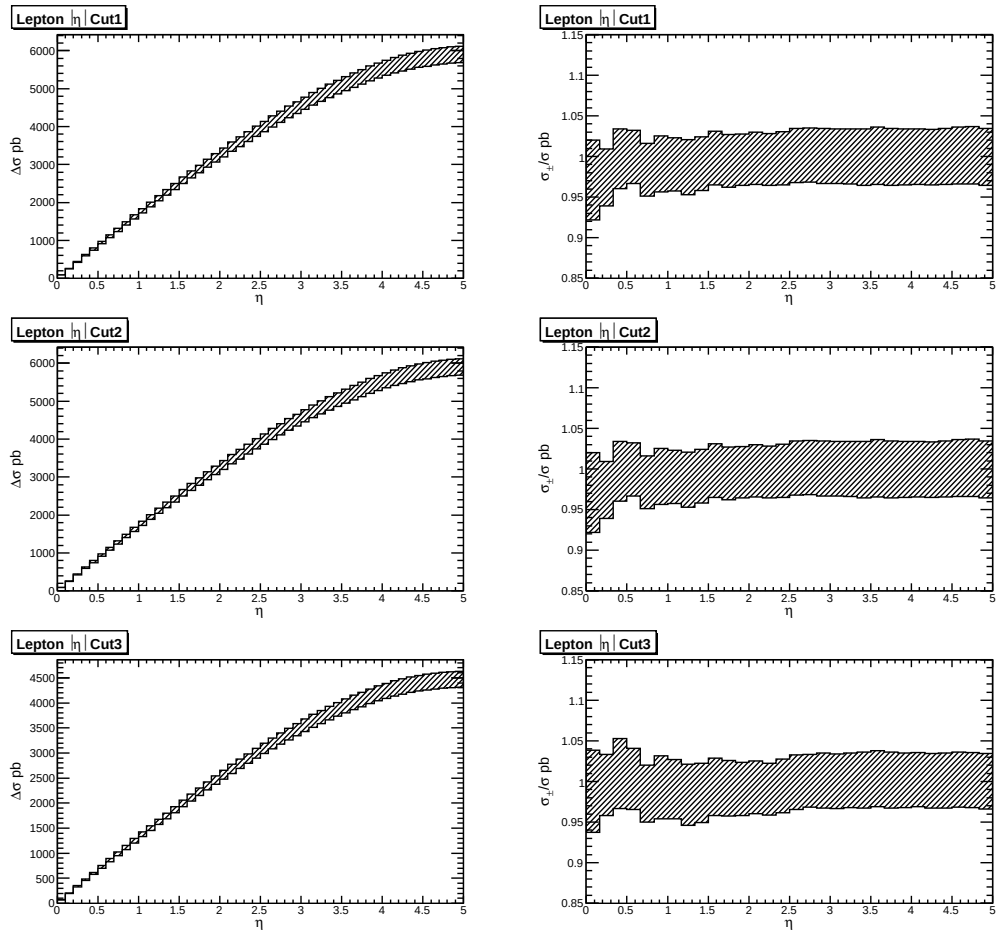

Figure 2.7: The $W^- \to l^- \overline{\nu}$ cross-section σ ($\ell = e$ or μ), as a function of the $|\eta|$ cut for acceptance regions (a) Cut 1, (b) Cut 2, and (c) Cut 3, as defined in Table 2.1. For each acceptance region we fix the invariant mass and $p_{\rm T}$cuts at their specified values, and vary only the $|\eta|$ cut. The figures on the right show the relative errors in the cross sections.

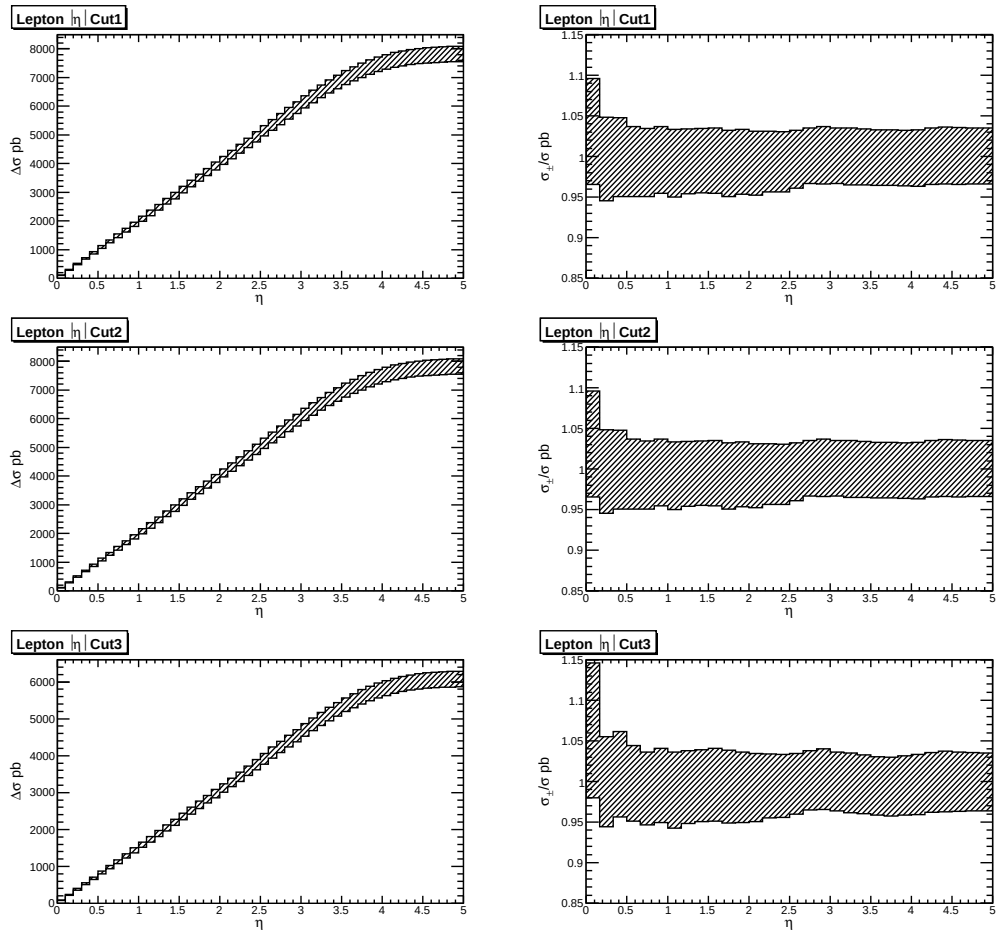

Figure 2.8: The $W^+ \to l^+\nu$ cross-section σ ($\ell = e$ or μ), as a function of the $|\eta|$ cut for acceptance regions (a) Cut 1, (b) Cut 2, and (c) Cut 3, as defined in Table 2.1. For each acceptance region we fix the invariant mass and $p_{\rm T}$cuts at their specified values, and vary only the $|\eta|$ cut. The figures on the right show the relative errors in the cross sections.

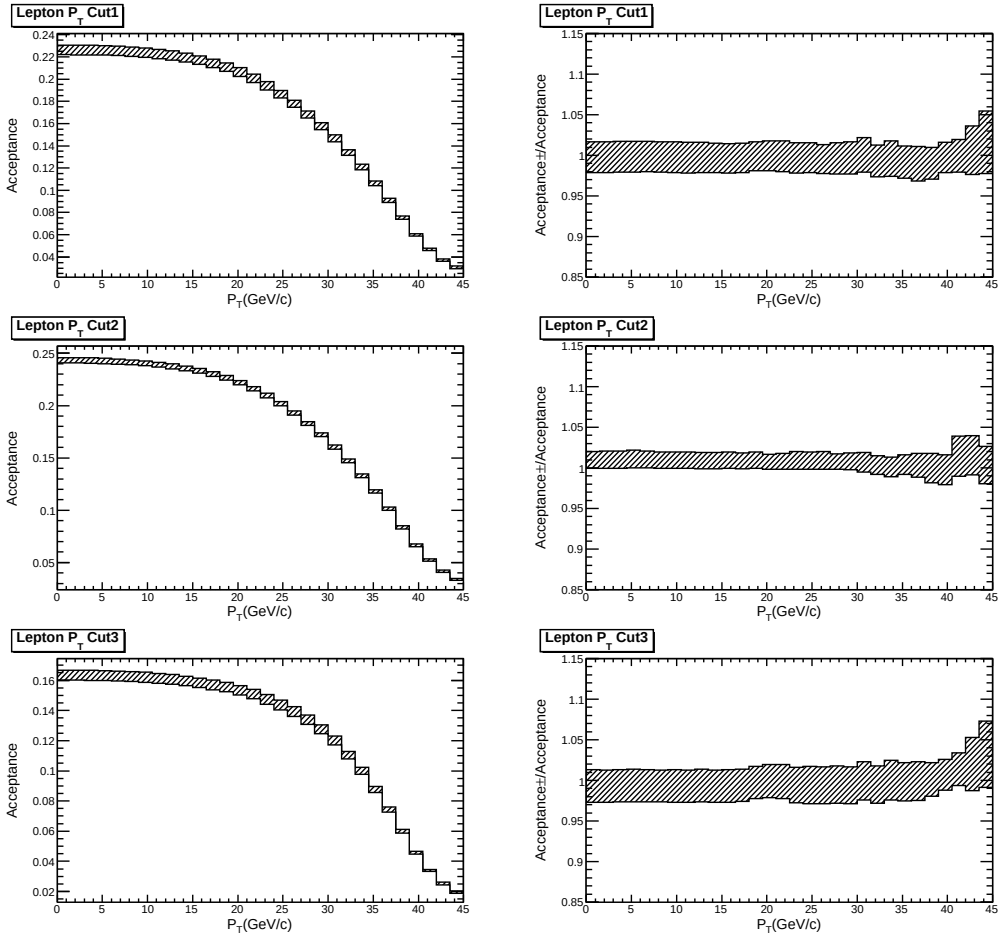

Figure 2.9: The $W^- \to l^- \overline{\nu}$ acceptances ($\ell = e$ or μ) A, as a function of the $p_{\rm T}$ cut for acceptance regions (a) Cut 1, (b) Cut 2, and (c) Cut 3, as defined in Table 2.1. For each acceptance region we fix the missing energy and $|\eta|$ cuts at their specified values, and vary only the $p_{\rm T}$ cut. The figures on the right show the relative errors in the acceptances.

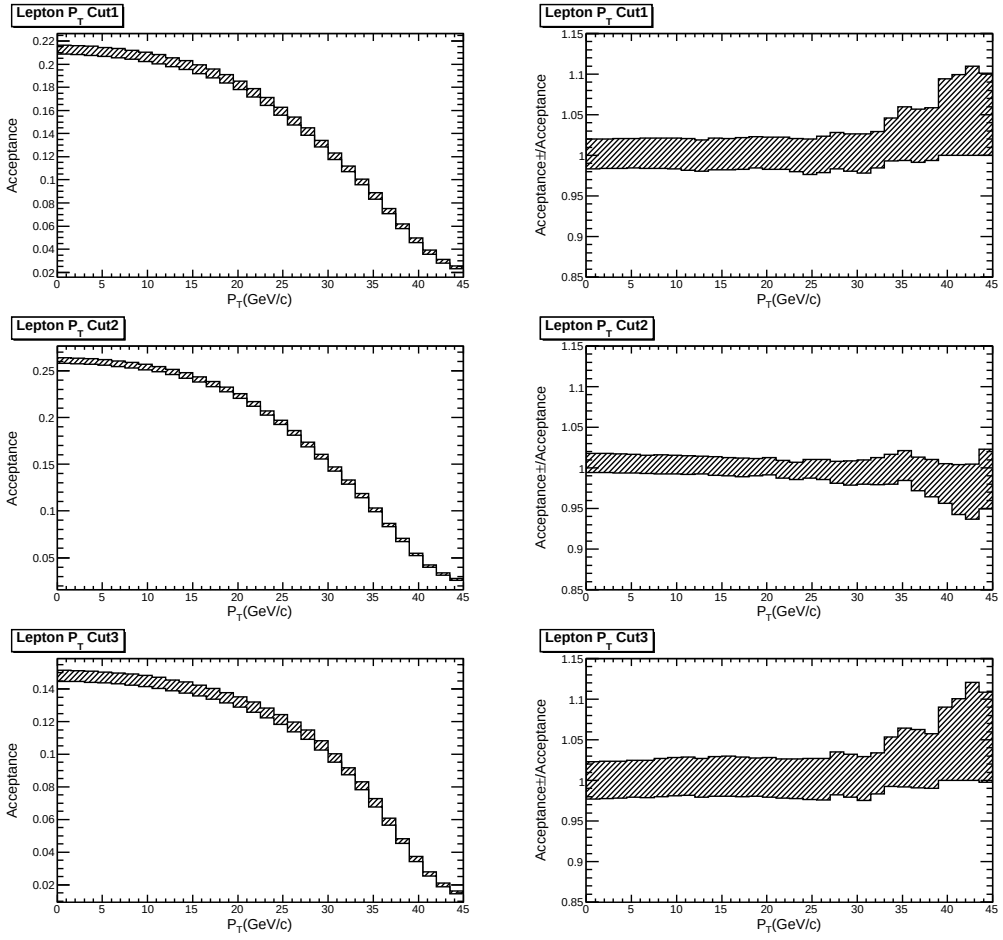

Figure 2.10: The $W^+ \to l^+\nu$ acceptances ($\ell = e$ or μ) A, as a function of the $p_{\rm T}$ cut for acceptance regions (a) Cut 1, (b) Cut 2, and (c) Cut 3, as defined in Table 2.1. For each acceptance region we fix the missing energy and $|\eta|$ cuts at their specified values, and vary only the $p_{\rm T}$ cut. The figures on the right show the relative errors in the acceptances.

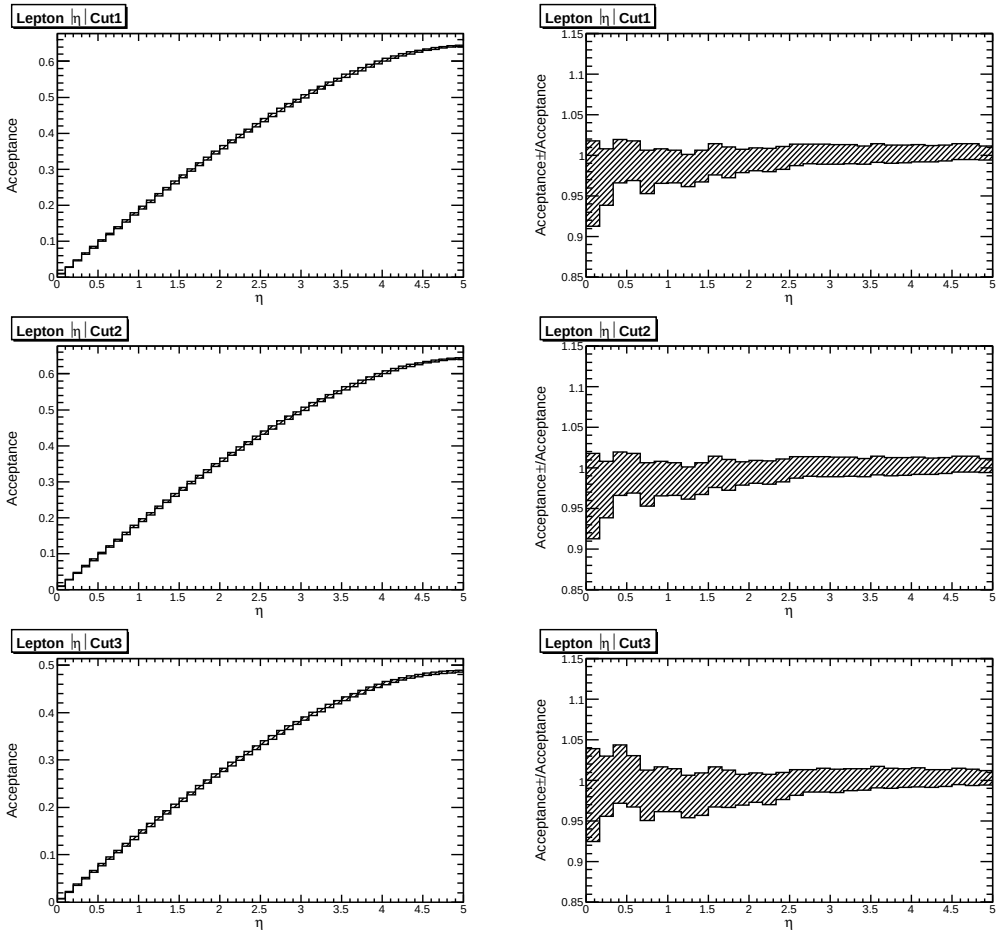

Figure 2.11: The $W^- \to l^- \overline{\nu}$ acceptances ($\ell = e$ or μ)A, as a function of the $|\eta|$ cut for acceptance regions (a) Cut 1, (b) Cut 2, and (c) Cut 3, as defined in Table 2.1. For each acceptance region we fix the missing energy and p_{T}cuts at their specified values, and vary only the $|\eta|$ cut. The figures on the right show the relative errors in the acceptances.

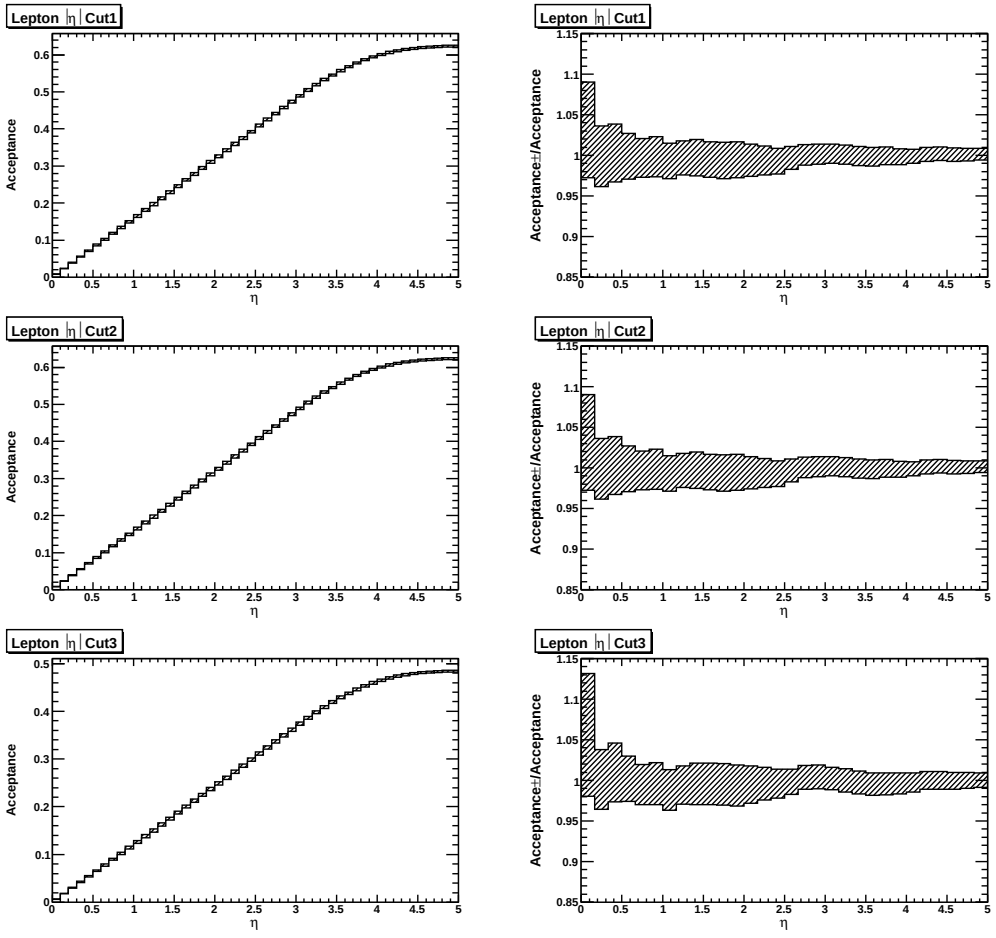

Figure 2.12: The $W^+ \to l^+\nu$ acceptances($\ell = e$ or μ) A, as a function of the $|\eta|$ cut for acceptance regions (a) Cut 1, (b) Cut 2, and (c) Cut 3, as defined in Table 2.1. For each acceptance region we fix the missing energy and p_{T}cuts at their specified values, and vary only the $|\eta|$ cut. The figures on the right show the relative errors in the acceptances.

Chapter 3

Application of Jet Trimming in Boosted Higgs Search

We introduce a new search strategy to look for a light Higgs boson (around 120 GeV) produced with a vector boson the Large Hadron Collider (LHC). The Higgs boson and the vector boson are required to be boosted, while the Higgs boson will decay to $b\bar{b}$ and the vector boson will decay leptonically. By using the Jet Trimming Technique, we will show that the Higgs boson mass resolution is significantly improved. Finally, we will show that statistical significance of this search channel is 4.5 σ for $30fb^{-1}$ data.

3.1 Boosted Higgs boson Search

The Higgs boson search is the most important search at the Large Hadron Collider (LHC), because it is an essential part of the SM electroweak symmetry breaking. As shown in Fig 3.1, current electroweak fits, together with the LEP and Tevatron exclusion limit, favour a light Higgs boson one with mass around 120 GeV [26] [27]. However, the Higgs boson will decay dominantly to $b\bar{b}$ around this mass region as shown in Fig 3.2. It is a challenging task for the discovery of Higgs boson in this mass

region [28] [29].

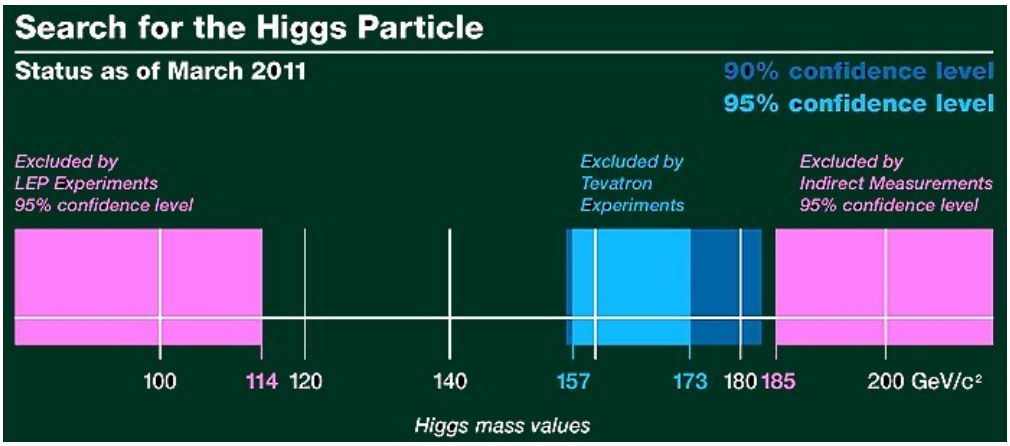

Figure 3.1: The current limit on the Higgs boson mass from LEP and Tevatron.

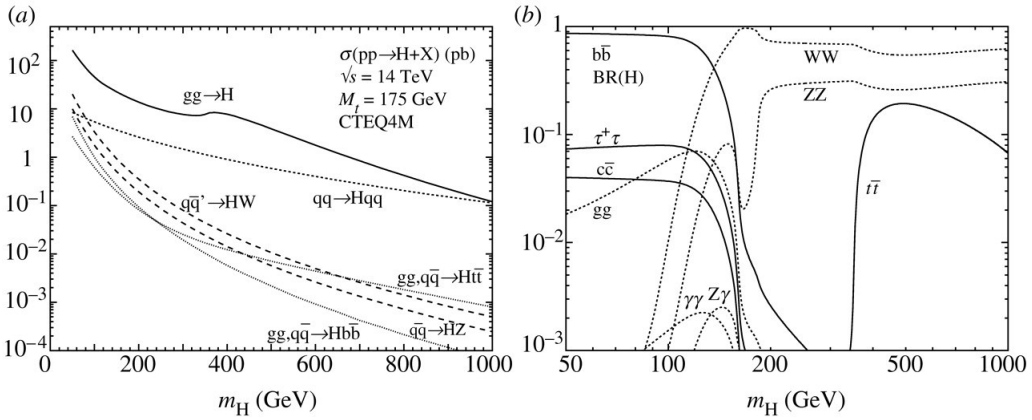

Figure 3.2: The Higgs boson Production Cross Section and Decay Branch Ratio at 14 TeV.

However, the Mass Dropping and Filtering method introduced in [31] revived this search channel.The Higgs boson will decay hadronically into two b-tagged jet with the vector boson decaying leptonically as shown in Fig 5.3. The dominant background for this process is VV,Vj and $t\bar{t}$. In [31], The statistical significance with 30 fb^{-1} after all the cuts is 4.5. In this study, we will employ a similar kinematic selection to [31], but we will reconstruct the Higgs boson using the jet trimming technique [30].

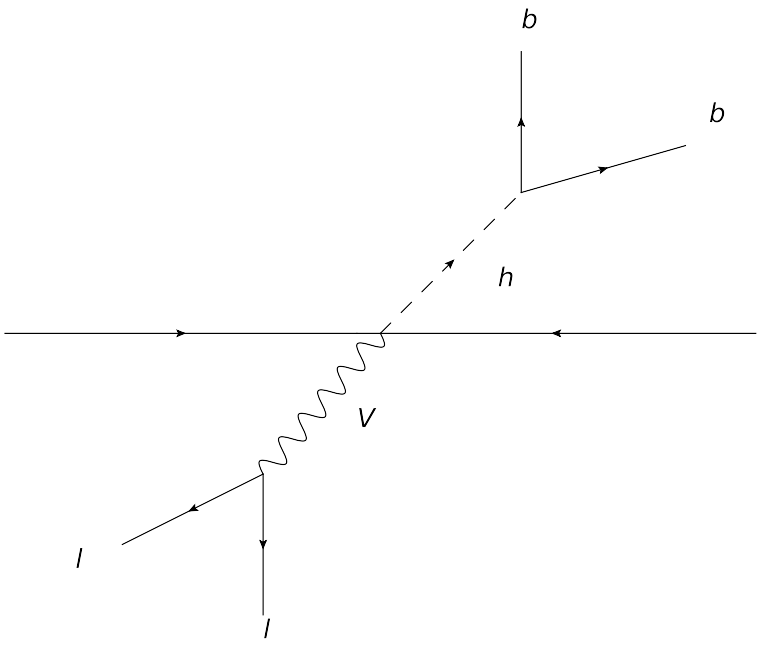

Figure 3.3: Demonstration of Higgs boson Production with a vector boson where the Higgs boson decays to a pair of bottom quark and the vector boson decays leptonically.

3.2 Jet Trimming

Jet Trimming [30] is a designated procedure for removing the ISR/MI/Pileup from the FSR. The intrinsic idea is that ISR/MI/Pileup will be much softer than the FSR. Therefore, we will form a fat jet using a larger cone and then recluster the fat jet with a smaller cone and throw away the softer subjets as shown in Fig 3.4.

We will make some changes to the original algorithm described in [30] for the jet substructure of the boosted Higgs boson. First, we will find the two b-tagged jets by clustering the jet constituents of the fat jet. Also, the Higgs jet, different from a QCD jet, is a dipole itself, so we expect to have more radiation between the two b quarks as shown in Fig 3.5. Therefore, we will use a dynamical f_{cut}, which is proportional to the distance between the subjet and the fat jet.

The jet trimming algorithm proceeds as follows:

- Cluster all the final state particles with Fastjet 2.4.2 [34] antik_T algorithm with

a cone size 1.2.

- Cluster the particles in the hardest jet with a smaller cone size 0.3 with antik_T algorithm to find out the hardest two subjets, and we will require each of the two subjets to be b tagged. We assume a 60% tagging efficiency and 2% of mis-tagging efficiency.

- Cluster the remaining particles with an even smaller cone size 0.2 with k_T algorithm to form the subjets.

- If $p_T^i > f_{\text{cut}} p_T \Delta R$ the subjet is kept otherwise it is trimmed, p_T is the p_T of the fat jet and ΔR is the distance between the subjet and the fat jet. The f_{cut} is chosen to be 0.03 in this analysis.

- Now we have the Higgs Candidate. We will require the Higgs Candidate p_T larger than 200 GeV and η less than 2.5.

The Higgs Mass spectrum before and after trimming is shown in Fig 3.5. The trimming procedure improve the Higgs mass resolution significantly.

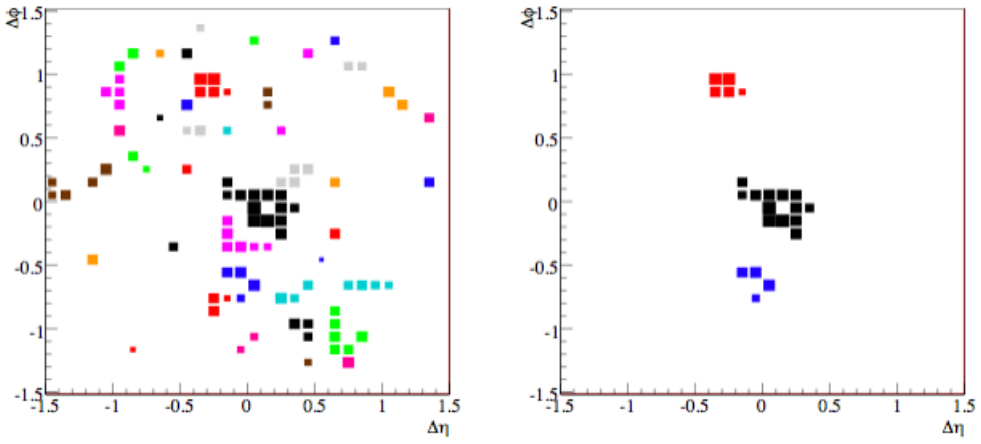

Figure 3.4: Demonstration of the Jet Trimming Technique.

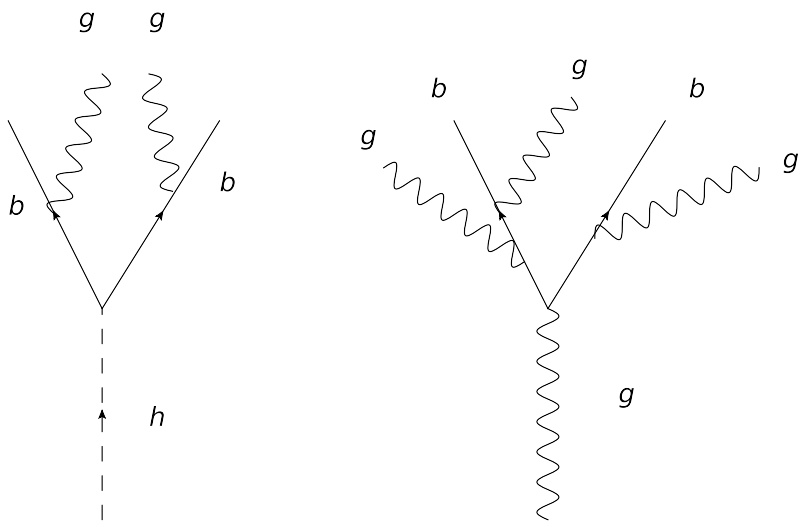

Figure 3.5: Comparison of the radiation pattern of the two bottom quarks from the Higgs boson(Left) and the gluon(Right).

3.3 Results

The events are generated by Pythia 6.403 [116], fully showered and hadronized. The underlying event is incorporated by Pythia "DW" tune. For this analysis, signal samples of WH, ZH are generated, as well as $WW, ZW, ZZ, Z + \text{jet}, W + \text{jet}, t\bar{t}$ to study backgrounds.

There are three search channels in this analysis and the channel specific cuts are very similar to [31]:

- Leptonic channel: Two opposite sign lepton (e or μ) with $p_T > 30$ GeV and $|\eta| < 2.5$, with an invariant mass between 80 and 100 GeV.
- Missing E_T channel: Missing Transverse momentum$>$ 200GeV.
- Semi-leptonic Channel: Missing transverse momentum$>$ 30GeV plus a lepton (e or μ) with $p_T >$ 30GeV. Veto event if there is jet with $p_T > 30$ GeV and $|\eta| < 3.0$.
- all channel: No more lepton with $p_T > 30$ GeV and $|\eta| < 2.5$ except to recon-

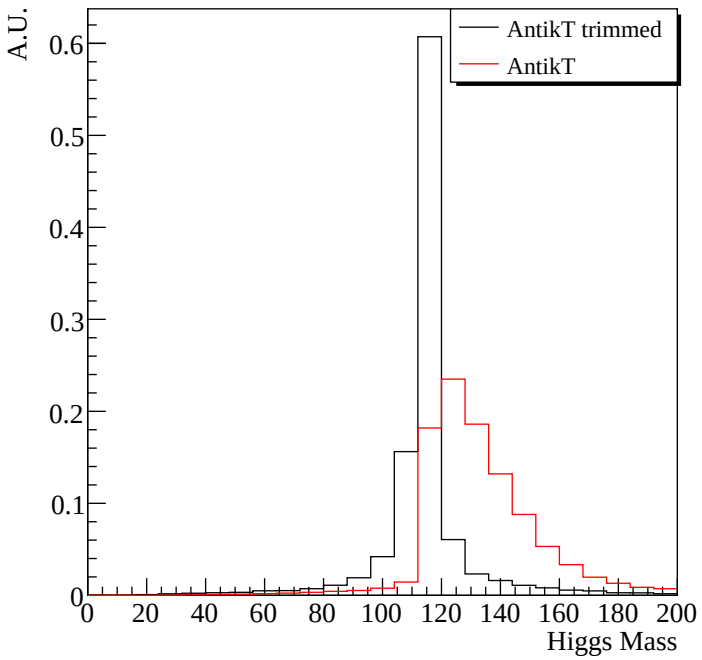

Figure 3.6: The Higgs Mass spectrum with and without trimming.

struct the vector boson, no more b-tagged jets with $p_T > 30$ and $|\eta| < 2.5$.

The mass spectrum of the Higgs Candidate with m_H =115 GeV is shown in Fig 3.7 for the three sub-channel and combined channel. The number of both signal and background for Higgs Mass between 112-128 GeV for $30 fb^{-1}$ data is shown in Table 3.1, the significance is 4.5 σ(8.2σ for 100 fb^{-1}). The result is comparable to [31] and offer an alternative strategy for search for boosted Higgs.

Channel	Signal	V+Jet	$t\bar{t}$	VV	S/B	S/$\sqrt{B}$
Leptonic	5.4	10.0	0.032	0.53	0.51	1.66
Missing E_t	24.3	65.6	12.9	3.4	0.3	2.7
Semi-leptonic	30.6	35.0	49.9	1.6	0.35	3.3
Total	60.3	110.60	62.8	6.5	0.34	4.5

Table 3.1: Signal and Background for a 115 GeV SM Higgs boson for 30 fb^{-1}.

3.4 Conclusion and Outlook

Here we have applied jet trimming technique to the boosted Higgs boson search for a low mass (115 GeV) SM Higgs boson. The statistical significance for $30 fb^{-1}$ data is 4.5 σ, which is comparable to the previous result [31]. This could be considered as an alternative search strategy for the high-p_T WH,ZH channel at the LHC.

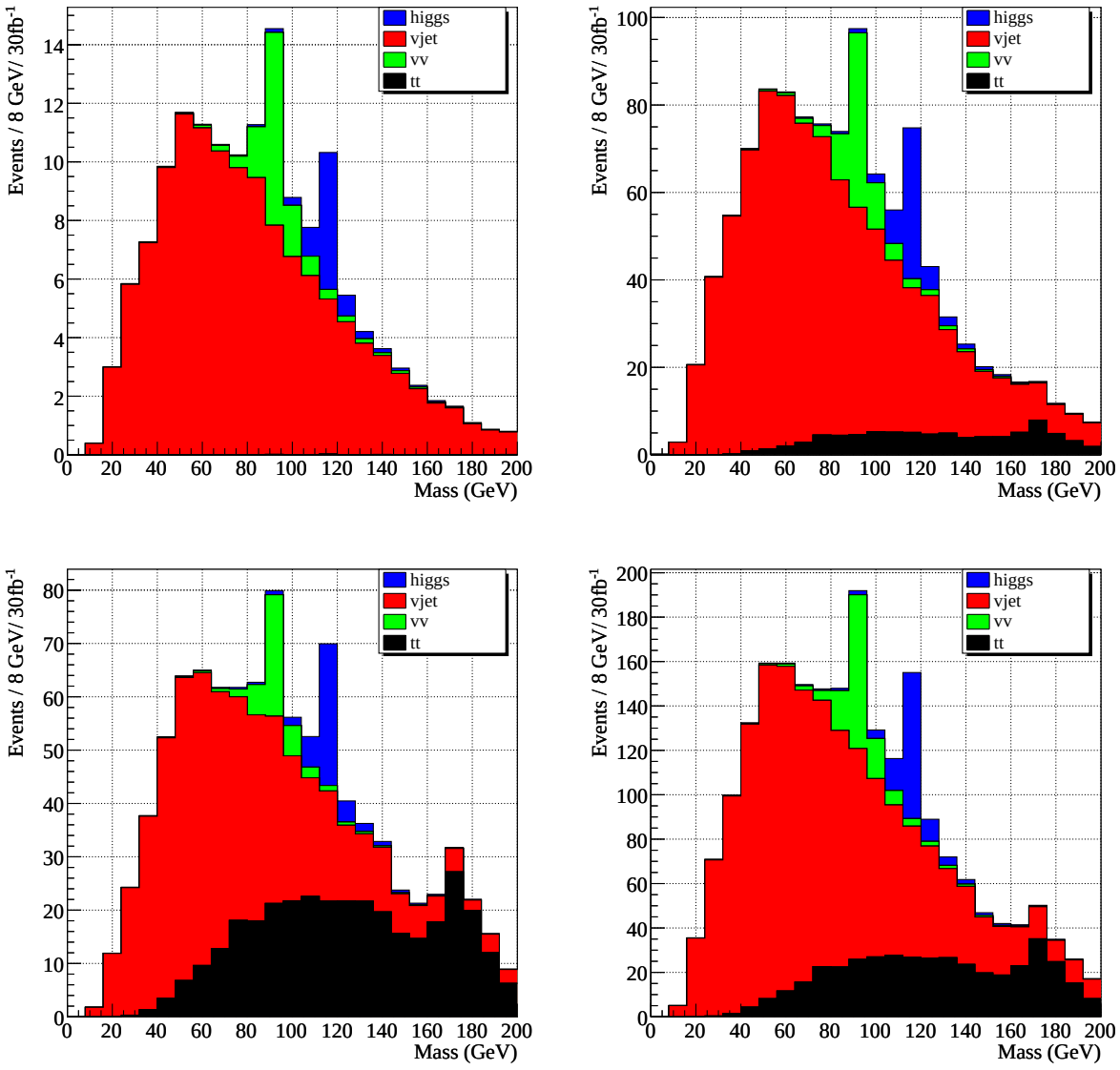

Figure 3.7: The Signal and Background for a 115 GeV SM Higgs boson for 30 fb^{-1}. On the top, the left plot is or leptonic channel and the right plot is for missing Et channel. On the bottom, the left plot is for semi-leptonic channel and the right plot is the total signal and background for all the channel.

Chapter 4

New Physics Signals in Longitudinal Gauge Boson Scattering at the LHC

We introduce a novel technique designed to look for signatures of new physics in vector boson fusion processes at the TeV scale. This functions by measuring the polarization of the vector bosons to determine the *relative* longitudinal to transverse production. In studying this ratio we can directly probe the high energy E^2-growth of longitudinal vector boson scattering amplitudes characteristic of models with non-SM interactions. We will focus on studying models parameterized by an effective Lagrangian that include a light Higgs boson with non-SM couplings arising from TeV scale new physics associated with the electroweak symmetry breaking, although our technique can be used in more general scenarios. We will show that this technique is stable against the large uncertainties that can result from variations in the factorization scale, improving upon previous studies that measure cross section alone.

4.1 Vector Boson Fusion as a Probe of New Physics

The Large Hadron Collider (LHC) was built to elucidate the physics behind electroweak symmetry breaking (EWSB). In a sense, it must succeed in finding some new physics because the partial wave amplitudes for $V_L V_L \to V_L V_L$ scattering,[1] calculated in the absence of a Higgs boson or other new physics, begin to violate unitarity at the TeV scale. Therefore, either new weakly-coupled light particles must come in to guaranty the unitary of the amplitude the amplitudes, or we will see new strong interactions in the electroweak sector.

While many models of EWSB have been proposed, precision experiments such as LEP seem to favor a model employing a $\mathcal{O}(100)$ GeV scalar with the quantum numbers and approximate couplings of the SM Higgs boson [35, 37]. Many models of new physics already include such a particle, oftentimes with couplings deviating slightly from those of the SM, *e.g.* little Higgs [36] and holographic Higgs models [38]. Ideally, such models would be identified and studied at the LHC through the production of their intrinsic new particles. However, the finite energy reach and large backgrounds at the LHC could make discovering any new states very difficult.

Thus we will focus on these non-SM light Higgs scenarios, both because they are favored by precision data and because they are perhaps the most difficult to distinguish from the SM. To study these setups we will take a model-independent approach, employing an effective field theory to parameterize the effects of new physics [17, 39, 40, 41, 42, 43]. We will see that the general phenomenology of the Higgs sector is captured by the coefficients of a small number of dimension-6 operators [44, 45], only one of which is relevant to the vector boson fusion process we wish to study.

Vector boson fusion (VBF) is the process in which vector bosons radiated by initial state quarks scatter into vector bosons (see Fig. 4.1). This process is intimately tied

[1] By V_L we denote a longitudinally polarized electroweak vector boson.

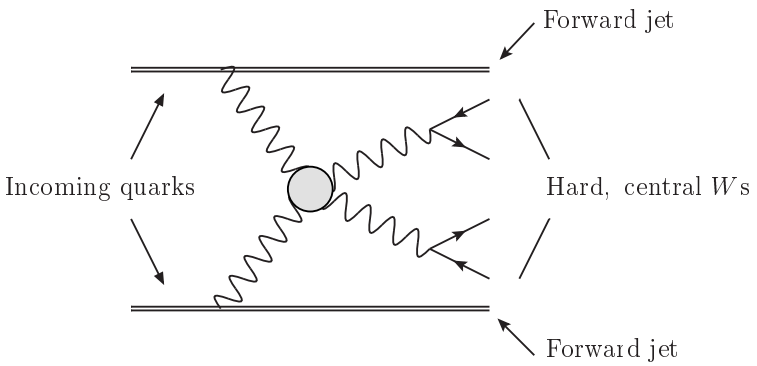

Figure 4.1: Illustration for vector boson fusion.

to EWSB: just as the pion is a Nambu-Goldstone boson (NGB) and $\pi\pi$ scattering can be used to understand chiral symmetry breaking, at high energies longitudinally polarized vector bosons take on the behavior of the NGBs from EWSB. In the absence of a Higgs boson or other new physics responsible for the EWSB, the scattering amplitudes probed by VBF would violate perturbative unitarity [46, 47, 48, 49] at around 1 TeV (see the discussion in appendix A). Furthermore, if the Higgs boson does not have the *exact* couplings to vector bosons as predicted by the SM, then the necessary cancelations will not occur and one will still observe an E^2 growth in the amplitudes until new physics comes into play. It is by measuring this growth that we can hope to observe the effects of physics beyond the SM, even in scenarios where we only see a light Higgs-like particle [45, 50].

In this article we will introduce a novel technique designed to analyze VBF processes and observe the E^2 growth in longitudinal gauge-boson scattering amplitudes mentioned above. We will begin by introducing our notations and framework in Section 4.2. In Section 4.4 we will describe our technique designed measure the *relative* production of transverse to longitudinal modes, focusing on the fully reconstructable semi-leptonic decay of the VV system. We will demonstrate that this measurement is sensitive to anomalous Higgs-gauge couplings while at the same time being robust against the scale uncertainties that challenge cross section measurements. Section 4.5

contains our conclusions.

4.2 Theoretical Setup

In the formulation of a general effective theory of the SM-like Higgs sector [17, 39, 44] most of the operators are tightly constrained [40, 41, 42, 43] because of their otherwise excessive contributions to the electroweak observables, such as the ρ-parameter, oblique parameters, and triple gauge boson self-interactions. There are only two dimension-six operators that are genuine interactions in the Higgs sector not subject to the stringent experimental constraints,[2] $\partial^\mu(H^\dagger H)\partial_\mu(H^\dagger H)$ and $(H^\dagger H)^3$. We note that as both operators are composed from the singlet operator $H^\dagger H$ they may serve to probe not only EWSB physics, but also other physics beyond the SM. For a given theoretical framework, the coefficients of these operators may be calculable [45], and by measuring them we can hope to learn about any new physics. Even in some strongly coupled models for which these may not be calculable, the measurement of a non-zero value can give important clues to the structure of new physics. Now, the second operator above does not have derivative couplings, so its effect on the behavior of the V_L scattering amplitudes at high energies should be sub-leading [44]. We therefore focus on the former and parameterize it (following [45]) as

$$\mathcal{L} \supset \frac{c_H}{2f^2}\partial^\mu(H^\dagger H)\partial_\mu(H^\dagger H), \tag{4.1}$$

where the coefficient c_H is naturally of $\mathcal{O}(1-4\pi)$ depending on whether the underlying theory is weakly or strongly coupled, and f is the characteristic scale of new physics, typically expected to be round $4\pi v$ if the new physics is associated with EWSB.

[2] As discussed in [51], the first of these operators can induce corrections to the oblique parameter S [52], leading to $\sim 2\sigma$ deviations in S for the range of anomalous couplings included here. However, shifts in S can be compensated for by the presence of additional heavy states. We thus believe that these parameters should still be considered viable.

Upon expanding around the electroweak VEV v, this operator contributes terms which add to the kinetic terms of H. After imposing canonical normalization on the fields, the result is a modification to the Higgs couplings. Ref. [45] parameterizes the resulting modified Higgs-gauge coupling in the zero-momentum limit as

$$g_{\text{eff}} = \frac{g_{\text{SM}}}{\sqrt{1 + c_H \xi}} \approx g_{\text{SM}} \left(1 - \frac{c_H}{2}\xi\right) \tag{4.2}$$

where $\xi = v^2/f^2$. This modified coupling has important phenomenological consequences because it deviates from the SM prediction. At high energies and for $|c_H \xi| \gtrsim 0.1$ [3] this modification leads to an incomplete cancelation in the amplitude for longitudinal vector boson scattering and the cross section grows as

$$\sigma(V_L V_L \to V_L V_L) \approx \left(\frac{c_H}{2}\xi\right)^2 \sigma(V_L V_L \to V_L V_L)_{\text{no-higgs}}. \tag{4.3}$$

which can be seen by considering the NGB scattering as shown in appendix A. In what follows we will study means of measuring this behavior. Note that, as discussed in appendix A, the $W_L^+ W_L^-$ scattering amplitudes calculated in this framework violate perturbative unitarity when

$$s_{WW} \approx \frac{16\pi v^2}{c_H \xi \left(1 - \frac{c_H \xi}{4(1+c_H \xi)}\right)}. \tag{4.4}$$

This is the point at which we expect new physics to come into play. In what follows we will limit our analyses to

$$\sqrt{s_{VV}} < 2 \text{ TeV}. \tag{4.5}$$

This corresponds to a coupling value $|c_H \xi| \sim 0.6$. We will take this as an upper limit for our analyses. Of course, looking beyond this energy range would be interesting

[3] For smaller values of $|c_H \xi|$ the dominant non-SM effects enter as interference terms proportional to $c_H \xi$ rather than $(c_H \xi)^2$. Also, in this case the anomalous energy dependence of the longitudinal cross section goes as E^2 instead of E^4.

and should be attempted at the LHC, but any deviation from the SM expectation would no longer carry the same effective Lagrangian interpretation. Also, note that for larger couplings and lower scales of new physics some higher dimensional operators could become relevant and it would be more appropriate to think of the $c_H\xi$ used in our analysis as parameterizing a new physics form factor, rather than as the coefficient of a particular operator.

4.3 Leptonic and Semi-Leptonic Channels Revisited: Scale Uncertainties

The most straightforward way to probe the behavior of Eq. (4.3) would be to measure the resulting increase in VBF cross section at higher energies. This is a well studied topic, with many different analyses having been performed (see, for instance, [55, 53, 54, 56, 57, 58, 59, 60, 61, 62, 63, 64, 65, 66]). Here we will revisit these analyses taking into account the effects of parton showering. We will see that while the cuts developed in past analyses remain essential in suppressing background and isolating VBF signals, one encounters large factorization scale uncertainties that affect rate measurements and must be overcome to detect new physics in VBF.

Sophisticated acceptance cuts have been developed to suppress the SM background and isolate the longitudinal gauge boson scattering in VBF processes at high energies. It has been a common practice to impose a high p_T cut on the reconstructed gauge bosons or their decay products, require one or two forward (backward) energetic jets, and demand that the central detector region remain relatively free of hadronic activity. The first few cuts ensure that we observe hard scattering processes with the gauge bosons emitted by energetic quarks [67, 68, 69], while the last cut is designed to reduce background by taking advantage of the fact that VBF is a purely electroweak process with no color exchange [70] and V_LV_L scattering tends to produce fewer central jets

than other electroweak processes [56]. Using this sort of cut, it was concluded [55, 53] that reasonable sensitivity can be achieved for TeV scale strongly interacting new physics at the 14 TeV LHC with an integrated luminosity of 100 fb^{-1}.

We revisit the WW analyses with the theoretical framework as discussed in the previous section. We consider both fully leptonic [55] and semi-leptonic [53] decays of the vector bosons. For the sake of illustration, we concentrate on the W^+W^- final state. Our VBF parton-level results are generated using the full $2 \to 6$ matrix element for

$$qq' \to qq'W^+W^- \to qq'\ \ell^\pm\nu\ f\bar{f}', \tag{4.6}$$

without making the effective W approximation [71, 72, 73]. In so doing, wherever appropriate, we have included other $\mathcal{O}(\alpha_{EW}^6)$ processes as background to the channels. Our PDFs are those of MRST2004 [74]. To generate the jet-level samples we shower parton-level results using `Pythia 6.4.21` [116] with a virtuality ordered shower, cluster the visible final state particles into 0.1×0.1 $y - \phi$ cells between $-5 \leq y \leq 5$, and produce $R = 0.7$ anti-k_T [113] jets using FastJet [102]. To sample PDFs and shower our results we must choose a factorization scale for the gauge boson scattering processes. The natural choice of the factorization scale is of the order of m_W, with corrections from the p_T of the scattering quarks. We parameterize the choice of scales via

$$\mu^2 = \beta^2 \left(m_W^2 + \frac{1}{2} \sum_{\text{jets}} p_T^2 \right), \tag{4.7}$$

where β is an $\mathcal{O}(1)$ parameter.

We begin by adopting the selection cuts of [55] to study the fully leptonic W^+W^- final state, as detailed in Table 4.1. Using these cuts, we calculate the parton level cross sections for a light Higgs scenario[4] with various anomalous couplings parame-

[4]Here and henceforth, we will take a light Higgs boson mass as $m_H = 100$ GeV for illustration and for comparing with the early studies in the literature. This will make no numerical difference with other m_H values as long as it is well below the $2m_W$ threshold.

Leptonic Cuts	Jet Cuts
$\lvert y(l)\rvert < 2.0$	$E(j_{\text{tag}}) > 0.8$ TeV
$p_T(l) > 100$ GeV	$3.0 < \lvert j_{\text{tag}}\rvert < 5.0$
$\Delta p_T(ll) > 440$ GeV	$p_T(j_{\text{tag}}) > 40$ GeV
$\cos\phi_{ll} < -0.8$	$p_T(j_{\text{veto}}) > 30$ GeV
$M(ll) > 250$ GeV	$\lvert y(j_{\text{veto}})\rvert < 3.0$

Table 4.1: The cuts of [55] for the leptonically decaying W^+W^- final state. The signal selection requires that we tag at least one jet (j_{tag}) and to veto extra central jets (j_{veto}).

terized by $c_H\xi$. The parton level results for a few representative scale choices of β are listed on the left-hand side of Table 4.2. They are consistent with those of [55]. At this level, the uncertainty in rate is only around $\mathcal{O}(10\%)$, which can be attributed entirely to the PDFs. When we include showering, hadronization and jet clustering, the scale μ dictates the virtuality at which the parton shower is started, in addition to controlling the sampling of PDFs. On the right-hand side in Table 4.2, we present the cross sections for the showered and clustered results with a few representative scale choices. We see that the uncertainties can now be as much as $\mathcal{O}(100\%)$. This is because small changes in μ result in large changes in the behavior of the associated forward jets. A higher value of μ could lead to harder radiation that will sink forward jets below the tagging criteria, or it could lead to the parton-shower emission of a veto jet. As the uncertainties from varying the scale ($\beta = 0.5 - 2.0$) would normally set the systematic theoretical errors, such large uncertainties in rate would make it difficult to distinguish the presence of anomalous couplings, even for large values of $c_H\xi$.

We next explore the situation for the semi-leptonic mode of W^+W^- decay. We employ cuts inspired by [53] as shown in Table 4.3. The results of this analysis are shown in Table 4.4, again demonstrating a relatively stable signal at the parton level (left-hand panels) and an $\mathcal{O}(100\%)$ uncertainty at the jet level (right-hand panels).

	Parton Level [fb]			Jet Level [fb]		
$c_H\xi$	$\beta = 0.5$	$\beta = 1.0$	$\beta = 2.0$	$\beta = 0.5$	$\beta = 1.0$	$\beta = 2.0$
0.4	0.015	0.013	0.012	0.015	0.009	0.005
0.2	0.013	0.011	0.010	0.013	0.006	0.004
0.0	0.011	0.090	0.008	0.012	0.007	0.004

Table 4.2: Cross sections [fb] for VBF with W^+W^- final states decaying into e and μ for various anomalous Higgs-gauge couplings and at different factorization scales parameterized by Eq. (4.7). The cuts used to generate these results are those of [55]. The set of cross sections on the left are computed at parton level, while those on the right correspond to results after the parton shower and hadronization.

Pass conditions	Veto conditions
$E(j_{\text{tag}}) > 300$ GeV	$p_T(j_{\text{mini}}) > 25$ GeV
$2 < \lvert y(j_{\text{tag}})\rvert < 5$	$\lvert y(j_{\text{mini}})\rvert < 2$
$p_T(j_{\text{tag}}) > 20$ GeV	130 GeV $< m_{WJ} <$ 240 GeV
$p_T(W_{\text{recon.}}) > 320$ GeV	
$\lvert y(W_{\text{had}})\rvert < 4$	

Table 4.3: W^+W^- semi-leptonic decay cuts inspired by [53]. These require two tagged jets (j_{tag}) and two reconstructed Ws ($W_{\text{recon.}}$). If the events contain two soft, central jets (j_{mini}) they are vetoed. The cut on the jet-W invariant mass is designed to reduce top quark backgrounds.

As with the fully leptonic system considered above, the large uncertainty is once again attributable to the parton-shower treatment of the forward jets using different scales.

We find that VBF cross sections with complicated kinematical cuts are extremely sensitive to the exact scale choice one uses, and it is insufficient to simply characterize the hard scattering with a rough estimate of μ. While we have only considered the effects of varying μ on signal rates, the background is also susceptible to these uncertainties. Even without considering the effects of the veto cut, which can only increase sensitivity to μ, it's natural to associate $\mathcal{O}(2\times)$ K-factors with high multiplicity QCD events. Therefore, before drawing any conclusion about the presence of new physics one would have to understand these systematics. In principle, the theoretical uncer-

	Parton Level [fb]			Jet Level [fb]		
$c_H\xi$	$\beta = 0.5$	$\beta = 1.0$	$\beta = 2.0$	$\beta = 0.5$	$\beta = 1.0$	$\beta = 2.0$
0.4	0.95	0.81	0.73	0.53	0.38	0.26
0.2	0.82	0.72	0.64	0.43	0.33	0.24
0.0	0.73	0.64	0.57	0.40	0.29	0.21

Table 4.4: Cross sections [fb] for VBF with the semi-leptonic decay of W^+W^- for various anomalous Higgs-gauge couplings and at different factorization scales parameterized by Eq. (4.7). The cuts used to generate these results are those of Table 4.3.

tainty may be reduced through higher order calculations that can give us a better idea of the appropriate scale choice. Substantial efforts would be needed both in theory and in experiments before to bring this uncertainty under control. With this in mind, in the next section we will present a new tool to circumvent the difficult issue of the factorization-scale dependence.

4.4 Polarization Measurements

With the uncertainties detailed above as our motivation, we propose a new technique to probe the anomalous couplings in a robust way. Our basic idea is to look for the *relative* increase in longitudinal vector boson production by comparing it to the production of transverse modes. Unlike the overall cross section, which is sensitive to the behavior of the forward jets, the relative transverse to longitudinal production rates should be stable against different scale choices because it depends only on the $VV \to VV$ scattering amplitude. To measure the polarization of a vector boson we need to reconstruct the four-momenta of its decay products and measure their distribution with respect to a polarization axis. If one chooses the polarization axis to be the gauge boson direction of motion (Fig. 4.2), then a simple spin-analysis predicts that in the V rest frame the transverse and longitudinal polarizations will

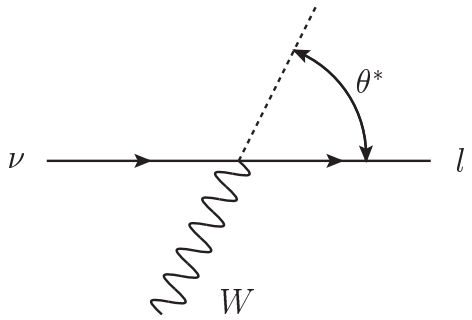

Figure 4.2: The polarization axis used to measure θ^*. Note that this is measured in the rest frame of the W, and the W direction of motion is defined with respect to the WW center of mass.

be distributed as [5]

$$P_{\pm}(\cos\theta^*) = \frac{3}{8}(1 \pm \cos\theta^*)^2, \; P_L(\cos\theta^*) = \frac{3}{4}(1 - \cos^2\theta^*) \tag{4.8}$$

where θ^* denotes the angle between the parton and the gauge boson direction of motion in the gauge boson rest frame. [6]

To measure these distributions experimentally, we need to fully reconstruct the gauge boson pair center of mass and each gauge boson's direction of motion in this frame. To accomplish this we will focus on the semi-leptonic decay channel of the VV system as this allows full reconstruction of the system while minimizing the SM background by requiring leptons and missing energy. The semi-leptonic channel also significantly increases the signal event rate. For this we will rely upon jet substructure techniques to reconstruct the hadronically decaying gauge boson [53]. We will focus on studying the W^+W^- final state, although we will take into account the background from other VBF processes like $W^{\pm}W^{\pm}$ and $W^{\pm}Z$ that enter because we can not distinguish the sign of a hadronically decaying vector, nor can we always distinguish

[5] Note that these distributions can be modified when cuts are placed on the individual W decay products, rather than on the W momenta.

[6] We alert the reader to the fact that θ^* is sometimes also used in the VBF literature (e.g. [53]) to refer to the angle between incoming and outgoing vector bosons.

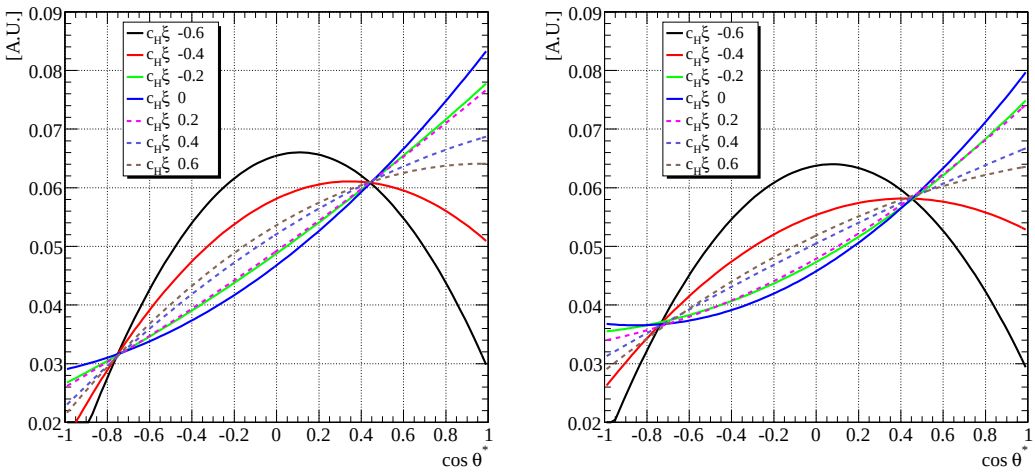

Figure 4.3: The distributions of $\cos\theta^*$ for different anomalous couplings at parton level (left) and for fully showered, hadronized, clustered, and reconstructed events (right). All distributions are normalized to the same area.

a hadronically decaying W from a Z. Later in this section we will comment on the SM $\mathcal{O}(\alpha_S^2)$ and $\mathcal{O}(\alpha_S^4)$ backgrounds.

4.4.1 Leptonic Polarization

We begin with the polarization analysis for the leptonic side of the decay. We first study the parton-level results, then we will turn on the full simulation (parton-showering and jet clustering) to see that they are largely unchanged.

Before proceeding further, we encounter a subtlety in the reconstruction of the leptonic system: While the neutrino four-momentum is constrained by the on-shell W condition, it is only determined up to a discrete ambiguity. One finds two candidate four-momenta at the same azimuthal angle but separated from the charged lepton by a fixed rapidity difference. In what follows we will simply use the average $\cos\theta^*$ value from both solutions as an approximation of the true value. This is acceptable because we are working in a boosted regime where the difference in rapidity between the neutrino and the lepton is small, making the curvature effects from the (y, ϕ)

	Leptonic W		Hadronic W		
$c_H\xi$	f_L^P	f_L^J	f_L^P	f_L^J	σ [fb]
-0.6	0.71	0.70	0.71	0.55	3.38
-0.4	0.49	0.48	0.49	0.40	1.12
-0.2	0.23	0.26	0.23	0.24	0.60
0.0	0.17	0.22	0.17	0.22	0.62
0.2	0.24	0.27	0.24	0.26	0.65
0.4	0.32	0.35	0.32	0.32	0.73
0.6	0.40	0.38	0.40	0.38	0.87

Table 4.5: The fraction of longitudinally polarized vector bosons for different anomalous couplings at parton level f_L^P and jet level f_L^J, reconstructed in hadronic and leptonic decays. Also listed are the jet-level cross sections. These results are after the cuts of Table 4.3.

system sub-leading. The resultant distributions are shown in Fig. 4.3, at parton level (left panel) and after the hadronization (right panel). The characteristic shapes with different couplings are quite distinctive. In Table 4.5 we compute the cross section for each anomalous coupling and fit it to the transverse and longitudinal distributions of Eq. (4.8) using

$$P(\cos\theta^*) = f_L P_L(\cos\theta^*) + f_+ P_+(\cos\theta^*) + f_- P_-(\cos\theta^*) \tag{4.9}$$

where the P are normalized probability distributions of $\cos\theta^*$ and the f are subject to the constraint $\sum f = 1$. As one can see from comparing the jet and parton level figures, the results are remarkably stable under a full simulation.

In Figure 4.4 we plot the projected event distributions and associated statistical errors both for the SM and for an anomalous scenario with $c_H\xi = -0.4$, given 100 fb^{-1} of luminosity. The shape difference between the two samples is clearly visible. To estimate the luminosity necessary to probe a given coupling, one can use that the signal scales roughly as $(c_H\xi)^2$, as discussed before. However, the precise reach of the LHC in discerning anomalous couplings will require a more thorough accounting of

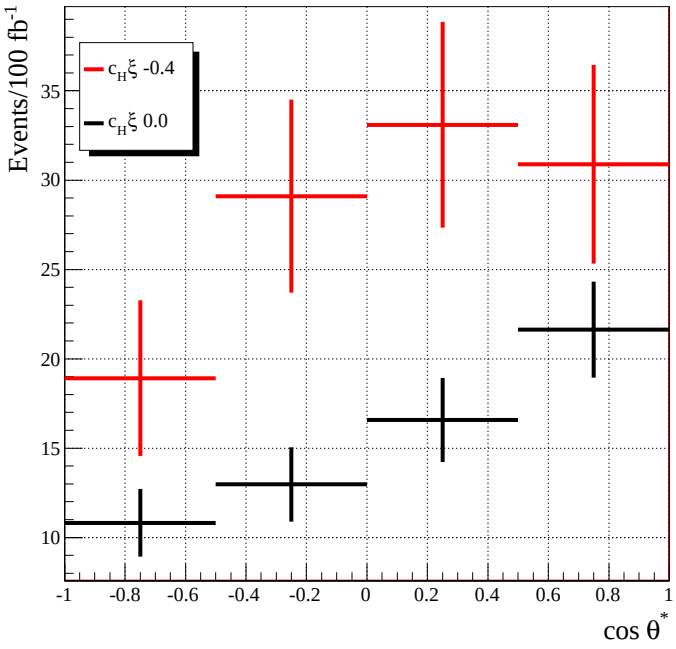

Figure 4.4: Projected distribution and associated statistical uncertainties of $\cos\theta^*$ for the leptonically decaying vector using 100 fb^{-1} of luminosity.

background. Further, we have not made an effort to optimize the statistical power of the analysis and there are other channels that contribute to the signal, such as $W^+W^+, W^\pm Z$ and ZZ. In addition, one can extract more information from each event, as we will now see.

4.4.2 Hadronic Polarization

It is possible to further improve the discriminating power of polarization by considering both sides of the VV system together; by looking for the expected *correlation* between both states one can hope to gain additional discriminating power.

To see the correlation effect, consider Fig. 4.5, which shows the parton-level $\cos\theta^*$ distributions for both sides of the VV system in SM and non-SM scenarios. For now, we plot $\cos\theta^*$ on the hadronic side for the down-type quarks. In the non-SM scenario we see a rapid rise in the central region of the plot near $\cos\theta^* \approx 0$. This indicates

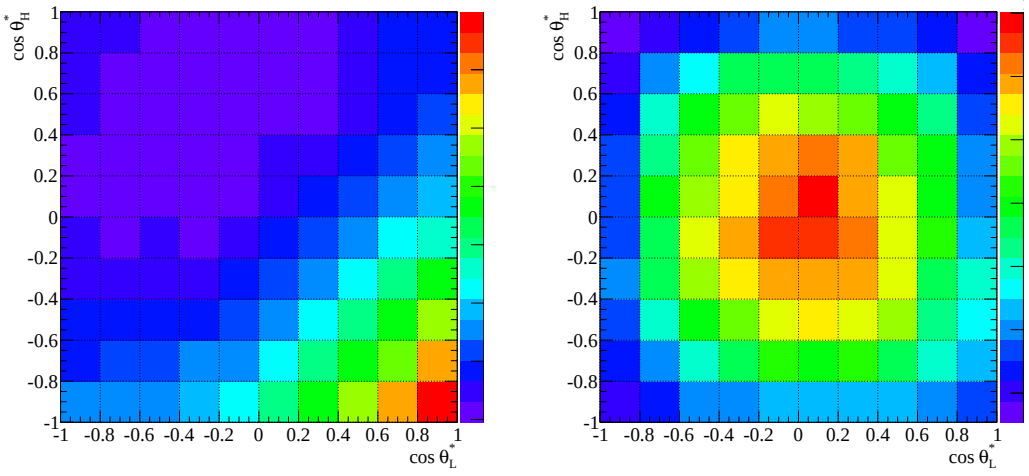

Figure 4.5: Distributions of $\cos\theta^*$ at parton-level for both sides of the VV system (labeled with subscript H and L for hadronic and leptonic decays, respectively). The plot on the left is for the Higgs boson with SM couplings, while the one on the right is for $c_H\xi = -0.6$. The scale is individually normalized for each plot, going from violet to red as the concentration of events increases. The scaling of the color gradient on the right side of each plot is linear.

that the results are correlated; when we see a V_L it is likely to be accompanied by a V_L because only the V_LV_L final state sees the E^2 growth characteristic of with non-SM effects. In practice the situation is slightly more complicated because we cannot label the light quark states once they shower and hadronize (e.g. we cannot distinguish a u from a d), so the distributions we measure are symmetrized. However, the distributions still carry additional discriminating power, as one can see from the distributions in Fig. 4.4.2 and Fig. 4.7, and Table 4.5. Note that in fitting the symmetrized distributions we only fit to data from $0 < |\cos\theta^*| < 0.7$. In the regime where $|\cos\theta^*| \gtrsim 0.7$ one subjet becomes very soft and the technique breaks down (although, of course, the leptonic analysis still works here).

To perform this analysis we had to look at the hadronically decaying V using subjet techniques (for a short overview of jet algorithms and their behavior, see appendix B). In particular, we used the k_T algorithm [75, 76] with $R = 0.25$ to cluster the constituents of each hadronically decaying gauge boson, using the two

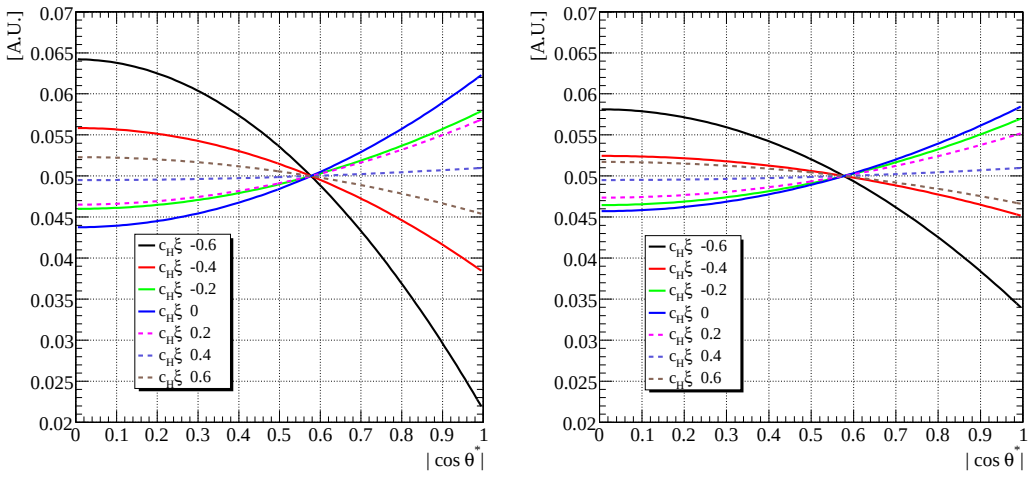

Figure 4.6: Distribution of $|\cos\theta^*|$ at different anomalous couplings for hadronically decaying Ws using parton level samples (left) and fully showered, hadronized samples (right). Note that the distributions differ more at high values of $\cos\theta^*$ because this is the region in which one jet is relatively soft.

most energetic subjets (as measured in the VV center of mass frame) for our analysis. Note that rather than identifying our subjets through a C/A [77, 78] or k_T-like unwinding [31, 79], we used fixed small cones (i.e. small R). Otherwise, the subjets encompass a large area and become more susceptable to contamination from initial state radiation, multiple interactions, and event pileup. The choice of a small cone seems to result in a better reconstruction of events, especially at high values of $\cos\theta^*$ when there is a large difference in the subjet p_Ts. Furthermore, we use k_T rather than anti-k_T to form our subjets because it more accurately reconstructs the softer jet in situations where the jets are nearly collinear (see appendix B).

One important thing to consider in the subjet analysis is that the results are not as robust in going from matrix-element to parton shower as were the leptonic results; the curves change shape (compare the parton and jet level results for both sides of the decay in Table 4.5). This is because the diffuse nature of the subjets makes them difficult to resolve when they become collinear and/or soft. We note, however, that at the LHC we can expect to calibrate subjet measurements for boosted hadronic Ws

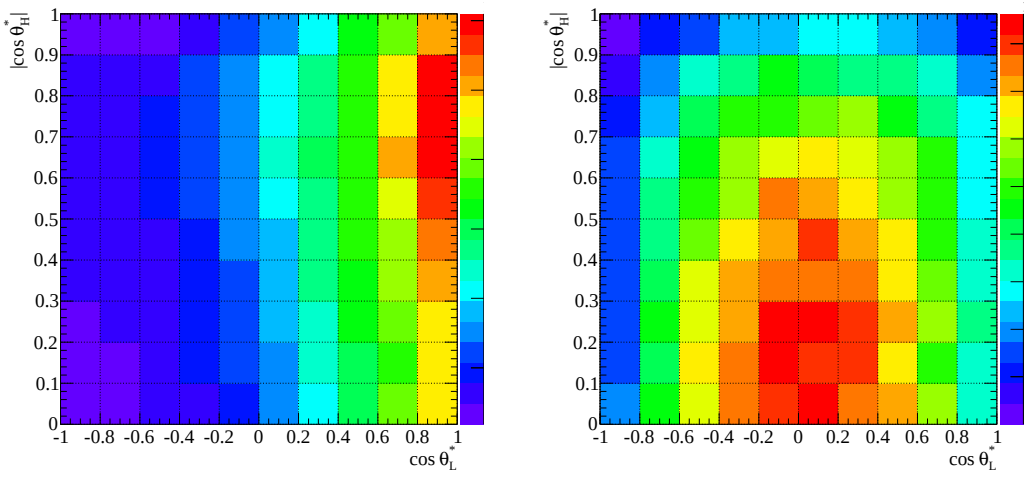

Figure 4.7: Jet-level distribution of $\cos\theta^*$ (labeled with subscript H and L for hadronic and leptonic decays, respectively) for the SM Higgs boson(left) and Higgs boson with $c_H\xi = -0.6$ (right). The scale is individually normalized for each plot, going from violet to red as the concentration of events increases. The scaling of the color gradient on the right side of each plot is linear.

with large SM samples, and while the parton-level to jet-level results may vary, the correspondence should eventually be well understood. Thus the leptonic gauge boson analysis is likely to be the first tool used, but the hadronic analysis can be added later on.

4.5 Conclusions

In this chapter, we have introduced a powerful new technique for identifying signs of beyond the SM physics associated with the EWSB by probing VBF processes at the LHC.

We began by motivating our decision to study models of EWSB employing a light Higg-like particle with couplings deviating from those of the SM. Theories with a light Higgs boson are favored by the current electroweak precision data. However, this type of model is the most difficult to distinguish from the SM, especially if the

new physics particles are very heavy. However, it is also the scenario in which VBF can be most useful, because for such a scenario the amplitude for $V_L V_L \to V_L V_L$ scattering exhibits a non-SM E^2 growth until new physics comes into play.

Past analyses designed to measure this E^2 growth were reviewed and updated to account for the effects of the parton shower and jet clustering. While the cuts pioneered by these works can be very powerful in reducing the SM background, we demonstrate that there is still a significant $\mathcal{O}(100\%)$ rate uncertainty attributable to factorization scale ambiguities. Thus, we show that in the absence of higher order calculations that might give us some guidance on the correct scale treatment, rate information alone may not be sufficient to distinguish the signs of new physics.

We then propose our new technique, which uses the semi-leptonic decay mode of the VV system to fully reconstruct events and obtain the decay angle distributions for the V daughters. These distributions can be decomposed into longitudinal and transverse components, allowing us to measure the E^2 growth in scattering amplitudes associated with new physics by looking for the relative increase in longitudinal production. We demonstrate that these results are insensitive to the scale ambiguities that trouble rate measurements.

In closing, we wish to reiterate that polarization measurements of VBF final states are a powerful, robust probe of new physics associated with the EWSB. Although we have only employed them here to study light SM-like Higgs scenarios, they would be useful in more general scenarios of EWSB as long as the longitudinal gauge bosons are significantly involved. Such measurements may prove to be our best tool in understanding the physics of EWSB at the LHC.

Chapter 5

Higgs boson Search through Highly Displaced Vertices

This chapter presents a proposal for a new search channel for the Higgs boson decaying to two long-lived neutral particles, each of which decays to $b\bar{b}$ at a displaced vertex inside the beampipe. We demonstrate how to discriminate the signal from the QCD background by looking at properties of the tracks from the highly-displaced vertices. We concentrate on the case of a 120 GeV Higgs boson that always decays via this mode, with the long-lived neutral particle having a mass in the range of 15–30 GeV and a decay length commensurate with the beam pipe radius. Such a signal can be readily observed with an integrated luminosity of 1 fb^{-1}.

5.1 Introduction/Theory

The Higgs sector is one of the great unknowns in our current understanding of particle physics, and is the primary target of the current Tevatron and Large Hadron Collider (LHC) programs. Within the Standard Model (SM), the mass of its single Higgs boson is undetermined, but for a given mass the Higgs boson's decay modes are precisely predicted. However, beyond the Standard Model (BSM), the number of neutral Higgs

bosons (and other scalars or pseudoscalars) and their decay modes can vary widely. It will be essential, especially if the SM Higgs boson is not found at the LHC during the current run, to do a very wide variety of analyses that cover all possibilities, until at least one discovery is made.

In this chapter we address an exotic Higgs decay mode, one that would have escaped existing search strategies. We consider the possibility [108] (see also [109, 110] for closely related work) that the Higgs boson h decays to two spin-zero neutral particles a, and the a decays in turn to $b\bar{b}$ with a displaced vertex. More specifically, we will consider the case where the lifetime τ_a of the a puts its decay at a distance from the collision point of order millimeters to a few centimeters. The case where the typical decay is in the several to 20 centimeter range has been weakly constrained by D0 [111]; longer and shorter lifetimes have not been significantly constrained, even for 100% branching fraction for this mode.

It is sometimes argued that searches of this type are not so well motivated, because the chance of the a to have a lifetime that allows for decays inside the detector is low. But there are both theoretical and experimental counterarguments. First, long-lived particles are less rare in models than is commonly assumed. In hidden valley models [112], for instance, there may be not one but many new particle states with a wide variety of lifetimes, similarly to the case of QCD, and this plenitude makes it more likely that one of these particles will decay at a certain non negligiable distance from the interaction point creating a displaced vertex which is detectable by the experiments. Second, decays of such particles have such limited SM background that in principle only a few such events might suffice for a discovery, so even a small branching fraction to such particles may lead to a discovery channel. That said, detector backgrounds can be a serious issue, and event triggering and reconstruction may be an even larger one if the lifetimes are long enough. Each search strategy has its own features, and some are easier than others.

The Tevatron and LHC detectors were generally not optimized for finding long-lived particles, with the exception of B hadrons, and searches for such particles face numerous challenges. In this paper we consider the case that, relatively speaking, is the easiest: a search for a new particle that mainly decays before that particle reaches the beampipe. Such decays face little or no background from secondary interactions of hadrons with detector material, and the dominant background is a physics background from real B hadron decays. However, to the extent the a lives longer than the B hadron and is considerably heavier, distinguishing it from SM heavy-flavor backgrounds should be easier. For the specific case of $h \to aa$, the situation is better still, since there are two a decays per event, and also a mass resonance that may be reconstructable.

The main purpose of our paper is to suggest a search strategy for $h \to aa$, with a decaying to $b\bar{b}$ before passing through the wall of the beampipe.

Since our signal consists of the significantly displaced decay of the (pseudo-)scalar, we will look for displaced tracks as our signal. The dominant background will stem mostly from production of two or more heavy quarks. Each decaying pseudo-scalar might create a single jet or two, depending on the angle between the two b quarks and the details of the jet algorithm. We will use large-radius anti-k_T [113] "displaced-track jets" (jets formed by applying the anti-k_T algorithm only to displaced tracks) in this analysis to try to capture the hadrons from both b quarks in a single object. By requiring these displaced-track jets be massive and isolated from any prompt tracks, we will reduce backgrounds to the point that we already obtain an excess of events in some cases. Efficiently identifying the correct primary vertex in the context of pile-up will be important in the isolation stage. Then we will try to reconstruct the Higgs as a resonance in the invariant mass of the two highest-p_T calorimetric jets that are close in angle to the displaced-track jets. This will require a careful pileup subtraction, and we use the approach suggested in [114].

Although our search strategy uses $h \to aa$ as a benchmark for optimization, it is not strongly dependent on the specific initial or final state. Consequently it should be somewhat model-independent, and would be sensitive to a variety of models with two long-lived particles in the events. For example, certain gauge-mediated supersymmetric models with a neutralino [115] decaying in flight to a Z or h might be picked up by our search. One point of model-dependence worth keeping in mind is that the heavy-flavor content of the a decay is important for our strategy, as we will base our study on the requirement to have 2 jets and 2 soft muon at the High Level Trigger (HLT, purely software-based and with access to the full event information). This choice will be found to provide reasoable efficiency and rate to be included in either CMS/ATLAS trigger menu while running at few times $10^{33}\text{cm}^{-2}s^{-1}$

5.2 Event Generation

At hadron colliders the dominant Higgs production mechanism is via gluon-gluon fusion. In this note we study the process $gg \to h \to (a \to b\bar{b})(a \to b\bar{b})$, where the Higgs boson is produced by gluon fusion and then decays into a pair of long lived (pseudo-)scalars which then each decay to a pair of bottom quarks. We consider this in the context of pp collisions at 7 TeV center of mass energy.

We generate the signal samples for Higgs mass $m_h = 120$ GeV and the (pseudo-)scalar mass m_a between 15 and 35 GeV with 5 GeV steps. Samples were generated for the $c\tau_a$ of the scalar varying within a wide range between 0.1 mm to 40 mm. The signal sample is generated using Pythia 6.4.21 [116]. The NNLO cross section for this process is 17 pb at 7 TeV [118].

The main background for this process is heavy quark production, including events in which multiple heavy-quark ($Q\bar{Q}$) pairs are created, which represents the most difficult background to remove. The background samples are generated at parton

level using ALPGEN 2.13 [156] and then showered through Pythia 6.4.21[1]. The specific details of the generation of the signal and background is shown in Table 5.1. For both the signal and background, the underlying events are incorporated using the Pythia "DW" tune [120] and the pileup is simulated assuming an average of 6 pileup events per bunch crossing.

While we carry out all simulations at leading order, we use the K factor from [121, 122, 123] to normalize the cross section, increasing the LO cross section by a factor of order $2-3$. For the background that will turn out to be dominant, $4b$ production, the NLO corrections have been calculated in Ref. [124] for the same scale choice as shown in table 5.1 and found to be of order 1.5. The cross section for the 4Q background is also normalized with this K factor.

All jet reconstruction in the following is performed using Fastjet 2.4.2 [34].

	Process	Scale Choice	PDF Choice
Signal	$gg \to h \to (a \to b\bar{b})(a \to b\bar{b})$	m_h	CTEQ5L
2Q	$Q\bar{Q}$+N_p partons with N_p from 0 to 1 and $Q = c, b$	CKKW Scale	CTEQ5L
4Q	$Q\bar{Q}Q'\bar{Q}'$ with $Q, Q' = c, b$	$\frac{1}{4}\sqrt{\sum_i p_{T,i}^2}$	CTEQ5L

Table 5.1: Some details of the Monte Carlo generation for backgrounds and signal. The CTEQ5 PDF [125] is the default choice in the DW tune. The $Q\bar{Q}$ and $Q\bar{Q}+1$ samples are combined using MLM matching (see Ref. [126]).

5.3 Identifying Displaced Tracks

To identify the displaced tracks arising from the displaced pseudo-scalar decay to b quarks and their ensuing hadronization, we will use the 2-D Impact Parameter (IP) — the transverse distance between the track and the vertex at the point of closest approach. For fast-moving B hadrons, the average IP is invariant under boosts of

[1]For the 2Q background, we turn off the gluon splitting to b quark pairs to avoid double counting of the events.

the B hadron along its direction of motion, and the typical scale of the IP is set by $c\tau_a \sim$ 400–500 μm. Given that the uncertainty in measurement of the IP can be of the same order of magnitude as the IP, a better observable for b-tagging is the Impact Parameter Significance (IPS) defined as IP/σ_{IP}. IPS is being used by all experiments at hadron colliders as one of the most robust b-tagging variables.

The IP resolution is extracted from [127]. We parametrize it as a function of pseudorapidity η and transverse momentum p_T:

$$\text{Resolution} = a + \frac{b}{p_T} + (c + \frac{d}{p_T})\eta^2 \tag{5.1}$$

with the coefficients a, b, c, d as shown in Table 5.2.

a	20.4
b	56.4
c	-0.11
d	18.2

Table 5.2: The coefficients of the impact-parameter resolution parameterization Eq. 5.1 giving resolution in μm for track momenta in GeV. The coefficients have been deduced based on the resolutions shown in Ref. [127], cf. also table 5.3.

Table 5.3 shows some values of the transverse impact parameter resolutions as a function of p_T and η. Tracks are measured up to $|\eta| = 2.5$.

p_T (GeV) \ η	0	1.0	2.0
1.0	80	95	150
3.0	40	45	65
8.0	26	30	35

Table 5.3: Measured resolution (in μm) of the transverse impact parameter from Figure 7 in Ref. [127] for different track p_T and η.

In addition, we will require that all the displaced tracks are originated from the

vertices inside the beam pipe. The vertex reconstruction is done in the following way:

- 1. Identify the MC truth vertices with at least 2 charged tracks with $p_t > 0.5$GeV; define two distinct vertices as being part of the same MC truth vertex if they are within the tolerance of 1 micron of each other.
- 2. For each remaining track, find the existing MC truth vertex to which it comes closest. If it comes within 0.3 mm of that vertex and the angle between the track and the vertex's direction from the primary vertex is less than $\frac{2}{3}\pi$, assign it to that vertex.
- 3. For the remaining un-vertexed tracks, find the pair that comes closest; if they come within 0.3 mm and the angle between the momentum of the two tracks is less than $\frac{2}{3}\pi$, create a new vertex at midpoint between the points of closest approach, then repeat from step 2.

5.4 Signal Selection

Before giving the event selection cuts used in our study, we outline our basic strategy, supporting our choices with plots of the key variables on which our cuts will be based.

Due to the long lifetime of the (pseudo-)scalar, the signal events have highly-displaced vertices, and to differentiate signal from background we look for unusually large numbers of tracks coming from displaced vertices. Figure 5.1 shows the distribution of number of tracks from signal and background samples for all tracks with IPS > 5. Clearly the number of tracks with substantial IPS is larger in signal than in background.

We will focus on those tracks with large IPS, and combine them to form jets, which we will call "displaced-track jets" to distinguish them from calorimeter jets which we use elsewhere. We use a large jet radius, so as to include most of the displaced tracks from a single a decay in a single displaced-track jet.

Since most tracks from the a decay will be included in a corresponding displaced-track jet, and a little more than one third of hadrons are neutral, the jet should have a mass that is around 60%-70% of m_a. In background, however, the jet mass will typically be much smaller. Many of the tracks from b-hadron decays will not have a large IP, so even in a jet with a gluon splitting to $b\bar{b}$, which is the source of background (the 4Q sample) most difficult to reduce, the mass of the two leading track jets will be significantly lower than the invariant mass of the two b quarks. For a jet from a more isolated b quark (the 2Q sample) the invariant mass distribution is much lower still. The mass distribution of the second-hardest displaced-track-jet is shown in Fig. 5.2.

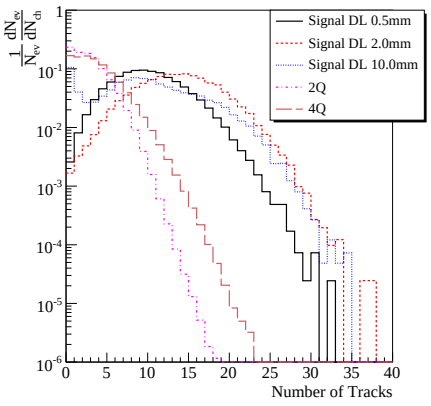

Figure 5.1: The distribution of the number of tracks with IPS > 5 (displaced tracks) for the backgrounds and for signals with different Decay Lengths (DL), shown after trigger cuts (Cut 1 below). The distributions are normalized to unity; $m_h = 120$ GeV and $m_a = 20$ GeV.

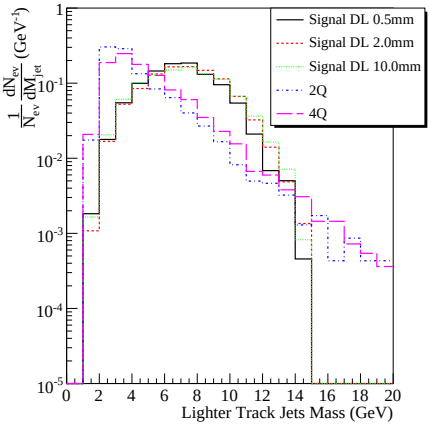

Figure 5.2: The mass distribution of the lighter of the two highest-p_T displaced-track jets, for events that pass Cuts 1 and 2 below. Shown for the background samples and for signals with different Decay Lengths (DL). The distributions are normalized to unity. In the full analysis, the two highest p_t track jets are both required to have masses greater than 6 GeV (Cut 3).

Finally, a key difference between signal and background is in the pattern of nearby prompt tracks. In standard-model heavy-hadron production, any b-quark or c-quark hadronizes within about a fermi of the primary vertex, and gluons generated in QCD

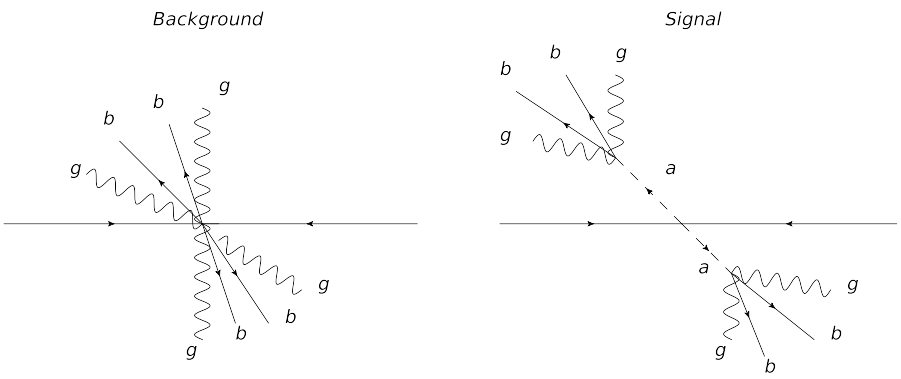

Figure 5.3: An illustration of why backgrounds have more prompt tracks near the jets than does the signal: gluons in QCD final-state showering (before hadronization) are produced mainly at the primary vertex in the background QCD events, but in the signal the a particle is color-neutral, and showering occurs only at the displaced location of its decay.

showering will generate, through QCD fragmentation, prompt moderately-hard tracks that accompany the heavy hadrons within their jet cone. In contrast, the a, a colorless particle, does not undergo any fragmentation. Only when it decays to $b\bar{b}$, at a macroscopic distance from the primary vertex, does a process of hadronization begin. All non-b hadrons generated in the showering and fragmentation of the $a \to b\bar{b}$ decay will emerge at the a decay vertex, and thus they too will typically have a large IPS. This is illustrated in Fig. 5.3.

Therefore, if we choose the prompt tracks that are at a small ΔR from either of the two highest-p_T displaced-track jets, we are likely to find more tracks, with higher energy, for the background than for the signal. The distributions of the p_T sum of these tracks are shown in Fig. 5.4. We see that a judicious cut can remove most of the remaining 4Q background.

The various selections are applied sequentially, as described below, and the yields for signal and background are presented in Table 5.4.

- Cut 1: Require events to be selected by the HLT with at least two calorimeter jets (formed using the anti-k_T algorithm with cone radius 0.7) of $p_T > 40$ GeV and two muons with $p_T > 3$ GeV and IPS > 5 (in the acceptance region of $|\eta| <$

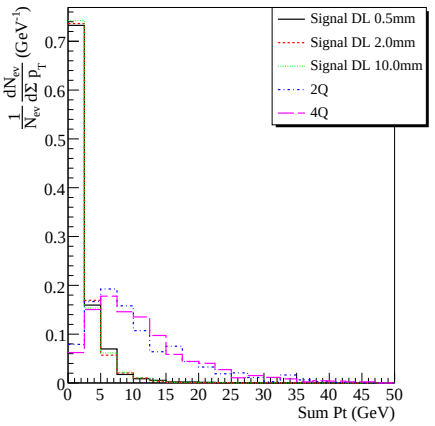

Figure 5.4: The distribution of the sum p_T variable (as defined in Cut 4, the smaller of the two jets are plotted), shown for events that pass cuts 1–3, both for the backgrounds for signals with different Decay Lengths (DL). The plots are normalized to unity.

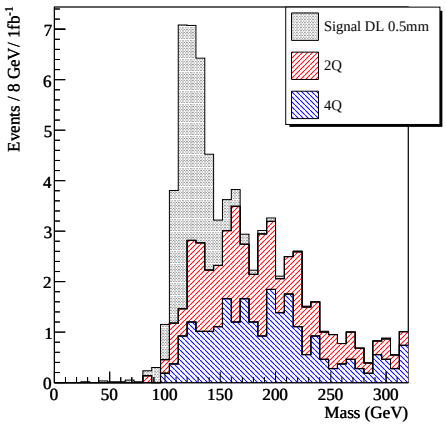

Figure 5.5: The mass spectrum of the Higgs boson candidate after Cut 4, shown for the backgrounds and the signal with (pseudo-)scalar Decay Length (DL) of 0.5 mm.

2.5)

- Cut 2: Select all tracks with $p_T > 0.5$ GeV. From these tracks, construct all radially-displaced vertices with IP greater than 1.0 mm. Reject all tracks that do not participate in any displaced vertex (the vertices are clustered using a tolerance of 0.3 mm) or that pass through a vertex at a radius > 25 mm (at or beyond the beampipe.) From the tracks that remain, make a list (List A, displaced tracks) of all tracks that have IPS > 5. Form displaced-track jets by clustering the tracks from List A, using the anti-k_T algorithm with a large cone radius, $R = 1.0$. Take the two highest-p_t displaced-track jets (call them T_1 and T_2). Require that each T_1 and T_2 have at least 6 displaced tracks.

- Cut 3: Require that both T_1 and T_2 have a mass greater than 6 GeV. (See Fig. 5.2, which shows the displaced-track mass distribution for the lighter of T_1 and T_2.)

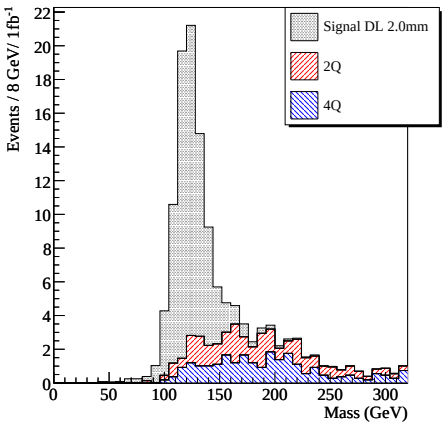

Figure 5.6: The mass spectrum of the Higgs boson candidate after Cut 4, shown for the backgrounds and the signal with (pseudo-)scalar Decay Length (DL) of 2.0 mm.

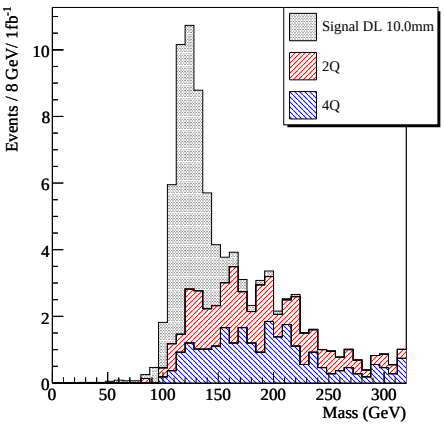

Figure 5.7: The mass spectrum of the Higgs boson candidate after Cut 4, shown for the backgrounds and the signal with (pseudo-)scalar Decay Length (DL) of 10.0 mm.

- Identify the primary vertex, as follows:
  - Trace back each track n in List A to the beamline.
  - Find its point x_n, y_n, z_n of closest approach.
  - Compute the p_T-weighted average of the z_n

$$\bar{z} = \left[\sum_{n \in \text{List A}} z_n \, (p_T)_n \right] / \left[\sum_{n \in \text{List A}} (p_T)_n \right] \tag{5.2}$$

    and identify the primary vertex with the proton-proton collision whose z coordinate is closest to $\bar{z}$.

- Cut 4: Select all prompt tracks emerging from the primary vertex that have $p_T > 0.5$ GeV and with a ΔR smaller than 1.0 from the jet axis of T_1 and T_2. Require the scalar p_T sum for each of T1 and T2 to be less than 5 GeV (see Fig. 5.4). We will call this cut "Absolute Track Isolation", following the terminology used by the experiments, and use Σ_T as a shorthand for the sum

p_T variable.[2]

- Construct large ($R = 1$, in contrast to the initial selection) anti-k_T calorimeter jets. To remove the effect of the underlying event and pileup, use the jet-area [130] based pileup-subtraction method of [114] (which involves using the k_T algorithm [131, 132] on the whole event and determining the appropriate energy-per-unit-area to subtract).

- Cut 5 Choose the two $R = 1$ calorimeter jets C_1 and C_2 closest in angle to the displaced-track jets T_1 and T_2. Compute the invariant mass of C_1 and C_2 (with pile-up and underlying event subtracted) and combine them to get the candidate Higgs boson mass. For the purpose of quoting a final significance, we will examine the number of events in a mass window from 90-140 GeV.

The resulting mass spectrum of these two calorimeter jets is shown in Figs. 5.5, 5.6, 5.7 for different lifetimes of the scalar. We see that for some lifetimes and an $h \to aa$ branching fraction of 100%, the signal can easily dominate over the background, and a peak in mass is clearly visible.

5.5 Results

The number of events for signal and background after each step of the cuts are shown in Table 5.4 for 1 fb^{-1} of integrated luminosity. In this table, we choose $m_h = 120$ GeV and $m_a = 20$ GeV and three decay length 0.5, 2.0, 10 mm. The background is overwhelming to start with, but after applying all the kinematic cuts, the signal becomes comparable to the background. Since the B-hadron mass is less than 6 GeV, it is expected that after cutting on the mass of the displaced-track jet, few events

[2]An isolation cut exploiting the colour-neutrality of the pseudo-scalar in $H \to aa$ decays had been used before in Refs [128, 129]. In our case, the separation between prompt and non-prompt radiation serves to enhance the discriminating power of the isolation requirement.

from the 2Q sample remain. A closer look at the 2Q sample reveals that the events passing this cut are exclusively $Q\bar{Q}g$, where the gluon further splits into two heavy quarks. Thus there is some overlap between the 2Q and 4Q samples, and so the background is therefore overestimated by a factor of order 2. In the interest of being conservative, we will not correct for this.

Channel	0.5 mm	2.0 mm	10.0 mm	2Q	4Q
Cut 1	229	332	416	712000	108000
Cut 2	36.4	123	61	656	480
Cut 3	24.8	88	42	109	124
Cut 4	20.3	73	34	21	21
Cut 5	18	65	30	5.6	4.8

Table 5.4: Comparison of the background and signal for $1 fb^{-1}$ luminosity; $m_h = 120\,\text{GeV}$, $m_a = 20\,\text{GeV}$, and three pseudo-scalar decay lengths are shown, 0.5 mm, 2 mm, 10 mm.

A comment is due concerning the trigger rate. The trigger selection corresponds to cut 1 and one sees that the cross section is of order 1 nb^{-1} (the order of magnitude has been confirmed with an independent inclusive dijet sample generated with Pythia 6.4). For an instantaneous luminosity of a few times $10^{33}\ cm^{-2}\ s^{-1}$, this corresponds to a rate of a few Hz, i.e. about 1% of typical high-level trigger output bandwidths, which are several hundred Hz. Prescaling could further reduce the rate, while still delivering an adequate integrated luminosity for this analysis.

Following the selection criteria discussed in Sec. 5.4, we can clearly see the Higgs boson mass peak in Fig. 5.6. Figs. 5.5 and 5.7 show the corresponding dijet mass spectrum for the 0.5 mm and 10.0 mm decay lengths respectively. If for simplicity we treat this search as a pure counting experiment, without cutting on the invariant mass variable, and assuming small systematic errors for the moment (see below), the signal has a statistical significance of about 11 in the case $c\tau_a = 2$ mm and $m_a = 20$ GeV. Placing a restriction on the dijet mass as in cut 5 increases the significance to

about 20. The statistical significance of the signal is shown for other choices of $c\tau_a$ in Fig. 5.8, and for other choices of m_a in Fig. 5.9. Note we have not optimized the cuts for these other masses and lifetimes. To improve the statistical significance at different lifetimes, one might want to use a looser cut on the IPS for smaller values of $c\tau_a$ and a stricter cut on the IPS for greater values of $c\tau_a$. For masses larger than 25 GeV, one might want to optimize the selection criteria, for instance, using a harder track-jet mass cut and a larger jet radius.

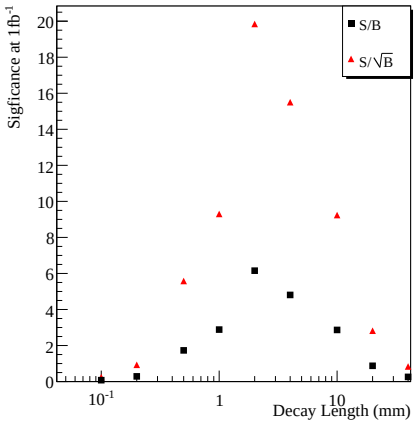

Figure 5.8: The statistical significance of the signal as a function of the decay length of the (pseudo-)scalar, for 1 fb^{-1}. The black squares indicate the ratio of signal to background, and the red triangles give the ratio of signal to square-root of background. In this plot, m_a is set to 20 GeV.

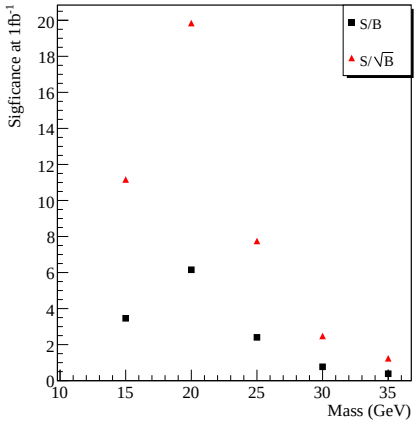

Figure 5.9: The statistical significance of the signal as a function of the mass of the (pseudo-)scalar, for 1 fb^{-1}. The black squares are the ratio of signal to background, and the red triangles give the ratio of signal to square root of background. The Decay Length $c\tau_a$ is set to 2 mm.

5.6 Conclusion

In this chapter we have introduced several powerful kinematic cuts designed to discover a Higgs boson decaying to long-lived neutral particles. The unique feature of this channel is the highly-displaced vertices resulting from the decay of the long-lived particles, some fraction of which occur before reaching within the beampipe. The

tracks from these vertices will have large IPS, and form clusters with large mass that are isolated from prompt tracks. We exploit these features to separate signal from background. For certain values of the (pseudo-)scalar decay length and masses in Fig. 5.8 and Fig. 5.9, we may be able to discover the Higgs in this channel with just 1 fb^{-1} of recorded LHC data.

We should comment regarding the trigger selection, which we took (see Cut 1 of section 5.4) as a requirement of two displaced muons and two jets with $p_T > 40$ GeV. Should the trigger rate be found to be intolerably high, one could perhaps additionally perform a regional track reconstruction in the vicinity of the calorimeter jets. One could then study either the number of prompt tracks with $p_T > 1$ GeV (requiring it to be less than two) or the number of tracks with large IP. Full regional reconstruction of the tracks associated with the calorimeter jets might consume a intolerably long CPU time to be done on the High Level Trigger. Another option would be to use Particle Flow (PF) reconstructions of all the objects in the event after a calo jets filter was applied to expedite the HLT trigger path CPU time. One should require 2 neutral PF jets with additional 2 muons in the event. Note, the reason one asks for neutral PF jets are an artifact of the PF jets and track reconstructions that does not manage to reconstruct displaced tracks after a certain distance from the interaction point. Therefore the PF algorithm will identify displaced jets as neutral PF jets. These techniques should suppress the background rate and should not much hurt the signal efficiency.

The search described in this chapter should also be sensitive to other models with displaced vertices and rather large cross-sections. Only the final step in the search method assumes anything specific about the Higgs being the source of the displaced vertices, though our di-muon trigger requirement makes us sensitive only to certain final states, including ones with bottom, charm, taus, and certain exotics (such as hidden sector particles decaying to leptons [112, 108], as for instance in lepton-jets

[133], or to neutralinos decaying via R-parity violation to heavy flavor [110].) Further optimization of the search strategy might allow for both improved significance for the Higgs signal and wider sensitivity to other possible new sources of displaced vertices.

Chapter 6

Systematic Uncertainties of Invariant Mass Distribution of W+jets at Tevatron

CDF has recently reported an excess in the dijet invariant mass distribution around 150 GeV for events containing a lepton, missing energy and exactly two jets [134]. This has led to many new physics interpretations [135, 136, 137, 138, 139, 140, 141, 142, 143, 144, 145, 146, 147, 148, 149, 150, 151, 152, 153]. However, the excess could also possibly be from the systematic uncertainty of the W+2jets background simulation. In this chapter, We will investigate the various sources of the systematic uncertainties.

6.1 Revisit of the W+2jets Analysis at CDF

In this chapter, we will use the same cuts as the original CDF analysis [134]. Namely, we ask for events containing exactly two jets with $p_T^j > 30$ GeV in $|\eta^j| < 2.4$ units of rapidity. We use the CDF JetClu algorithm with parameter $R = 0.4$ implemented in Fastjet 2.4.2 [34]. The jets must be separated by at most 2.5 units of rapidity and

the transverse momentum of the dijet system (p_T^{jj}) is constrained by $p_T^{jj} > 40$ GeV. Events should contain exactly one lepton in $|\eta^\ell| < 1$, $p_T^\ell > 20$ GeV that is separated from the jets by $R_{j\ell} > 0.52$. We require that the missing transverse momentum ($E_T^{\rm miss}$) satisfies $E_T^{\rm miss} > 25$ GeV and is separated azimuthally from the leading jet, $\Delta\phi > 0.4$.

The CDF results are shown in Fig 6.1. The data deviates from the background simulation significantly, and if a Gaussian distribution between 120-160 GeV is added, the statistical significance is 3.4 [134].

6.2 ME-PS matching

Matrix Element (ME) is good at describing the hard process of the event, typically $2 \to N$ process. To describe the full event with all the soft radiations, we need the Parton Shower (PS) to describe the jet evolution. A complete simulation of the events will need both of them. However, there is an overlap in the phase space between these two methods, so we need ME-PS matching to avoid the double counting. Here, we will describe MLM matching, CKKW matching [154].

6.2.1 MLM matching

The MLM matching will find the double counting phase space and reject them. It is implemented this way [154]:

- The first step is the generation of parton-level configurations for all final-state parton multiplicities n up to a given N ($W + N$ partons). They are defined by the following kinematical cuts:

$$p_T^{part} > p_T^{min}, |\eta^{part}| < |\eta^{max}|, \Delta R_{jj} > R_{min} \tag{6.1}$$

where p_T^{part} and η^{part} are the transverse momentum and pseudo-rapidity of the final-state partons, and ΔR_{jj} is their minimal separation in the (η, ϕ) plane. The parameters p_T^{min}, η_{max} and R_{min} are called generation parameters, and are the same for all $n = 1, \ldots, N$.

- Events are then showered, using Pythia [116] or Herwig [33]. The evolution for each parton starts at the scale determined by the default Pythia and Herwig algorithms on the basis of the kinematics and colour connections of the event. The upper veto cutoff to the shower evolution is given by the hard scale of the process. After evolution, a jet cone algorithm is applied to the partons produced in the perturbative phase of the shower. Jets are defined by a cone size R_{clus}, a minimum transverse energy E_T^{clus} and a maximum pseudo-rapidity η_{max}^{clus}. These parameters are called matching parameters, and should be kept the same for all samples $n = 0, 1, \ldots, N$. These jets provide the starting point for the matching procedure, described in the next bullet. In the default implementation, we take $R_{clus} = R_{min}$, $\eta_{max}^{clus} = \eta^{max}$ and $E_T^{clus} = p_T^{min} + \max(5Gev, 0.2 \times p_T^{min})$, but these can be varied as part of the systematics assessment. To ensure a complete coverage of phase space, however, it is necessary that $R_{clus} > R_{min}$, $\eta_{max}^{clus} > \eta^{max}$ and $E_T^{clus} > p_T^{min}$.

- Starting from the hardest parton, the jet, which is closest to it in (η, ϕ) is selected. If the distance between the parton and the jet centroid is smaller than $1.5 \times R_{clus}$, we say that the parton and the jet *match*. The matched jet is removed from the list of jets, and the matching test for subsequent partons is performed. The event is fully matched if each parton matches to a jet. Events, which do not match, are rejected. A typical example is when two partons are so close that they cannot generate independent jets, and therefore cannot match. Another example is when a parton is too soft to generate its own jet, again

failing matching.

- Events from the parton samples with $n < N$, which survive matching, are then required not to have extra jets. If they do, they are rejected, a suppression, which replaces the Sudakov reweighting used in the CKKW approach. This prevents the double counting of events, which will be present in, and more accurately described by, the $n + 1$ sample. In the case of $n = N$, events with extra jets can be kept since they will not be generated by samples with higher n. Nevertheless, to avoid double counting, we require that their transverse momentum be smaller than that of the softest of the matched jets.

When all the resulting samples from $n = 0, \ldots, N$ are combined, we obtain an inclusive W+jets sample. The harder the threshold for the energy of the jets used in the matching, E_T^{clus}, the fewer the events rejected by the extra-jet veto (i.e. smaller Sudakov suppression), with a bigger role given to the shower approximation in the production of jets. Using lower thresholds would instead enhance the role of the matrix elements even at lower E_T, and lead to larger Sudakov suppression, reducing the role played by the shower in generating jets. The matching/rejection algorithm ensures that these two components balance each other.

6.2.2 CKKW matching

The CKKW matching will reject Parton shower to cover only phase space not covered by ME. The implementation is described as:

- Select the jet multiplicity n and parton identities i with probability

$$P^{(0)}(n, i) = \frac{\sigma^{(0)}_{n,i}}{\sum_{k,j}^{k=N} \sigma^{(0)}_{k,j}} \tag{6.2}$$

where $\sigma^{(0)}_{n,i}$ is the tree-level njet cross section at resolution $y_{\text{ini}} = Q_1^2/Q^2$, cal-

culated using a fixed value $\alpha_s(Q_1)$ for the strong coupling. The label i is to distinguish different parton identities with the same multiplicity, e.g. $i = q\bar{q}gg$ or $q\bar{q}q\bar{q}q$ for $n = 4$. N is the largest jet multiplicity for which the calculation can realistically be performed ($N \sim 6$ currently). Errors will then be of relative order α_s^{N-1}. Ideally, one should check that any given result is insensitive to N.

- Distribute the jet momenta according to the corresponding n-parton matrix elements squared $|\mathcal{M}_{n,i}|^2$, again using fixed $\alpha_s(Q_1)$.

- Use the k_T-clustering algorithm to determine the resolution values $y_2 = 1 > y_3 > \ldots > y_n > y_{\rm ini}$ at which $2, 3, \ldots, n$ jets are resolved. These give the nodal values of $q_j = Q\sqrt{y_j}$ for a tree diagram that specifies the k_T-clustering sequence for that configuration.

- Apply a coupling-constant weight of $\alpha_s(q_3)\alpha_s(q_4)\cdots\alpha_s(q_n)/[\alpha_s(Q_1)]^{n-2} < 1$.

- For each internal line of type i from a node at scale q_j to the next node at $q_k < q_j$, apply a Sudakov weight factor $\Delta_i(Q_1, q_j)/\Delta_i(Q_1, q_k) < 1$. For an external line from a node at scale q_j, the weight factor is $\Delta_i(Q_1, q_j)$.

- Accept the configuration if the product of the coupling-constant weight and the Sudakov factor is greater than a random number $\mathcal{R} \in [0, 1]$ times[1] $[\Delta_q(Q_1, Q)]^2$. Otherwise, return to step 1.

6.3 Results

We will employ three different Matrix Element Generator in this study, Madgraph [155], ALPGEN [156], and SHERPA [157]. The Madgraph and ALPGEN events will be fully showered and hadronized by Pythia 6.4 [116], while the SHERPA events will be

[1]Multiplying by $[\Delta_q(Q_1, Q)]^2$ increases the efficiency of the procedure, since this constant factor is always present.

handled by the internal shower and hadronization program CSSHOWER [158] and AHADRONIC [159]. Jet Matching are applied for all the sample generated in this study and it is matched up to 3 jets (the highest multiplicity is 3). In ALPGEN, MLM cone matching is available, while in Madgraph, one could do both MLL cone matching and kt matching, and in SHERPA, the CKKW matching is used.

Parton distribution functions (PDF) are defined as the probability density for finding a particle with a certain longitudinal momentum fraction x at momentum transfer Q^2. It is obtained by a global fit of the experimental data. There are various different versions of PDF sets, here we will use three different set of PDF: CTEQ5, CTEQ6 and CTEQ6l[25]. The dijet mass spectrum and the ΔR between the two jets are shown in Figure 6.2, the samples are from ALPGEN matched up to 3 jets. At parton level, the p_T cut is 15 GeV and the cone size is 0.4, during ME-PS merging, the matching scale is set to 20 GeV. In Figure 6.1, CDF used CTEQ5 to generate the events.

In the matrix element calculation, the coupling constant is evaluated at the renormalization scale and the PDF are evaluated at the factorization scale, and the factorization scale also sets the virtuality of the parton shower. Figure 6.3 shows the difference between the dijet mass spectrum and ΔR between the two jets for different scale choices. We will vary the default scale by half and two and compare with the result with the default scale. The samples are from ALPGEN matched up to 3 jets. At parton level, the p_T cut is 15 GeV and the cone size is 0.4, during ME-PS merging, the matching scale is set to 20 GeV.

In ME-PS matching, we need to choose the matching scale described in the previous section. However, these scales are quite arbitrary and has no physical meanings. We will vary these scales to probe the systematic uncertainties associated with these scales in Figure 6.4. The events are generated by ALPGEN, matched up to 3 jets. At parton level, the p_T cut is 15 GeV and the cone size is 0.4, during ME-PS merging,

the matching scale is set to 20, 25 and 30 GeV. In Figure 6.1, this scale is set to be 20 GeV.

In Madgraph, the MLM algorithm is not only implemented for cone matching, but also for k_T matching. We show the difference between the two matching schemes in Figure 6.5. The events are generated by Madgraph, matched up to 3 jets. For MLM cone matching, at parton level the p_T cut is 15 GeV and the cone size is 0.4, during ME-PS merging, the matching scale is set to 20 GeV. For MLM k_T matching, at parton level, the k_T cut is 15 GeV and during ME-PS merging, the matching scale is set to 20 GeV.

In addition, we also show the systematic uncertainty from the choice of the ME-PS matching scale in the MLM k_T matching in Fig 6.6. The events are generated by Madgraph, matched up to 3 jets with MLM k_T matching. At parton level the k_T cut is 15 GeV, during ME-PS merging, the matching scale is set to 20, 25 and 30 GeV.

Figure 6.7 shows the results for various generators, ALPGEN, Madgraph and SHERPA. The samples for all the three generators are matched up to 3 jets. For ALPGEN and Madgraph, at parton level the p_T cut is 15 GeV and the cone size is 0.4, during ME-PS merging, the matching scale is set to 20 GeV. For SHERPA, the matching scale is set to 15 GeV for the CKKW matching. In SHERPA results differ from Madgraph and ALPGEN significantly, and looks more similar to the data in Figure 6.1.

Figure 6.8 shows the results for different matching scale in the CKKW matching. The events are generated by SHERPA, matched up to 3 jets with CKKW matching. And the matching scale is set to 10, 15 and 20 GeV.

6.4 Conclusion

In this chapter, we investigate all the possible systematic uncertainties for the dijet mass distribution at Tevatron. Among all the possible sources, the difference between MLM matching and CKKW matching seems to be the greatest, which is shown in Figure 6.7. Another important systematic uncertainty is the choice of matching scale as shown in Figure 6.4 and Figure 6.6. These two areas deserve more theoretical and experimental studies.

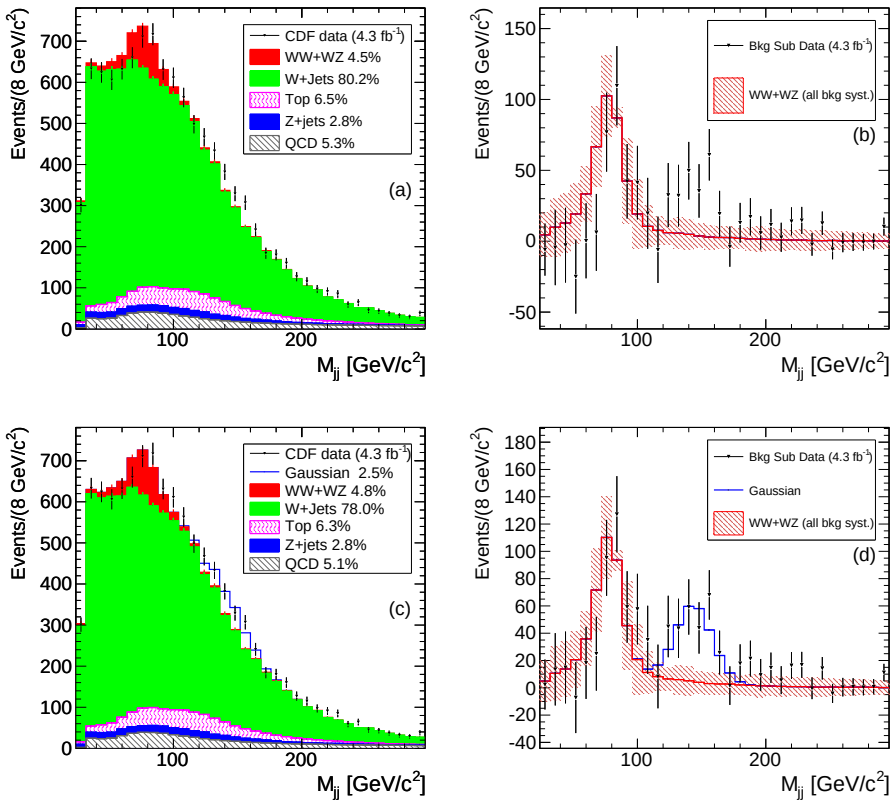

Figure 6.1: The dijet invariant mass distribution from CDF[134]. The sum of electron and muon events is plotted. In the left plots we show the fits for known processes only (a) and with the addition of a hypothetical Gaussian component (c). On the right plots we show, by subtraction, only the resonant contribution to M_{jj} including WW and WZ production (b) and the hypothesized narrow Gaussian contribution (d). In plot (b) and (d) data points differ because the normalization of the background changes between the two fits. The band in the subtracted plots represents the sum of all background shape systematic uncertainties described in the text. The distributions are shown with a 8 GeV/c^2 binning while the actual fit is performed using a 4 GeV/c^2 bin size.

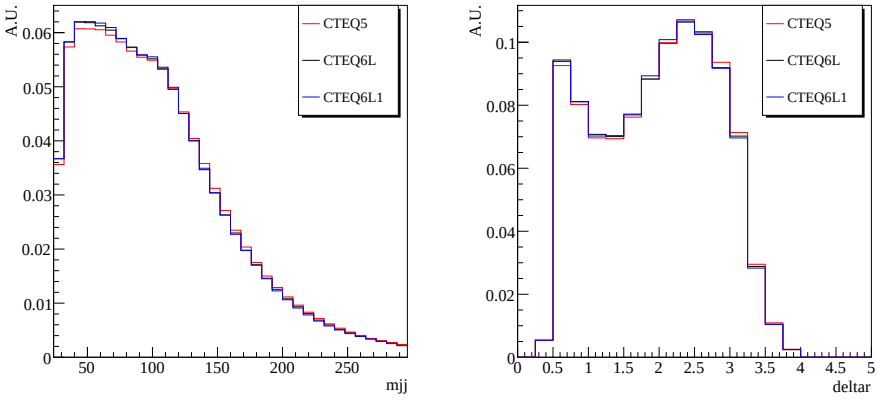

Figure 6.2: The comparison of the dijet mass spectrum(on the left) and the ΔR between the two jets for different PDF sets, CTEQ5, CTEQ6L and CTEQ6L1. The events are generated by ALPGEN, matched up to 3 jets. At parton level, the p_T cut is 15 GeV and the cone size is 0.4, during ME-PS merging, the matching scale is set to 20 GeV.

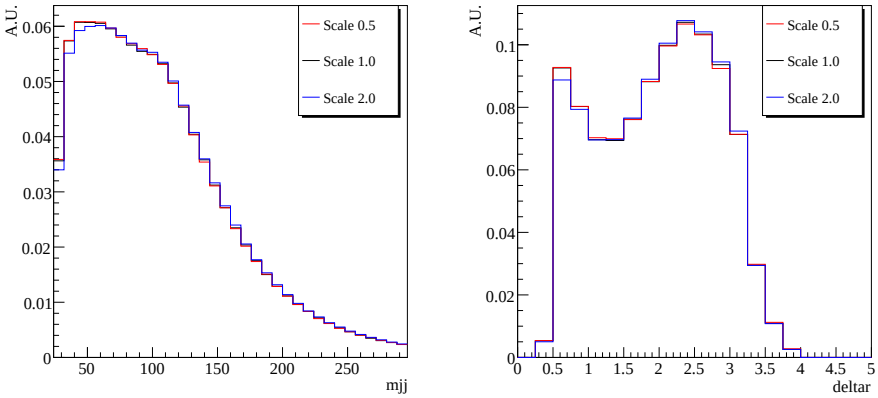

Figure 6.3: The comparison of the dijet mass spectrum(on the left) and the ΔR between the two jets for different renormalization and factorization choices. The events are generated by ALPGEN, matched up to 3 jets. At parton level, the p_T cut is 15 GeV and the cone size is 0.4, during ME-PS merging, the matching scale is set to 20 GeV. We will vary the default scale choice by a factor of half and two.

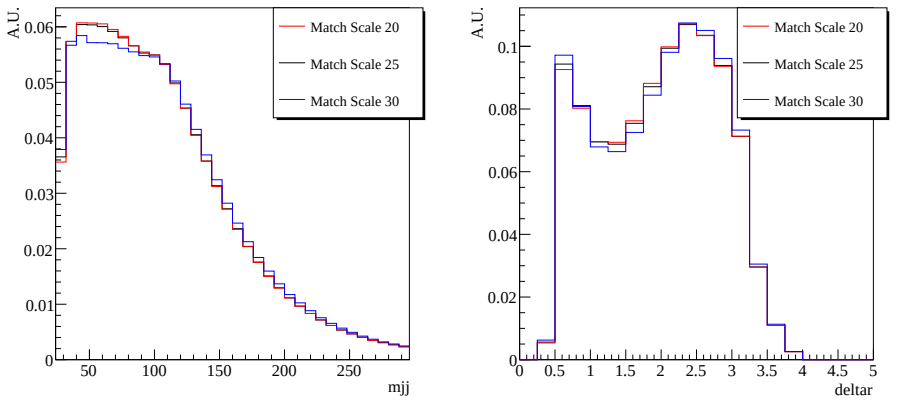

Figure 6.4: The comparison of the dijet mass spectrum(on the left) and the ΔR between the two jets for different matching scales. The events are generated by ALPGEN, matched up to 3 jets. At parton level, the p_T cut is 15 GeV and the cone size is 0.4, during ME-PS merging, the matching scale is set to 20, 25 and 30 GeV.

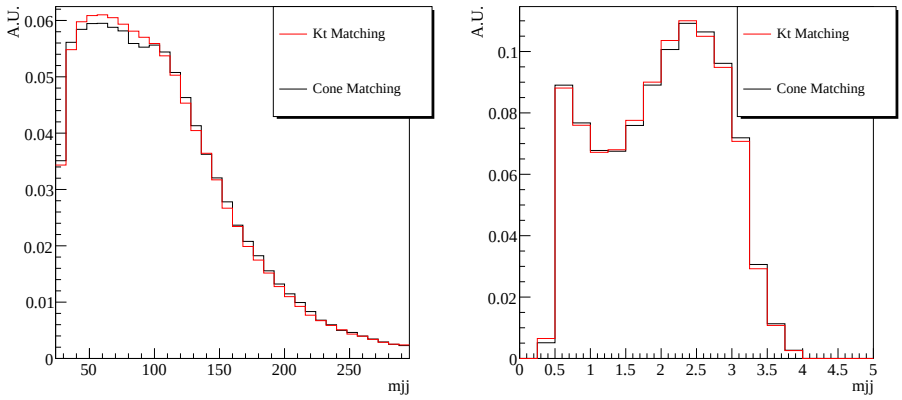

Figure 6.5: The comparison of the dijet mass spectrum(on the left) and the ΔR between the two jets for different MLM matching schemes. The events are generated by Madgraph, matched up to 3 jets. For MLM cone matching, at parton level the p_T cut is 15 GeV and the cone size is 0.4, during ME-PS merging, the matching scale is set to 20 GeV. For MLM k_T matching, at parton level, the k_T cut is 15 GeV and during ME-PS merging, the matching scale is set to 20 GeV.

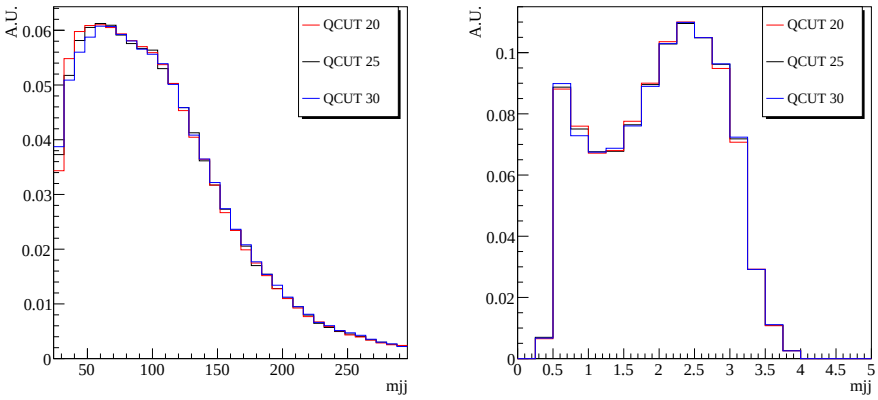

Figure 6.6: The comparison of the dijet mass spectrum(on the left) and the ΔR between the two jets for different MLM k_T matching scales. The events are generated by Madgraph, matched up to 3 jets with MLM k_T matching. At parton level the k_T cut is 15 GeV, during ME-PS merging, the matching scale is set to 20, 25 and 30 GeV.

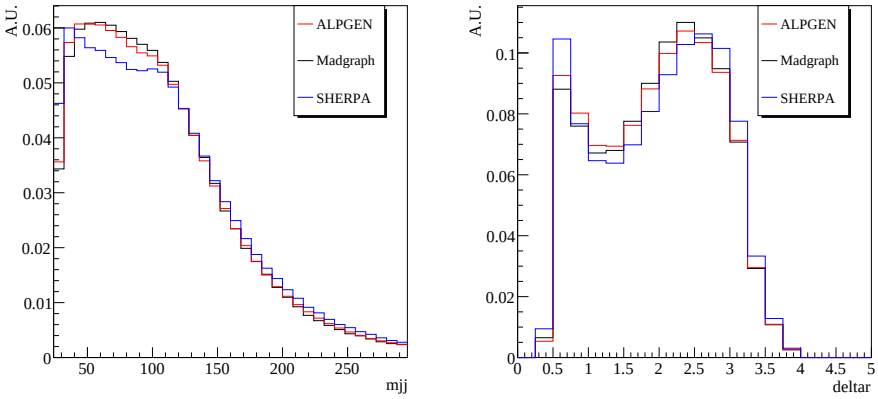

Figure 6.7: The comparison of the dijet mass spectrum(on the left) and the ΔR between the two jets for different event generators, ALPGEN, Madgraph and SHERPA. The samples for all the three generators are matched up to 3 jets. For ALPGEN and Madgraph, at parton level the p_T cut is 15 GeV and the cone size is 0.4, during ME-PS merging, the matching scale is set to 20 GeV. For SHERPA, the matching scale is set to 15 GeV for the CKKW matching.

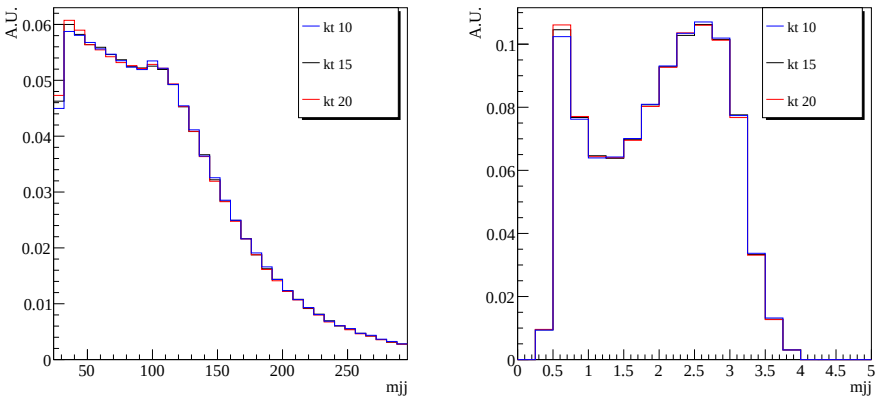

Figure 6.8: The comparison of the dijet mass spectrum(on the left) and the ΔR between the two jets for different CKKW matching scales. The events are generated by SHERPA, matched up to 3 jets with CKKW matching. And the matching scale is set to 10, 15 and 20 GeV.

Chapter 7

Conclusion

With the LHC turning on, it is a very exciting period for collider physics, which this thesis primarily focus on. And all the topics discussed in this thesis will be summarized below.

The thesis began, in chapter 2, with the estimation of the PDF uncertainties of the W boson production cross section. At the end of the day, every analysis at the LHC, for search of new physics or test of SM, has to be compared with the Monte Carlo Prediction. So we need to find out the proper normalization factor to connect between Events and Cross Section. The W boson production cross section serves as a Standard Candle for this purpose. Since the Parton Distribution Functions are measured experimentally, they come with statistical and systematic errors, and these errors will propagate into the W boson cross section computation in the MC generator. This chapter present the results both the uncertainties and its sensitivities to the acceptance cut by employing the Hessian Method.

In Chapter 3, we focus on the search strategy of a light SM Higgs boson. Inspired by [31], we search for a SM Higgs boson with mass around 120 GeV produced with a vector boson, and both of them are very boosted. In this search channel, the Higgs boson will decay to a pair of bottom quark and the vector boson will decay

leptonically. To kill the huge QCD background, we will require two b-tagged subjets inside the Higgs Jet and also apply the Jet Trimming Technique on the Higgs Jet to improve its mass resolution. It is shown that we could achieve the same statistical significance with 30 fb^{-1} data and could offer an alternative search strategy.

In Chapter 5, we continue to focus on collider search of a Non-SM Higgs boson. Instead decaying to SM particles, the Higgs boson will decay to a pair of (psuedo-)scalars, and decaying to four bottom quarks eventually. However, due to the weak coupling between the (psuedo-)scalar and the bottom quark, the (psuedo-)scalar will be long-lived, therefore, we are expected to see highly-displaced vertices in the (psuedo-)scalar decay. Taken advantage of this feature, we propose a set of efficient cuts to kill the QCD background and show that we are likely to observe this channel in the early LHC data.

Chapter 4, we introduce a new measurement sensitive to the Higgs/weak gauge-boson coupling, where the Higgs boson looks like a light SM Higgs boson, but its coupling to the gauge boson is different. The primary virtue of the proposed measurement is its insensitivity to experimental and theoretical uncertainties. Through such a measurement, one might detect subtle shifts in the Higgs couplings signaling the effects of new physics, and perhaps giving clues to the mechanism behind electroweak symmetry breaking.

Finally, in Chapter 6, we discuss various systematic uncertainty in the dijet mass distribution from the W+2jets production at the Tevatron. We use different PDF sets, scale choices, Monte Carlo Generators, ME-PS matching schemes and ME-PS matching scales. Among these factors, the largest difference comes from the CKKW matching implemented in SHERPA and the MLM cone matching implemented in ALPGEN (what the CDF has been using). Another important systematic error is the choice of the matching scale in ME-PS merging. These systematic uncertainties are important and needs more study both from the theoretical and experimental

effort.

Appendix A

Scattering Amplitudes for Longitudinal Gauge Bosons and Partial Wave Unitarity

For completeness, we will here review the high energy behavior of longitudinal gauge boson scattering. This will demonstrate why we expect the increase in the scattering amplitudes for non-SM Higgs couplings. It will also help us establish the partial wave unitarity bound for longitudinal gauge boson scattering, which is of practical importance for our simulation. We will make use of the Goldstone equivalence theorem, which says that the scattering behavior of the longitudinal gauge bosons is the same as that of the eaten Goldstones, up to corrections of order $\mathcal{O}(m_W/E)$. Note that while we will only explicitly calculate the behavior of $W_L^+W_L^- \to W_L^+W_L^-$, the other longitudinal gauge boson scattering processes are similar.

We begin with the Lagrangian for the SM Higgs doublet with the additional

dimension-6 operator we wish to study:

$$\mathcal{L} = \frac{1}{4}\,\mathrm{Tr}\left(\partial\mathcal{H}^\dagger\partial\mathcal{H} + \mu^2\mathcal{H}^\dagger\mathcal{H}\right) - \frac{\lambda}{16}\,\mathrm{Tr}\left(\mathcal{H}^\dagger\mathcal{H}\right)^2 + \frac{c_H}{32f^2}\left[\partial\,\mathrm{Tr}\left(\mathcal{H}^\dagger\mathcal{H}\right)\partial\,\mathrm{Tr}\left(\mathcal{H}^\dagger\mathcal{H}\right)\right] \tag{A.1}$$

where $\mathcal{H} = \phi\cdot\sigma$ for real fields ϕ_i $(i = 0 \leftrightarrow 3)$ and $\sigma = (1, \vec{\sigma})$. The SM Higgs potential corresponds to $c_H = 0$. Expanding around the minima $\langle\phi_0\rangle = \mu/\sqrt{\lambda}$ one finds new derivative interactions proportional to c_H. Those relevant to $\phi_+\phi_- \to \phi_+\phi_-$ scattering at lowest order are:

$$\mathcal{L} \supset -v\lambda h\phi_+\phi_- - \frac{\lambda}{2}\phi_+^2\phi_-^2 + \frac{c_H}{2f^2}\left(\phi_+^2(\partial\phi_-)^2 + \phi_+\phi_-\partial\phi_+\partial\phi_- + 2v\phi_+\partial\phi_-\partial h\right) + \text{h.c.} \tag{A.2}$$

where we have denoted the shifted ϕ_0 field by h and written $\phi_{1,2}$ in terms of their charge eigenstates $\phi_\pm$. Also, note that there is an additional kinetic term for h:

$$\mathcal{L} \supset \frac{c_H v^2}{2f^2}(\partial h)^2 \tag{A.3}$$

so that in going to canonical normalization we must insert a factor of $N = 1/\sqrt{1 + c_H v^2/f^2}$ for every h encountered at a vertex. The tree level amplitude becomes

$$\mathcal{M}(\phi_+\phi_- \to \phi_+\phi_-) = -4i\lambda + i\frac{c_H}{f^2}s - \frac{iN^2}{(s - m_h^2)}\left(2\lambda v + \frac{c_H v}{2f^2}s\right)^2 + (s \leftrightarrow t) \tag{A.4}$$

where $m_h = \sqrt{2\lambda}v$. Working in the limit $s, t \gg m_h^2$ we find

$$\mathcal{M}(\phi_+\phi_- \to \phi_+\phi_-) \approx i\frac{c_H}{f^2}\left(1 - N^2\frac{c_H v^2}{4f^2}\right)(s + t) \tag{A.5}$$

which shows the E^2 growth in the amplitude that we expect. In this limit, the $J = 0$

partial wave is:

$$a_0 = \frac{1}{16\pi s}\int_{-s}^{0}\frac{c_H}{f^2}\left(1 - N^2\frac{c_H v^2}{4f^2}\right)(s+t)\,dt = \frac{c_H s}{32\pi f^2}\left(1 - N^2\frac{c_H v^2}{4f^2}\right) \tag{A.6}$$

Partial wave unitarity is violated when $|\mathrm{Re}(a_I)| \geq 1/2$, so the unitarity bound is saturated when

$$s_{\max} = \frac{16\pi v^2}{c_H\xi\left(1 - c_H\xi N^2/4\right)} \tag{A.7}$$

To stay clear of this limit, we limit ourselves to studying events for which $s \leq 2$ TeV (corresponding to $|c_H\xi| \leq 0.6$).

We note that one may gain further intuition into the longitudinal gauge boson system by considering the parameterization

$$\mathcal{H} = (v + h)\,e^{i\vec{\pi}\cdot\vec{\sigma}/v} \tag{A.8}$$

Here we have shifted our field definitions so that the π transform non-linearly. In this language, the relevant terms in the Lagrangian become

$$\mathcal{L} \supset \frac{\sqrt{\lambda}}{\mu}h\partial\pi_+\partial\pi_- + \frac{\lambda}{6\mu^2}\left(\pi_+^2(\partial\pi_-)^2 - \pi_+\pi_-\partial\pi_+\partial\pi_-\right) + \text{h.c.} \tag{A.9}$$

As before, the kinetic term of h is shifted, so we must add a factor of N at every point we encounter an h at a vertex. Note, however, that in this case all of the operators come with $\partial\pi$ terms. Computed in this way, the amplitude $\mathcal{M}(\pi_+\pi_- \to \pi_+\pi_-)$ shows the same behavior as Eq. (A.4), as it must, but this is the result of a *non-cancelation* of derivatives between the four-point operator and the h-exchange in the t & s-channels, rather than because of a new vertex.

Using these results we can compare the scattering in the Higgsless case to that of the case where the Higgs has anomalous couplings. To consider the Higgsless case we

set $c_H = 0$ in Eq. (A.4) and consider the $\sqrt{s} \ll m_h$ limit using $m_h = \sqrt{2\lambda}v$. We find

$$\sigma_{\mathrm{no-higgs}} \propto |\mathcal{M}|^2 = \frac{4}{v^4}(s+t)^2 \tag{A.10}$$

wheras for the case of a light Higgs with anomalous couplings we find from Eq. (A.5)

$$\sigma_{\mathrm{anom-higgs}} \propto |\mathcal{M}|^2 = \frac{(c_H\xi)^2}{v^4}(s+t)^2 \tag{A.11}$$

under the assumption

$$\frac{c_H\xi}{2} \gg \frac{m_h^2}{s} \tag{A.12}$$

This is how we arrived at Eq. (4.3). For $m_h \sim 100$ GeV this is true for scattering at the TeV scale as long as $c_H\xi \gtrsim 1/10$. At lower values of the anomalous coupling the dominant effect comes from interference effects proportional to $s+t$ instead of $(s+t)^2$. Thus smaller values of the anomalous couplings have a qualitatively different energy behavior that of larger values, making them especially difficult to resolve.

Appendix B

Overview of Jet Algorithms

While a comprehensive review of jet algorithms is beyond the scope of this work (see [107] for a recent review), here we will provide a short overview so the reader can quickly gain intuition into subjet techniques.

Jet algorithms can roughly be divided into two categories: cone algorithms, which function as cookie-cutters to stamp out jets from calorimeter cells, and sequential recombination algorithms, which build up a jet by merging four-momenta one by one in a prescribed order. Here we will focus on recombination algorithms.

Each of these algorithms functions by defining a distance measure between every pair of four-momenta and for each four-momenta individually:

$$d_{ij} = \min(p_{Ti}^{2n}, p_{Tj}^{2n}) \left(\frac{R_{ij}}{R_0} \right)^2, \; d_{iB} = p_{Tj}^{2n} \tag{B.1}$$

for jets i and j. If the smallest distance measure at a given stage in clustering is between two four-momenta they are merged, otherwise the four-momenta with the smallest d_{iB} is declared a jet and removed from the queue.

The different sequential recombination algorithms are distinguished by value of n appearing in Eq. (B.1). These values determine the clustering order, whether one clusters beginning with hard four-momenta, soft four-momenta, or by angle (see

Algortithm	n	Approximate clustering order
k_T	1	soft$\rightarrow$ hard
C/A	0	near$\rightarrow$far (in y-ϕ)
anti-k_T	-1	hard$\rightarrow$ soft

Table B.1: Parameterization and approximate behavior of sequential recombination jet algorithms.

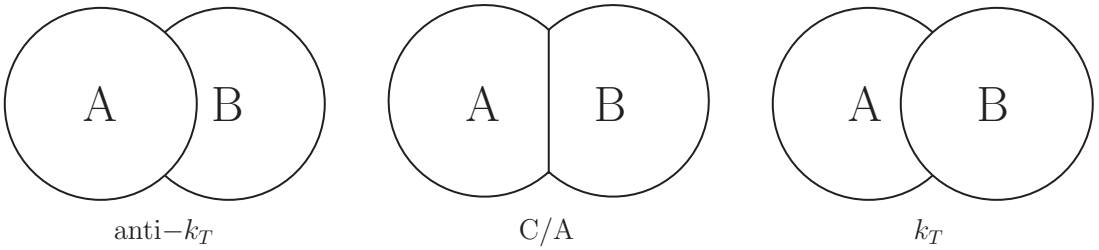

Figure B.1: Approximate clustering behavior of jets for the different sequential recombination algorithms assuming $p_T^A > p_T^B$. Note that while we have shown the jets as being circular, the k_T jets can behave in a non-circular, wandering way.

Table B.1 and Fig. B.1). For the subjet analysis at hand, where reconstructing the softer subjet is essential, we therefore use the k_T algorithm which begins by clustering softer jets, preventing them from being cannibalized by the harder subjet.

Bibliography

[1] N. E. Adam, V. Halyo, S. A. Yost and W. Zhu, JHEP **0809**, 133 (2008) [arXiv:0808.0758 [hep-ph]].

[2] W. Zhu, arXiv:1107.1808 [hep-ph].

[3] T. Han, D. Krohn, L.-T. Wang, and W. Zhu, *New Physics Signals in Longitudinal Gauge Boson Scattering at the LHC*, *JHEP* **03** (2010) 082, [0911.3656].

[4] S. L. Glashow, *Partial Symmetries of Weak Interactions*, *Nucl. Phys.* **22** (1961) 579–588.

[5] S. Weinberg, *A Model of Leptons*, *Phys. Rev. Lett.* **19** (1967) 1264–1266.

[6] A. Salam and J. C. Ward, *Electromagnetic and weak interactions*, *Phys. Lett.* **13** (1964) 168–171.

[7] F. Englert and R. Brout, *Broken Symmetry and the Mass of Gauge Vector Mesons*, *Phys. Rev. Lett.* **13** (1964) 321–322.

[8] P. W. Higgs, *Broken symmetries, massless particles and gauge fields*, *Phys. Lett.* **12** (1964) 132–133.

[9] G. S. Guralnik, C. R. Hagen, and T. W. B. Kibble, *Global Conservation Laws and Massless Particles*, *Phys. Rev. Lett.* **13** (1964) 585–587.

[10] **Particle Data Group** Collaboration, S. Eidelman *et al.*, *Review of particle physics*, *Phys. Lett.* **B592** (2004) 1.

[11] S. Dimopoulos and H. Georgi, *Softly Broken Supersymmetry and SU(5)*, *Nucl. Phys.* **B193** (1981) 150.

[12] S. Weinberg, *Approximate symmetries and pseudoGoldstone bosons*, *Phys. Rev. Lett.* **29** (1972) 1698–1701.

[13] H. Georgi and A. Pais, *Vacuum Symmetry and the PseudoGoldstone Phenomenon*, *Phys. Rev.* **D12** (1975) 508.

[14] H. Georgi and A. Pais, *Calculability and Naturalness in Gauge Theories*, *Phys. Rev.* **D10** (1974) 539.

[15] S. Weinberg, *Implications of Dynamical Symmetry Breaking*, *Phys. Rev.* **D13** (1976) 974–996.

[16] L. Susskind, *Dynamics of Spontaneous Symmetry Breaking in the Weinberg-Salam Theory*, *Phys. Rev.* **D20** (1979) 2619–2625.

[17] W. Buchmuller and D. Wyler, *Effective Lagrangian Analysis of New Interactions and Flavor Conservation*, *Nucl. Phys.* **B268** (1986) 621.

[18] R. Barbieri and A. Strumia, *What is the limit on the Higgs mass?*, *Phys. Lett.* **B462** (1999) 144–149, [`hep-ph/9905281`].

[19] M. Dittmar, F. Pauss and D. Zurcher, *Phys. Rev.* **D56** (1997) 7284 [hep-ex/9705004];
V.A. Koze, A.D. Martin, R. Orava and M.G. Ryskin, *Eur. Phys. J.* **C19** (2001) [arXiv:hep-ph/0010163]; W.T. Giele and S.A. Keller, arXiv:hep-ph/0104053;

[20] M.W. Krasny, F. Fayette, W. Płaczek, *Eur. Phys. J.* **C51** (2007) 607.

[21] S.D. Drell and T.M. Yan, *Phys. Rev. Lett.* **25** (1970) 316.

[22] J. Pumplin *et al.*, Phys. Rev. D **65**, 014013 (2001) [arXiv:hep-ph/0101032].

[23] A.D. Martin, R.G. Roberts, W.J. Stirling, and R.S. Thorne, *Phys. Lett.* **B652** (2007) 292, *ibid.* **B636** (2006) 259; *Eur. Phys. J.* **C28** (2003) 455, *ibid.* **C23** (2002) 73, *ibid.* **C18** (2000) 117; `durpdg.dur.ac.uk/hepdata/mrs.html`.

[24] A. Cafarella, C. Coriano, and M. Guzzi, *JHEP* **0708** (2007) 030; *Nucl. Phys.* **B748** (2006) 253.

[25] W.K. Tung, H.L. Lai, A. Belyaev, J. Pumplin, D. Stump, C.-P. Yuan, *JHEP* **0702** (2007) 053; D. Stump, J. Huston, J. Pumplin, W.-K. Tung, H.L. Lai, S. Kuhlmann, and J.F. Owens, *JHEP* **0310** (2003) 046; J. Pumplin, D. Stump, J. Huston, H.L. Lai, P. Nadolsky and W.-K. Tung, *JHEP* **07** (2002) 012; `hep.pa.msu.edu/people/wkt/cteq6/cteq6pdf.html`.

[26] M. W. Grunewald, J. Phys. Conf. Ser. **110**, 042008 (2008). [arXiv:0709.3744 [hep-ph]].

[27] T. Aaltonen *et al.* [CDF and D0 Collaborations], Phys. Rev. Lett. **104**, 061802 (2010) [arXiv:1001.4162 [hep-ex]].

[28] G. Aad *et al.* [The ATLAS Collaboration], [arXiv:0901.0512 [hep-ex]].

[29] G. L. Bayatian *et al.* [CMS Collaboration], J. Phys. G **G34**, 995-1579 (2007).

[30] D. Krohn, J. Thaler and L. T. Wang, JHEP **1002**, 084 (2010) [arXiv:0912.1342 [hep-ph]].

[31] J. M. Butterworth, A. R. Davison, M. Rubin and G. P. Salam, Phys. Rev. Lett. **100**, 242001 (2008) [arXiv:0802.2470 [hep-ph]].

[32] T. Sjostrand, S. Mrenna and P. Z. Skands, JHEP **0605**, 026 (2006) [arXiv:hep-ph/0603175].

[33] G. Corcella, I. G. Knowles, G. Marchesini, S. Moretti, K. Odagiri, P. Richardson, M. H. Seymour, B. R. Webber, [arXiv:hep-ph/0210213].

[34] M. Cacciari and G. P. Salam, Phys. Lett. B **641**, 57 (2006) [arXiv:hep-ph/0512210].

[35] *Precision electroweak measurements on the Z resonance*, *Phys. Rept.* **427** (2006) 257, [hep-ex/0509008]. The **ALEPH** Collaboration, the **DELPHI** Collaboration, the **L3** Collaboration, the **OPAL** Collaboration, the **SLD** Collaboration, the **LEP** Electroweak Working Group, the **SLD** electroweak, heavy flavour groups.

[36] N. Arkani-Hamed, A. G. Cohen and H. Georgi, Phys. Lett. B **513**, 232 (2001) [arXiv:hep-ph/0105239].

[37] R. Barbieri, A. Pomarol, R. Rattazzi, and A. Strumia, *Electroweak symmetry breaking after LEP-1 and LEP-2*, *Nucl. Phys.* **B703** (2004) 127–146, [hep-ph/0405040].

[38] R. Contino, Y. Nomura, and A. Pomarol, *Higgs as a holographic pseudo-Goldstone boson*, *Nucl. Phys.* **B671** (2003) 148–174, [hep-ph/0306259].

[39] C. N. Leung, S. T. Love, and S. Rao, *Low-Energy Manifestations of a New Interaction Scale: Operator Analysis*, *Z. Phys.* **C31** (1986) 433.

[40] J. Wudka, *Electroweak effective Lagrangians*, *Int. J. Mod. Phys.* **A9** (1994) 2301–2362, [hep-ph/9406205].

[41] K. Hagiwara, S. Ishihara, R. Szalapski, and D. Zeppenfeld, *Low-energy constraints on electroweak three gauge boson couplings*, *Phys. Lett.* **B283** (1992) 353–359.

[42] K. Hagiwara, S. Ishihara, R. Szalapski, and D. Zeppenfeld, *Low-energy effects of new interactions in the electroweak boson sector*, *Phys. Rev.* **D48** (1993) 2182–2203.

[43] **Particle Data Group** Collaboration, K. Hagiwara *et al.*, *Review of particle physics*, *Phys. Rev.* **D66** (2002) 010001.

[44] V. Barger, T. Han, P. Langacker, B. McElrath, and P. Zerwas, *Effects of genuine dimension-six Higgs operators*, *Phys. Rev.* **D67** (2003) 115001, [hep-ph/0301097].

[45] G. F. Giudice, C. Grojean, A. Pomarol, and R. Rattazzi, *The Strongly-Interacting Light Higgs*, *JHEP* **06** (2007) 045, [hep-ph/0703164].

[46] D. A. Dicus and V. S. Mathur, *Upper bounds on the values of masses in unified gauge theories*, *Phys. Rev.* **D7** (1973) 3111–3114.

[47] B. W. Lee, C. Quigg, and H. B. Thacker, *Weak Interactions at Very High-Energies: The Role of the Higgs Boson Mass*, *Phys. Rev.* **D16** (1977) 1519.

[48] M. J. G. Veltman, *Second Threshold in Weak Interactions*, *Acta Phys. Polon.* **B8** (1977) 475.

[49] M. S. Chanowitz and M. K. Gaillard, *The TeV Physics of Strongly Interacting W's and Z's*, *Nucl. Phys.* **B261** (1985) 379.

[50] I. Low, R. Rattazzi, and A. Vichi, *Theoretical Constraints on the Higgs Effective Couplings*, 0907.5413.

[51] R. Barbieri, B. Bellazzini, V. S. Rychkov, and A. Varagnolo, *The Higgs boson from an extended symmetry*, *Phys. Rev.* **D76** (2007) 115008, [0706.0432].

[52] M. E. Peskin and T. Takeuchi, *A New constraint on a strongly interacting Higgs sector*, *Phys. Rev. Lett.* **65** (1990) 964–967.

[53] J. M. Butterworth, B. E. Cox, and J. R. Forshaw, *W W scattering at the LHC*, *Phys. Rev.* **D65** (2002) 096014, [hep-ph/0201098].

[54] J. Bagger, S. Dawson, and G. Valencia, *Effective field theory calculation of p p → V(L) V(L) X*, *Nucl. Phys.* **B399** (1993) 364–394, [hep-ph/9204211].

[55] J. Bagger *et al.*, Phys. Rev. D **52**, 3878 (1995) [arXiv:hep-ph/9504426].

[56] V. D. Barger, K.-m. Cheung, T. Han, and R. J. N. Phillips, *Strong W^+W^+ scattering signals at pp supercolliders*, *Phys. Rev.* **D42** (1990) 3052–3077.

[57] M. S. Chanowitz, *Strong W W scattering at the end of the 90's: Theory and experimental prospects*, hep-ph/9812215.

[58] D. A. Dicus, J. F. Gunion, and R. Vega, *Isolating the scattering of longitudinal W+'s at the SSC using like sign dileptons*, *Phys. Lett.* **B258** (1991) 475–481.

[59] V. D. Barger, K.-m. Cheung, T. Han, J. Ohnemus, and D. Zeppenfeld, *A Comparative study of the benefits of forward jet tagging in heavy Higgs production at the SSC*, *Phys. Rev.* **D44** (1991) 1426–1437.

[60] V. Hankele, G. Klamke, D. Zeppenfeld, and T. Figy, *Anomalous Higgs boson couplings in vector boson fusion at the CERN LHC*, *Phys. Rev.* **D74** (2006) 095001, [hep-ph/0609075].

[61] J. Bagger *et al.*, *The Strongly interacting W W system: Gold plated modes*, *Phys. Rev.* **D49** (1994) 1246–1264, [hep-ph/9306256].

[62] G. J. Gounaris, J. Layssac, and F. M. Renard, *Vector boson pair production at supercollider: Useful approximate helicity amplitudes*, *Z. Phys.* **C62** (1994) 139–150, [hep-ph/9309324].

[63] A. Ballestrero, G. Bevilacqua, D. B. Franzosi, and E. Maina, *How well can the LHC distinguish between the SM light Higgs scenario, a composite Higgs and the Higgsless case using VV scattering channels?*, 0909.3838.

[64] K. Cheung, C.-W. Chiang, and T.-C. Yuan, *Partially Strong WW Scattering*, *Phys. Rev.* **D78** (2008) 051701, [0803.2661].

[65] H.-J. He, Y.-P. Kuang, C. P. Yuan, and B. Zhang, *Anomalous gauge interactions of the Higgs boson: Precision constraints and weak boson scatterings. ((U))*, *Phys. Lett.* **B554** (2003) 64–72, [hep-ph/0211229].

[66] B. Zhang, Y.-P. Kuang, H.-J. He, and C. P. Yuan, *Testing anomalous gauge couplings of the Higgs boson via weak-boson scatterings at the LHC*, *Phys. Rev.* **D67** (2003) 114024, [hep-ph/0303048].

[67] R. N. Cahn, S. D. Ellis, R. Kleiss, and W. J. Stirling, *Transverse Momentum Signatures for Heavy Higgs Bosons*, *Phys. Rev.* **D35** (1987) 1626.

[68] V. D. Barger, T. Han, and R. J. N. Phillips, *Improving the Heavy Higgs Boson Two Charged Lepton-Two Neutrino Signal*, *Phys. Rev.* **D37** (1988) 2005–2008.

[69] R. Kleiss and W. J. Stirling, *Tagging the Higgs*, *Phys. Lett.* **B200** (1988) 193.

[70] V. D. Barger, R. J. N. Phillips, and D. Zeppenfeld, *Mini - jet veto: A Tool for the heavy Higgs search at the LHC*, *Phys. Lett.* **B346** (1995) 106–114, [hep-ph/9412276].

[71] R. N. Cahn and S. Dawson, *Production of Very Massive Higgs Bosons*, *Phys. Lett.* **B136** (1984) 196.

[72] G. L. Kane, W. W. Repko, and W. B. Rolnick, *The Effective W+-, Z0 Approximation for High-Energy Collisions*, *Phys. Lett.* **B148** (1984) 367–372.

[73] S. Dawson, *The Effective W Approximation*, *Nucl. Phys.* **B249** (1985) 42–60.

[74] A. D. Martin, R. G. Roberts, W. J. Stirling, and R. S. Thorne, *Physical gluons and high E(T) jets*, *Phys. Lett.* **B604** (2004) 61–68, [hep-ph/0410230].

[75] S. Catani, Y. L. Dokshitzer, M. H. Seymour, and B. R. Webber, *Longitudinally invariant K(t) clustering algorithms for hadron hadron collisions*, *Nucl. Phys.* **B406** (1993) 187–224.

[76] S. D. Ellis and D. E. Soper, *Successive combination jet algorithm for hadron collisions*, *Phys. Rev.* **D48** (1993) 3160–3166, [hep-ph/9305266].

[77] Y. L. Dokshitzer, G. D. Leder, S. Moretti, and B. R. Webber, *Better Jet Clustering Algorithms*, *JHEP* **08** (1997) 001, [hep-ph/9707323].

[78] M. Wobisch and T. Wengler, *Hadronization corrections to jet cross sections in deep- inelastic scattering*, hep-ph/9907280.

[79] J. Thaler and L.-T. Wang, *Strategies to Identify Boosted Tops*, *JHEP* **07** (2008) 092, [0806.0023].

[80] K. Agashe, A. Delgado, M. J. May, and R. Sundrum, *RS1, custodial isospin and precision tests*, *JHEP* **08** (2003) 050, [hep-ph/0308036].

[81] G. L. Kane, G. A. Ladinsky, and C. P. Yuan, *Using the top quark for testing standard model polarization and CP predictions*, *Phys. Rev.* **D45** (1992) 124–141.

[82] K. Agashe, A. Belyaev, T. Krupovnickas, G. Perez, and J. Virzi, *LHC signals from warped extra dimensions*, *Phys. Rev.* **D77** (2008) 015003, [hep-ph/0612015].

[83] B. Lillie, L. Randall, and L.-T. Wang, *The Bulk RS KK-gluon at the LHC*, *JHEP* **09** (2007) 074, [hep-ph/0701166].

[84] V. Barger, T. Han, and D. G. E. Walker, *Top Quark Pairs at High Invariant Mass: A Model- Independent Discriminator of New Physics at the LHC*, *Phys. Rev. Lett.* **100** (2008) 031801, [hep-ph/0612016].

[85] A. L. Fitzpatrick, J. Kaplan, L. Randall, and L.-T. Wang, *Searching for the Kaluza-Klein Graviton in Bulk RS Models*, *JHEP* **09** (2007) 013, [hep-ph/0701150].

[86] W. Skiba and D. Tucker-Smith, *Using jet mass to discover vector quarks at the LHC*, *Phys. Rev.* **D75** (2007) 115010, [hep-ph/0701247].

[87] U. Baur and L. H. Orr, *High p_T Top Quarks at the Large Hadron Collider*, *Phys. Rev.* **D76** (2007) 094012, [0707.2066].

[88] R. Frederix and F. Maltoni, *Top pair invariant mass distribution: a window on new physics*, *JHEP* **01** (2009) 047, [0712.2355].

[89] U. Baur and L. H. Orr, *Searching for $t\bar{t}$ Resonances at the Large Hadron Collider*, *Phys. Rev.* **D77** (2008) 114001, [0803.1160].

[90] D. E. Kaplan, K. Rehermann, M. D. Schwartz, and B. Tweedie, *Top Tagging: A Method for Identifying Boosted Hadronically Decaying Top Quarks*, *Phys. Rev. Lett.* **101** (2008) 142001, [0806.0848].

[91] L. G. Almeida *et al.*, *Substructure of high-p_T Jets at the LHC*, 0807.0234.

[92] L. G. Almeida, S. J. Lee, G. Perez, I. Sung, and J. Virzi, *Top Jets at the LHC*, *Phys. Rev.* **D79** (2009) 074012, [0810.0934].

[93] Y. Bai and Z. Han, *Top-antitop and Top-top Resonances in the Dilepton Channel at the CERN LHC*, *JHEP* **04** (2009) 056, [0809.4487].

[94] T. C. Collaboration, *A cambridge-aachen (c-a) based jet algorithm for boosted top-jet tagging*, Tech. Rep. CMS PAS JME-09-001, Jul, 2007.

[95] G. Brooijmans, *High p_t hadronic top quark identification*, Tech. Rep. ATL-COM-PHYS-2008-001, ATLAS, Feb, 2008.

[96] S. D. Ellis, C. K. Vermilion, and J. R. Walsh, *Techniques for improved heavy particle searches with jet substructure*, 0903.5081.

[97] J. Shelton, *Polarized tops from new physics: signals and observables*, *Phys. Rev.* **D79** (2009) 014032, [0811.0569].

[98] M. Perelstein and A. Weiler, *Polarized Tops from Stop Decays at the LHC*, *JHEP* **03** (2009) 141, [0811.1024].

[99] L. March, E. Ros, and B. Salvacha, *Search for kaluza-klein excitations of the gluon in models with extra dimensions*, Tech. Rep. ATL-PHYS-PUB-2006-002. ATL-COM-PHYS-2005-032, CERN, Geneva, Jul, 2005.

[100] S. Gonzlez de la Hoz, L. March, and E. Ros, *Search for hadronic decays of z_H and w_H in the little higgs model*, Tech. Rep. ATL-PHYS-PUB-2006-003. ATL-COM-PHYS-2005-001, CERN, Geneva, 2005.

[101] M. Lehmacher, *b-Tagging Algorithms and their Performance at ATLAS*, 0809.4896.

[102] M. Cacciari, G. Salam, and G. Soyez, "FastJet." http://fastjet.fr/.

[103] F. Maltoni and T. Stelzer, *MadEvent: Automatic event generation with MadGraph*, *JHEP* **02** (2003) 027, [hep-ph/0208156].

[104] M. Bahr *et al.*, *Herwig++ Physics and Manual*, *Eur. Phys. J.* **C58** (2008) 639–707, [0803.0883].

[105] M. Cacciari, G. P. Salam, and G. Soyez, *The anti-k_t jet clustering algorithm*, *JHEP* **04** (2008) 063, [0802.1189].

[106] S. D. Ellis, J. Huston, K. Hatakeyama, P. Loch, and M. Tonnesmann, *Jets in hadron-hadron collisions*, *Prog. Part. Nucl. Phys.* **60** (2008) 484–551, [0712.2447].

[107] G. P. Salam, *Towards Jetography*, 0906.1833.

[108] M. J. Strassler and K. M. Zurek, Phys. Lett. B **661**, 263 (2008) [arXiv:hep-ph/0605193].

[109] S. Chang, P. J. Fox, N. Weiner, JHEP **0608**, 068 (2006). [hep-ph/0511250]

[110] L. M. Carpenter, D. E. Kaplan, E. -J. Rhee, Phys. Rev. Lett. **99**, 211801 (2007). [hep-ph/0607204].

[111] V. M. Abazov *et al.* [D0 Collaboration], Phys. Rev. Lett. **103**, 071801 (2009). [arXiv:0906.1787 [hep-ex]].

[112] M. J. Strassler and K. M. Zurek, Phys. Lett. B **651**, 374 (2007) [arXiv:hep-ph/0604261].

[113] M. Cacciari, G. P. Salam, G. Soyez, JHEP **0804**, 063 (2008) [arXiv:0802.1189 [hep-ph]].

[114] M. Cacciari and G. P. Salam, Phys. Lett. B **659**, 119 (2008) [arXiv:0707.1378 [hep-ph]].

[115] K. T. Matchev and S. D. Thomas, Phys. Rev. D **62**, 077702 (2000) [arXiv:hep-ph/9908482].

[116] T. Sjostrand, S. Mrenna and P. Z. Skands, JHEP **0605**, 026 (2006) [arXiv:hep-ph/0603175].

[117] M. L. Mangano, M. Moretti, F. Piccinini, R. Pittau and A. D. Polosa, JHEP **0307**, 001 (2003) [arXiv:hep-ph/0206293].

[118] S. Dittmaier *et al.* [LHC Higgs Cross Section Working Group], arXiv:1101.0593 [hep-ph].

[119] N. Greiner, A. Guffanti, T. Reiter and J. Reuter, arXiv:1105.3624 [hep-ph].

[120] M. G. Albrow *et al.* [TeV4LHC QCD Working Group], arXiv:hep-ph/0610012.

[121] R. V. Harlander and W. B. Kilgore, Phys. Rev. Lett. **88** (2002) 201801 [arXiv:hep-ph/0201206].

[122] C. Anastasiou and K. Melnikov, Nucl. Phys. B **646** (2002) 220 [arXiv:hep-ph/0207004].

[123] V. Ravindran, J. Smith and W. L. van Neerven, Nucl. Phys. B **665** (2003) 325 [arXiv:hep-ph/0302135].

[124] N. Greiner, A. Guffanti, T. Reiter and J. Reuter, arXiv:1105.3624 [hep-ph].

[125] H. L. Lai *et al.* [CTEQ Collaboration], Eur. Phys. J. **C12**, 375-392 (2000). [hep-ph/9903282].

[126] S. Hoeche, F. Krauss, N. Lavesson, L. Lonnblad, M. Mangano, A. Schalicke and S. Schumann, arXiv:hep-ph/0602031.

[127] The CMS Collaboration, CMS PAS TRK-10-005

[128] C. -R. Chen, M. M. Nojiri, W. Sreethawong, JHEP **1011**, 012 (2010) [arXiv:1006.1151 [hep-ph]].

[129] A. Falkowski, D. Krohn, L. -T. Wang, J. Shelton, A. Thalapillil, arXiv:1006.1650 [hep-ph].

[130] M. Cacciari, G. P. Salam and G. Soyez, "The Catchment Area of Jets," JHEP **0804**, 005 (2008) [arXiv:0802.1188 [hep-ph]].

[131] S. Catani, Y. L. Dokshitzer, M. H. Seymour and B. R. Webber, "Longitudinally invariant K(t) clustering algorithms for hadron hadron collisions," Nucl. Phys. B **406**, 187 (1993).

[132] S. D. Ellis and D. E. Soper, "Successive Combination Jet Algorithm For Hadron Collisions," Phys. Rev. D **48**, 3160 (1993) [hep-ph/9305266].

[133] N. Arkani-Hamed and N. Weiner, JHEP **0812**, 104 (2008) [arXiv:0810.0714 [hep-ph]].

[134] T. Aaltonen *et al.* [CDF Collaboration], Phys. Rev. Lett. **106**, 171801 (2011) [arXiv:1104.0699 [hep-ex]].

[135] J. L. Hewett and T. G. Rizzo, arXiv:1106.0294 [hep-ph].

[136] Z. Liu, P. Nath and G. Peim, arXiv:1105.4371 [hep-ph].

[137] C. H. Chen, C. W. Chiang, T. Nomura and Y. Fusheng, arXiv:1105.2870 [hep-ph].

[138] T. Enkhbat, X. G. He, Y. Mimura and H. Yokoya, arXiv:1105.2699 [hep-ph].

[139] G. Segre and B. Kayser, arXiv:1105.1808 [hep-ph].

[140] L. M. Carpenter and S. Mantry, arXiv:1104.5528 [hep-ph].

[141] F. del Aguila, J. de Blas, P. Langacker and M. Perez-Victoria, arXiv:1104.5512 [hep-ph].

[142] J. E. Kim and S. Shin, arXiv:1104.5500 [hep-ph].

[143] Q. H. Cao, M. Carena, S. Gori, A. Menon, P. Schwaller, C. E. M. Wagner and L. T. M. Wang, arXiv:1104.4776 [hep-ph].

[144] B. Bhattacherjee and S. Raychaudhuri, arXiv:1104.4749 [hep-ph].

[145] S. Chang, K. Y. Lee and J. Song, arXiv:1104.4560 [hep-ph].

[146] B. A. Dobrescu and G. Z. Krnjaic, arXiv:1104.2893 [hep-ph].

[147] L. A. Anchordoqui, H. Goldberg, X. Huang, D. Lust and T. R. Taylor, arXiv:1104.2302 [hep-ph].

[148] A. E. Nelson, T. Okui and T. S. Roy, arXiv:1104.2030 [hep-ph].

[149] R. Sato, S. Shirai and K. Yonekura, Phys. Lett. B **700**, 122 (2011) [arXiv:1104.2014 [hep-ph]].

[150] X. G. He and B. Q. Ma, arXiv:1104.1894 [hep-ph].

[151] K. Cheung and J. Song, arXiv:1104.1375 [hep-ph].

[152] F. Yu, Phys. Rev. D **83**, 094028 (2011) [arXiv:1104.0243 [hep-ph]].

[153] M. R. Buckley, D. Hooper, J. Kopp and E. Neil, arXiv:1103.6035 [hep-ph].

[154] J. Alwall, S. Hoche, F. Krauss, N. Lavesson, L. Lonnblad, F. Maltoni, M. L. Mangano, M. Moretti *et al.*, Eur. Phys. J. **C53**, 473-500 (2008). [arXiv:0706.2569 [hep-ph]].

[155] F. Maltoni, T. Stelzer, JHEP **0302**, 027 (2003). [hep-ph/0208156].

[156] M. L. Mangano, M. Moretti, F. Piccinini, R. Pittau, A. D. Polosa, JHEP **0307**, 001 (2003). [hep-ph/0206293].

[157] T. Gleisberg, S. .Hoeche, F. Krauss, M. Schonherr, S. Schumann, F. Siegert, J. Winter, JHEP **0902**, 007 (2009). [arXiv:0811.4622 [hep-ph]].

[158] S. Schumann and F. Krauss, JHEP **0803**, 038 (2008) [arXiv:0709.1027 [hep-ph]].

[159] J. C. Winter, F. Krauss and G. Soff, Eur. Phys. J. C **36**, 381 (2004) [arXiv:hep-ph/0311085].